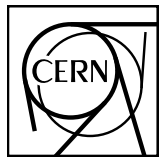


# EUROPEAN ORGANIZATION FOR NUCLEAR RESEARCH



ALICE-ANA-2016-xxx  
January 17, 2018

## Lambda-Kaon and Cascade-Kaon Femtoscopy in Pb-Pb Collisions at $\sqrt{s_{NN}} = 2.76 \text{ TeV}$ from the LHC ALICE Experiment

Jesse T. Buxton<sup>1</sup>

1. Department of Physics, The Ohio State University, Columbus, Ohio, USA

Email: jesse.thomas.buxton@cern.ch

### Abstract

We present results from a femtoscopic analysis of Lambda-Kaon correlations in Pb-Pb collisions at  $\sqrt{s_{NN}} = 2.76 \text{ TeV}$  by the ALICE experiment at the LHC. All pair combinations of  $\Lambda$  and  $\bar{\Lambda}$  with  $K^+$ ,  $K^-$  and  $K_S^0$  are analyzed. The femtoscopic correlations are the result of strong final-state interactions, and are fit with a parametrization based on a model by R. Lednicky and V. L. Lyuboshitz [1]. This allows us to both characterize the emission source and measure the scattering parameters for the particle pairs. We observe a large difference in the  $\Lambda$ - $K^+$  ( $\bar{\Lambda}$ - $K^-$ ) and  $\Lambda$ - $K^-$  ( $\bar{\Lambda}$ - $K^+$ ) correlations in pairs with low relative momenta ( $k^* \lesssim 100 \text{ MeV}$ ). Additionally, the average of the  $\Lambda$ - $K^+$  ( $\bar{\Lambda}$ - $K^-$ ) and  $\Lambda$ - $K^-$  ( $\bar{\Lambda}$ - $K^+$ ) correlation functions is consistent with our  $\Lambda$ - $K_S^0$  ( $\bar{\Lambda}$ - $K_S^0$ ) measurement. The results suggest an effect arising from different quark-antiquark interactions in the pairs, i.e.  $s\bar{s}$  in  $\Lambda$ - $K^+$  ( $\bar{\Lambda}$ - $K^-$ ) and  $u\bar{u}$  in  $\Lambda$ - $K^-$  ( $\bar{\Lambda}$ - $K^+$ ). To gain further insight into this hypothesis, we currently are conducting a  $\Xi$ -K femtoscopic analysis.



## Contents

<b>1</b>	<b>Introduction</b>	<b>6</b>
<b>2</b>	<b>Data Sample and Software</b>	<b>6</b>
2.1	Data Sample . . . . .	6
2.2	Software . . . . .	6
<b>3</b>	<b>Data Selection</b>	<b>6</b>
3.1	Event Selection and Mixing . . . . .	6
3.2	$K^\pm$ Track Selection . . . . .	7
3.3	V0 Selection . . . . .	8
3.3.1	$\Lambda$ Reconstruction . . . . .	9
3.3.2	$K_S^0$ Reconstruction . . . . .	11
3.4	Cascade Reconstruction . . . . .	12
3.5	Pair Selection . . . . .	15
<b>4</b>	<b>Correlation Functions</b>	<b>16</b>
<b>5</b>	<b>Fitting</b>	<b>17</b>
5.1	Model: $\Lambda K_S^0$ , $\Lambda K^\pm$ , $\Xi^{ch} K_S^0$ . . . . .	17
5.2	Model: $\Xi^{ch} K^{ch}$ . . . . .	20
5.3	Momentum Resolution Corrections . . . . .	23
5.4	Residual Correlations . . . . .	25
<b>6</b>	<b>Systematic Errors</b>	<b>30</b>
6.1	Systematic Errors: $\Lambda K_S^0$ . . . . .	30
6.1.1	Particle and Pair Cuts . . . . .	30
6.1.2	Non-Flat Background . . . . .	31
6.1.3	Fit Range . . . . .	32
6.2	Systematic Errors: $\Lambda K^\pm$ . . . . .	32
6.2.1	Particle and Pair Cuts . . . . .	32
6.2.2	Non-Flat Background . . . . .	33
6.2.3	Fit Range . . . . .	33
6.3	Systematic Errors: $\Xi K^\pm$ . . . . .	33
6.3.1	Particle and Pair Cuts . . . . .	33

<b>7 Results and Discussion</b>	<b>33</b>
7.1 Results: $\Lambda K_S^0$ and $\Lambda K^\pm$ . . . . .	33
7.1.1 Results: $\Lambda K_S^0$ and $\Lambda K^\pm$ : No Residual Correlations Included in Fit . . . . .	34
7.1.2 Results: $\Lambda K_S^0$ and $\Lambda K^\pm$ : 3 Residual Correlations Included in Fit . . . . .	48
7.1.3 Results: $\Lambda K_S^0$ and $\Lambda K^\pm$ : 10 Residual Correlations Included in Fit . . . . .	48
7.2 Results: $\Xi K^\pm$ . . . . .	48
<b>8 To Do</b>	<b>50</b>
<b>9 Additional Figures</b>	<b>68</b>
9.1 Residuals . . . . .	68
9.1.1 $\Lambda K^+$ Residuals . . . . .	68
9.1.2 $\Lambda K^-$ Residuals . . . . .	74
9.1.3 $\Lambda K_S^0$ Residuals . . . . .	80

## List of Figures

1	V0 Reconstruction	9
2	$K_S^0$ contamination in $\Lambda(\bar{\Lambda})$ collection	10
3	$\Lambda$ and $\bar{\Lambda}$ Purity	11
4	$\Lambda(\bar{\Lambda})$ contamination in $K_S^0$ collection	13
5	$K_S^0$ Purity	14
6	$\Xi$ Reconstruction	15
7	$\Xi^-(\bar{\Xi}^+)$ Purity	15
8	Average Separation of $\Lambda(\bar{\Lambda})$ and $K_S^0$ Daughters	17
9	Average Separation of $\Lambda(\bar{\Lambda})$ Daughter and $K^\pm$	18
10	Average Separation of $\Xi$ Daughters and $K^\pm$	19
11	$\Lambda(\bar{\Lambda})K_S^0$ Correlation Functions	20
12	$\Lambda K^+$ and $\bar{\Lambda} K^-$ Correlation Functions	21
13	$\Lambda K^-$ and $\bar{\Lambda} K^+$ Correlation Functions	22
14	Correlation Functions: $\Lambda K^+$ vs $\Lambda K^-$ for 0-10% Centrality	23
15	Momentum Resolution: Sample $k_{True}^*$ vs. $k_{Rec}^*$	26
16	Particle Contaminations Visible in $k_{True}^*$ vs. $k_{Rec}^*$	27
17	Transform Matrices for $\Lambda K^+$ Analysis	28
18	Transform Matrices for $\bar{\Lambda} K^+$ Analysis	29
19	$\Sigma^0 K^+$ Transform	31
20	$\Sigma^0 K^+$ Transform	32
21	Scattering Parameter Results	34
22	$\lambda$ vs. R (0-10% Centrality)	35
23	$\lambda$ vs. R (10-30% Centrality)	36
24	$\lambda$ vs. R (30-50% Centrality)	37
25	Scattering Parameter Results (free and fixed $d_0$ )	38
26	$\lambda$ vs. R (0-10% Centrality) (free and fixed $d_0$ )	38
27	$\lambda$ vs. R (10-30% Centrality) (free and fixed $d_0$ )	39
28	$\lambda$ vs. R (30-50% Centrality) (free and fixed $d_0$ )	39
29	$\Lambda K_S^0(\bar{\Lambda} K_S^0)$ Fits with No Residuals	40
30	$\Lambda K_S^0(\bar{\Lambda} K_S^0)$ Fits with No Residuals (Wide Range)	41
31	$\Lambda K^+(\bar{\Lambda} K^-)$ Fits, with NO residual correlations included, with No Residuals	42
32	$\Lambda K^+(\bar{\Lambda} K^-)$ Fits with No Residuals (Wide Range)	43

33	$\Lambda K^- (\bar{\Lambda} K^+)$ Fits with No Residuals . . . . .	44
34	$\Lambda K^- (\bar{\Lambda} K^+)$ Fits with No Residuals (Wide Range) . . . . .	45
35	$m_T$ Scaling of Radii: No Residuals in Fit . . . . .	48
36	$\Lambda K_S^0 (\bar{\Lambda} K_S^0)$ Fits with 3 Residuals . . . . .	49
37	$\Lambda K_S^0 (\bar{\Lambda} K_S^0)$ Fits with 3 Residuals (Wide Range) . . . . .	50
38	$\Lambda K^+ (\bar{\Lambda} K^-)$ Fits with 3 Residuals . . . . .	51
39	$\Lambda K^+ (\bar{\Lambda} K^-)$ Fits with 3 Residuals (Wide Range) . . . . .	52
40	$\Lambda K^- (\bar{\Lambda} K^+)$ Fits with 3 Residuals . . . . .	53
41	$\Lambda K^- (\bar{\Lambda} K^+)$ Fits with 3 Residuals (Wide Range) . . . . .	54
42	$m_T$ Scaling of Radii: 3 Residuals in Fit . . . . .	55
43	$\Lambda K_S^0 (\bar{\Lambda} K_S^0)$ Fits with 10 Residuals . . . . .	56
44	$\Lambda K_S^0 (\bar{\Lambda} K_S^0)$ Fits with 10 Residuals (Wide Range) . . . . .	57
45	$\Lambda K^+ (\bar{\Lambda} K^-)$ Fits with 10 Residuals . . . . .	58
46	$\Lambda K^+ (\bar{\Lambda} K^-)$ Fits with 10 Residuals (Wide Range) . . . . .	59
47	$\Lambda K^- (\bar{\Lambda} K^+)$ Fits with 10 Residuals . . . . .	60
48	$\Lambda K^- (\bar{\Lambda} K^+)$ Fits with 10 Residuals (Wide Range) . . . . .	61
49	$m_T$ Scaling of Radii: 10 Residuals in Fit . . . . .	62
50	$\Xi K^\pm$ Results . . . . .	62
51	$\Xi K^\pm$ Data with Coulomb-Only Bands, 0-10% Centrality . . . . .	63
52	Effect of Strong Force Inclusion on Coulomb-Only Curve for $\Xi K^\pm$ systems . . . . .	64
53	$\Xi K^\pm$ Global Coulomb-Only Fit (Set 1) . . . . .	65
54	$\Xi K^\pm$ Global Coulomb-Only Fit (Set 2) . . . . .	66
55	$\Xi^- K^+$ Coulomb-Only Fit . . . . .	66
56	$\Xi^- K^-$ Coulomb-Only Fit . . . . .	67
57	Residuals: $\Sigma^0 K^+$ to $\Lambda K^+$ (0-10% Centrality) . . . . .	68
58	Residuals: $\Xi^0 K^+$ to $\Lambda K^+$ (0-10% Centrality) . . . . .	69
59	Residuals: $\Xi^- K^+$ to $\Lambda K^+$ (0-10% Centrality) . . . . .	69
60	Residuals: $\Sigma^{*+} K^+$ to $\Lambda K^+$ (0-10% Centrality) . . . . .	70
61	Residuals: $\Sigma^{*-} K^+$ to $\Lambda K^+$ (0-10% Centrality) . . . . .	70
62	Residuals: $\Sigma^{*0} K^+$ to $\Lambda K^+$ (0-10% Centrality) . . . . .	71
63	Residuals: $\Lambda K^{*0}$ to $\Lambda K^+$ (0-10% Centrality) . . . . .	71
64	Residuals: $\Sigma^0 K^{*0}$ to $\Lambda K^+$ (0-10% Centrality) . . . . .	72
65	Residuals: $\Xi^0 K^{*0}$ to $\Lambda K^+$ (0-10% Centrality) . . . . .	72

66	Residuals: $\Xi^- K^{*0}$ to $\Lambda K^+$ (0-10% Centrality) . . . . .	73
67	Residuals: $\Sigma^0 K^-$ to $\Lambda K^-$ (0-10% Centrality) . . . . .	74
68	Residuals: $\Xi^0 K^-$ to $\Lambda K^-$ (0-10% Centrality) . . . . .	75
69	Residuals: $\Xi^- K^-$ to $\Lambda K^-$ (0-10% Centrality) . . . . .	75
70	Residuals: $\Sigma^{*+} K^-$ to $\Lambda K^-$ (0-10% Centrality) . . . . .	76
71	Residuals: $\Sigma^{*-} K^-$ to $\Lambda K^-$ (0-10% Centrality) . . . . .	76
72	Residuals: $\Sigma^{*0} K^-$ to $\Lambda K^-$ (0-10% Centrality) . . . . .	77
73	Residuals: $\Lambda \bar{K}^{*0}$ to $\Lambda K^-$ (0-10% Centrality) . . . . .	77
74	Residuals: $\Sigma^0 \bar{K}^{*0}$ to $\Lambda K^-$ (0-10% Centrality) . . . . .	78
75	Residuals: $\Xi^0 \bar{K}^{*0}$ to $\Lambda K^-$ (0-10% Centrality) . . . . .	78
76	Residuals: $\Xi^- \bar{K}^{*0}$ to $\Lambda K^-$ (0-10% Centrality) . . . . .	79
77	Residuals: $\Sigma^0 K_S^0$ to $\Lambda K_S^0$ (0-10% Centrality) . . . . .	80
78	Residuals: $\Xi^0 K_S^0$ to $\Lambda K_S^0$ (0-10% Centrality) . . . . .	81
79	Residuals: $\Xi^- K_S^0$ to $\Lambda K_S^0$ (0-10% Centrality) . . . . .	81
80	Residuals: $\Sigma^{*+} K_S^0$ to $\Lambda K_S^0$ (0-10% Centrality) . . . . .	82
81	Residuals: $\Sigma^{*-} K_S^0$ to $\Lambda K_S^0$ (0-10% Centrality) . . . . .	82
82	Residuals: $\Sigma^{*0} K_S^0$ to $\Lambda K_S^0$ (0-10% Centrality) . . . . .	83
83	Residuals: $\Lambda K^{*0}$ to $\Lambda K_S^0$ (0-10% Centrality) . . . . .	83
84	Residuals: $\Sigma^0 K^{*0}$ to $\Lambda K_S^0$ (0-10% Centrality) . . . . .	84
85	Residuals: $\Xi^0 K^{*0}$ to $\Lambda K_S^0$ (0-10% Centrality) . . . . .	84
86	Residuals: $\Xi^- K^{*0}$ to $\Lambda K_S^0$ (0-10% Centrality) . . . . .	85

---

## 12 1 Introduction

13 We present results from a femtoscopic analysis of Lambda-Kaon correlations in Pb-Pb collisions at  $\sqrt{s_{NN}}$   
 14 = 2.76 TeV by the ALICE experiment at the LHC. All pair combinations of  $\Lambda$  and  $\bar{\Lambda}$  with  $K^+$ ,  $K^-$  and  
 15  $K_S^0$  are analyzed. The femtoscopic correlations are the result of strong final-state interactions, and are  
 16 fit with a parametrization based on a model by R. Lednicky and V. L. Lyuboshitz [1]. This allows us to  
 17 both characterize the emission source and measure the scattering parameters for the particle pairs. We  
 18 observe a large difference in the  $\Lambda$ - $K^+$  ( $\bar{\Lambda}$ - $K^-$ ) and  $\Lambda$ - $K^-$  ( $\bar{\Lambda}$ - $K^+$ ) correlations in pairs with low relative  
 19 momenta ( $k^* \lesssim 100$  MeV). Additionally, the average of the  $\Lambda$ - $K^+$  ( $\bar{\Lambda}$ - $K^-$ ) and  $\Lambda$ - $K^-$  ( $\bar{\Lambda}$ - $K^+$ ) correlation  
 20 functions is consistent with our  $\Lambda$ - $K_S^0$  ( $\bar{\Lambda}$ - $K_S^0$ ) measurement. The results suggest an effect arising from  
 21 different quark-antiquark interactions in the pairs, i.e.  $s\bar{s}$  in  $\Lambda$ - $K^+$  ( $\bar{\Lambda}$ - $K^-$ ) and  $u\bar{u}$  in  $\Lambda$ - $K^-$  ( $\bar{\Lambda}$ - $K^+$ ). To  
 22 gain further insight into this hypothesis, we currently are conducting a  $\Xi$ -K femtoscopic analysis.

## 23 2 Data Sample and Software

### 24 2.1 Data Sample

25 The analysis used “pass 2” reconstructed Pb-Pb data from LHC11h (AOD145). The runlist was selected  
 26 from runs with global quality tag “1” in the ALICE Run Condition Table. Approximately 40 million  
 27 combined central, semi-central, and minimum bias events were analyzed. Runs from both positive (++)  
 28 and negative (--) magnetic field polarity settings were used.

29 Run list: 170593, 170572, 170388, 170387, 170315, 170313, 170312, 170311, 170309, 170308, 170306,  
 30 170270, 170269, 170268, 170230, 170228, 170207, 170204, 170203, 170193, 170163, 170159, 170155,  
 31 170091, 170089, 170088, 170085, 170084, 170083, 170081, 170040, 170027, 169965, 169923, 169859,  
 32 169858, 169855, 169846, 169838, 169837, 169835, 169591, 169590, 169588, 169587, 169586, 169557,  
 33 169555, 169554, 169553, 169550, 169515, 169512, 169506, 169504, 169498, 169475, 169420, 169419,  
 34 169418, 169417, 169415, 169411, 169238, 169167, 169160, 169156, 169148, 169145, 169144, 169138,  
 35 169099, 169094, 169091, 169045, 169044, 169040, 169035, 168992, 168988, 168826, 168777, 168514,  
 36 168512, 168511, 168467, 168464, 168460, 168458, 168362, 168361, 168342, 168341, 168325, 168322,  
 37 168311, 168310, 168315, 168108, 168107, 168105, 168076, 168069, 167988, 167987, 167985, 167920,  
 38 167915

39 Analysis was also performed on the LHC12a17a\_fix (AOD149) Monte Carlo HIJING events for certain  
 40 checks. THERMINATOR2 was also used for certain aspects, such as transform matrices described feed-  
 41 down contributions.

### 42 2.2 Software

43 The analysis was performed on the PWGCF analysis train using AliRoot v5-08-18-1 and AliPhysics  
 44 vAN-20161027-1.

45 The main classes utilized include: AliFemtoVertexMultAnalysis, AliFemtoEventCutEstimators, AliFem-  
 46 toESDTrackCutNSigmaFilter, AliFemtoV0TrackCutNSigmaFilter, AliFemtoXiTrackCut, AliFemtoV0PairCut,  
 47 AliFemtoV0TrackPairCut, AliFemtoXiTrackPairCut, and AliFemtoAnalysisLambdaKaon. All of these  
 48 classes are contained in /AliPhysics/PWGCF/FEMTOSCOPY/AliFemto and .../AliFemtoUser.

## 49 3 Data Selection

### 50 3.1 Event Selection and Mixing

51 The events used in this study were selected with the class AliFemtoEventCutEstimators according to the  
 52 following criteria:

- 53        – Triggers
- 54            – minimum bias (kMB)
- 55            – central (kCentral)
- 56            – semi-central (kSemiCentral)
- 57        – z-position of reconstructed event vertex must be within 10 cm of the center of the ALICE detector
- 58        – the event must contain at least one particle of each type from the pair of interest

59     The event mixing was handled by the AliFemtoVertexMultAnalysis class, which only mixes events with  
60     like vertex position and centrality. The following criteria were used for event mixing:

- 61        – Number of events to mix = 5
- 62        – Vertex position bin width = 2 cm
- 63        – Centrality bin width = 5

64     The AliFemtoEventReaderAODChain class is used to read the events. Event flattening is not currently  
65     used. FilterBit(7). The centrality is determined by the “V0M” method of AliCentrality, set by calling Al-  
66     iFemtoEventReaderAOD::SetUseMultiplicity(kCentrality). I utilize the SetPrimaryVertexCorrectionT-  
67     PCPoints switch, which causes the reader to shift all TPC points to be relative to the event vertex.

### 68     3.2 K $^{\pm}$ Track Selection

69     Charged kaons are identified using the AliFemtoESDTrackCutNSigmaFilter class. The specific cuts used  
70     in this analysis are as follows:

71     Track Selection:

- 72        – Kinematic range:
- 73            –  $0.14 < p_T < 1.5$
- 74            –  $|\eta| < 0.8$
- 75        – FilterBit(7)
- 76            – TPC tracks
- 77        – Track Quality
- 78            – Minimum number of clusters in the TPC (fminTPCncls) = 80
- 79            – Maximum allowed  $\chi^2/N_{DOF}$  for ITS clusters = 3.0
- 80            – Maximum allowed  $\chi^2/N_{DOF}$  for TPC clusters = 4.0
- 81        – Primary Particle Selection:
- 82            – Maximum XY impact parameter = 2.4
- 83            – Maximum Z impact parameter = 3.0
- 84        – Remove particles with any kink labels (fRemoveKinks = true)
- 85        – Maximum allowed sigma to primary vertex (fMaxSigmaToVertex) = 3.0

86 K $^\pm$  Identification:

87 – PID Probabilities:

- 88 – K: > 0.2
- 89 –  $\pi$ : < 0.1
- 90 –  $\mu$ : < 0.8
- 91 – p: < 0.1

92 – Most probable particle type must be Kaon (fMostProbable=3)

93 – TPC and TOF N $_\sigma$  cuts:

- 94 –  $p < 0.4 \text{ GeV}/c$ : N $_{\sigma K, TPC} < 2$
- 95 –  $0.4 < p < 0.45 \text{ GeV}/c$ : N $_{\sigma K, TPC} < 1$
- 96 –  $0.45 < p < 0.8 \text{ GeV}/c$ : N $_{\sigma K, TPC} < 3 \& N_{\sigma K, TOF} < 2$
- 97 –  $0.8 < p < 1.0 \text{ GeV}/c$ : N $_{\sigma K, TPC} < 3 \& N_{\sigma K, TOF} < 1.5$
- 98 –  $p > 1.0 \text{ GeV}/c$ : N $_{\sigma K, TPC} < 3 \& N_{\sigma K, TOF} < 1$

99 – Electron Rejection: Reject if N $_{\sigma e^-, TPC} < 3$

100 – Pion Rejection: Reject if:

- 101 –  $p < 0.65$ 
  - 102 \* if TOF and TPC available: N $_{\sigma \pi, TPC} < 3 \& N_{\sigma \pi, TOF} < 3$
  - 103 \* else
    - 104 ·  $p < 0.5$ : N $_{\sigma \pi, TPC} < 3$
    - 105 ·  $0.5 < p < 0.65$ : N $_{\sigma \pi, TPC} < 2$
- 106 –  $0.65 < p < 1.5$ : N $_{\sigma \pi, TPC} < 5 \& N_{\sigma \pi, TOF} < 3$
- 107 –  $p > 1.5$ : N $_{\sigma \pi, TPC} < 5 \& N_{\sigma \pi, TOF} < 2$

108 The purity of the K $^\pm$  collections was estimated using the MC data, for which the true identity of each  
109 reconstructed K $^\pm$  particle is known. Therefore, the purity may be estimated as:

$$\text{Purity}(K^\pm) = \frac{N_{true}}{N_{reconstructed}} \quad (1)$$

110 Purity(K $^+$ )  $\approx$  Purity(K $^-$ )  $\approx$  97%

### 111 3.3 V0 Selection

112  $\Lambda$  ( $\bar{\Lambda}$ ) and K $_S^0$  are neutral particles which cannot be directly detected, but must instead be reconstructed  
113 through detection of their decay products, or daughters. This process is illustrated in Figure 1. In  
114 general, particles which are topologically reconstructed in this fashion are called V0 particles. The  
115 class AliFemtoV0TrackCutNSigmaFilter (which is an extension of AliFemtoV0TrackCut) is used to  
116 reconstruct the V0s.

117 In order to obtain a true and reliable signal, one must ensure good purity of the V0 collection. The purity  
118 of the collection is calculated as:

$$\text{Purity}_y = \frac{\text{Signal}}{\text{Signal} + \text{Background}} \quad (2)$$

119 To obtain both the signal and background, the invariant mass distribution ( $m_{inv}$ ) of all V0 candidates  
 120 must be constructed immediately before the final invariant mass cut. Examples of such distributions can  
 121 be found in Figures 3 and 5. It is vital that this distribution be constructed immediately before the final  
 122  $m_{inv}$  cut, otherwise it would be impossible to estimate the background. As shown in Figures 3 and 5, the  
 123 background is fit (with a polynomial) outside of the peak region of interest to obtain an estimate for the  
 124 background within the region. Within the  $m_{inv}$  cut limits, the background is the region below the fit while  
 125 the signal is the region above the fit.

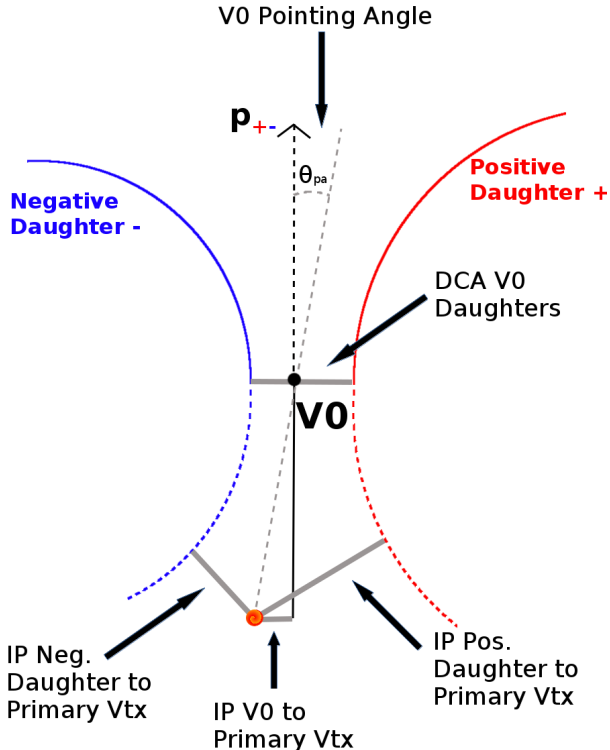


**Fig. 1:** V0 Reconstruction

126 **3.3.1  $\Lambda$  Reconstruction**

127 The following cuts were used to select good  $\Lambda$  ( $\bar{\Lambda}$ ) candidates:

128 1. Daughter Particle Cuts

- 129 (a) Cuts Common to Both Daughters
- 130     i.  $|\eta| < 0.8$   
 131     ii. SetTPCnclsDaughters(80)  
 132     iii. SetStatusDaughters(AliESDtrack::kTPCrefic)  
 133     iv. SetMaxDcaV0Daughters(0.4)

134 (b) Pion Specific Daughter Cuts

- 135     i.  $p_T > 0.16$   
 136     ii. DCA to prim vertex  $> 0.3$

137 (c) Proton Specific Daughter Cuts

- 138     i.  $p_T > 0.5(p) [0.3(\bar{p})] \text{ GeV}/c$   
 139     ii. DCA to prim vertex  $> 0.1$

140    2. V0 Cuts

- 141    (a)  $|\eta| < 0.8$   
 142    (b)  $p_T > 0.4$   
 143    (c)  $|m_{inv} - m_{PDG}| < 3.8 \text{ MeV}$   
 144    (d) DCA to prim. vertex  $< 0.5 \text{ cm}$   
 145    (e) Cosine of pointing angle  $> 0.9993$   
 146    (f) OnFlyStatus = false  
 147    (g) Decay Length  $< 60 \text{ cm}$

148    3. Shared Daughter Cut for V0 Collection

- 149    – Iterate through V0 collection to ensure that no daughter is used in more than one V0 candidate

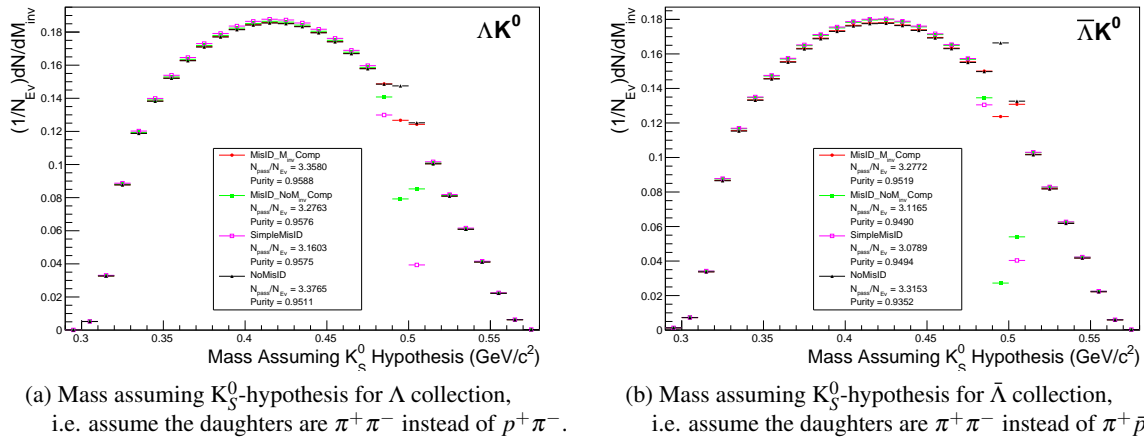


**Fig. 2:** Mass assuming  $K_S^0$ -hypothesis for V0 candidates passing all  $\Lambda$  (2a) and  $\bar{\Lambda}$  (2b) cuts. The “NoMisID” distribution (black triangles) uses the V0 finder without any attempt to remove misidentified  $K_S^0$ . The slight peak in the “NoMisID” distribution around  $m_{inv} = 0.5 \text{ GeV}/c^2$  contains misidentified  $K_S^0$  particles in our  $\Lambda(\bar{\Lambda})$  collection. “SimpleMisID” (pink squares) simply cuts out the entire peak, which throws away some good  $\Lambda$  and  $\bar{\Lambda}$  particles. “MisID\_NoM<sub>inv</sub>\_Comp” (green squares) uses the misidentification cut outlined in the text, but does not utilize the invariant mass comparison method. “MisID\_M<sub>inv</sub>\_Comp” (red circles) utilizes the full misidentification methods, and is currently used for this analysis. “ $N_{pass}/N_{ev}$ ” is the total number of  $\Lambda(\bar{\Lambda})$  particles found, normalized by the total number of events. The purity of the collection is also listed.

150    Figure 2a shows the mass assuming  $K_S^0$  hypothesis for the  $\Lambda$  collection, i.e. assume the daughters are  
 151     $\pi^+\pi^-$  instead of  $\pi^+\bar{p}^-$ . Figure 2b is a similar plot, but is for the  $\bar{\Lambda}$  collection, i.e. assume the daughters  
 152    are  $\pi^+\pi^-$  instead of  $\pi^+\bar{p}^-$ . The  $K_S^0$  contamination is visible, although not profound, in both in the slight  
 153    peaks around  $m_{inv} = 0.497 \text{ GeV}/c^2$ . If one simply cuts out the entire peak, good  $\Lambda$  particles will be  
 154    lost. Ideally, the  $\Lambda$  selection and  $K_S^0$  misidentification cuts are selected such that the peak is removed  
 155    from this plot while leaving the distribution continuous. To attempt to remove these  $K_S^0$  contaminations  
 156    without throwing away good  $\Lambda$  and  $\bar{\Lambda}$  particles, the following misidentification cuts are imposed; a  $\Lambda(\bar{\Lambda})$   
 157    candidate is rejected if all of the following criteria are satisfied:

- 158    –  $|m_{inv, K_S^0 \text{ Hypothesis}} - m_{PDG, K_S^0}| < 9.0 \text{ MeV}/c^2$   
 159    – Positive and negative daughters pass  $\pi$  daughter cut implemented for  $K_S^0$  reconstruction

$$160 \quad - \left| m_{inv, K_S^0 \text{ Hypothesis}} - m_{PDG, K_S^0} \right| < \left| m_{inv, \Lambda(\bar{\Lambda}) \text{ Hypothesis}} - m_{PDG, \Lambda(\bar{\Lambda})} \right|$$

161 Figure 3 shows the invariant mass ( $M_{inv}$ ) distribution of all  $\Lambda(\bar{\Lambda})$  candidates immediately before the final  
 162 invariant mass cut. These distributions are used to calculate the collection purities. The  $\Lambda$  and  $\bar{\Lambda}$  purities  
 163 are found to be: Purity( $\Lambda$ )  $\approx$  Purity( $\bar{\Lambda}$ )  $\approx$  95%.

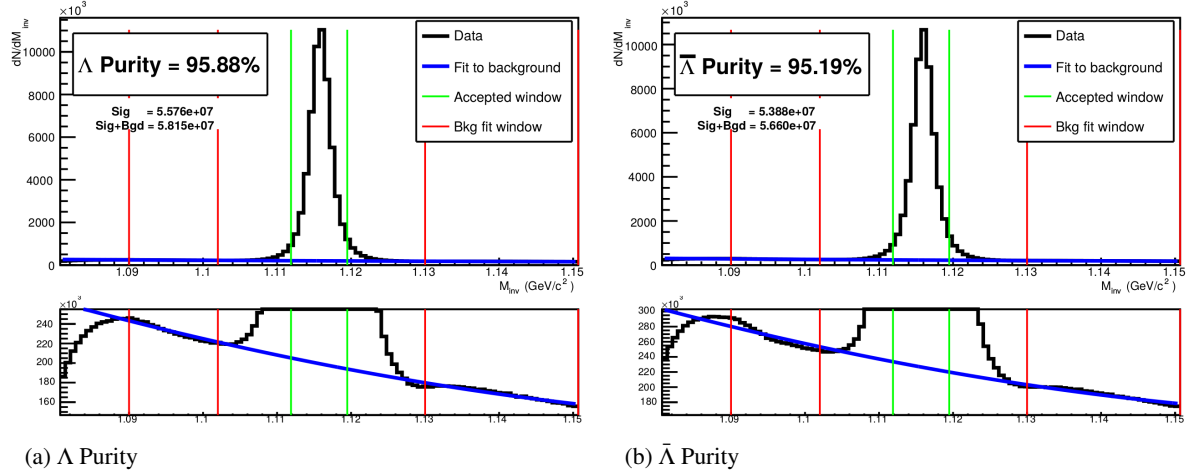


**Fig. 3:** Invariant mass ( $M_{inv}$ ) distribution of all  $\Lambda$  (a) and  $\bar{\Lambda}$  (b) candidates immediately before the final invariant mass cut. The bottom figures are zoomed to show the background with fit. The vertical green lines represent the  $M_{inv}$  cuts used in the analyses, the red vertical lines delineate the region over which the background was fit, and the blue line shows the background fit. These distributions are used to calculate the collection purities, Purity( $\Lambda$ )  $\approx$  Purity( $\bar{\Lambda}$ )  $\approx$  95%.

### 164 3.3.2 $K_S^0$ Reconstruction

165 The following cuts were used to select good  $K_S^0$  candidates:

166 1. Pion Daughter Cuts

- 167 (a)  $|\eta| < 0.8$
- 168 (b) SetTPCnclsDaughters(80)
- 169 (c) SetStatusDaughters(AliESDtrack::kTPCrefic)
- 170 (d) SetMaxDcaV0Daughters(0.3)
- 171 (e)  $p_T > 0.15$
- 172 (f) DCA to prim vertex  $> 0.3$

173 2.  $K_S^0$  Cuts

- 174 (a)  $|\eta| < 0.8$
- 175 (b)  $p_T > 0.2$
- 176 (c)  $m_{PDG} - 13.677 \text{ MeV} < m_{inv} < m_{PDG} + 2.0323 \text{ MeV}$
- 177 (d) DCA to prim. vertex  $< 0.3 \text{ cm}$
- 178 (e) Cosine of pointing angle  $> 0.9993$
- 179 (f) OnFlyStatus = false
- 180 (g) Decay Length  $< 30 \text{ cm}$

181     3. Shared Daughter Cut for V0 Collection

- 182       – Iterate through V0 collection to ensure that no daughter is used in more than one V0 candidate

183     As can be seen in Figure 4, some misidentified  $\Lambda$  and  $\bar{\Lambda}$  particles contaminate our  $K_S^0$  sample. Figure  
 184     4a shows the mass assuming  $\Lambda$ -hypothesis for the  $K_S^0$  collection, i.e. assume the daughters are  $p^+\pi^-$   
 185     instead of  $\pi^+\pi^-$ . Figure 4b is similar, but shows the mass assuming  $\bar{\Lambda}$  hypothesis for the collection,  
 186     i.e. assume the daughters are  $\pi^+\bar{p}^-$  instead of  $\pi^+\pi^-$ . The  $\Lambda$  contamination can be seen in 4a, and the  
 187      $\bar{\Lambda}$  contamination in 4b, in the peaks around  $m_{inv} = 1.115 \text{ GeV}/c^2$ . Additionally, the  $\bar{\Lambda}$  contamination is  
 188     visible in Figure 4a, and the  $\Lambda$  contamination visible in Figure 4b, in the region of excess around  $1.65$   
 189      $< m_{inv} < 2.1 \text{ GeV}/c^2$ . This is confirmed as the number of misidentified  $\Lambda$  particles in the sharp peak  
 190     of Figure 4a (misidentified  $\bar{\Lambda}$  particles in the sharp peak of Figure 4b) approximately equals the excess  
 191     found in the  $1.65 < m_{inv} < 2.1 \text{ GeV}/c^2$  region of Figure 4a (Figure 4b).

192     The peaks around  $m_{inv} = 1.115 \text{ GeV}/c^2$  in Figure 4 contain both misidentified  $\Lambda$  ( $\bar{\Lambda}$ ) particles and good  
 193      $K_S^0$ . If one simply cuts out the entire peak, some good  $K_S^0$  particles will be lost. Ideally, the  $K_S^0$  selection  
 194     and  $\Lambda(\bar{\Lambda})$  misidentification cuts can be selected such that the peak is removed from this plot while leaving  
 195     the distribution continuous. To attempt to remove these  $\Lambda$  and  $\bar{\Lambda}$  contaminations without throwing away  
 196     good  $K_S^0$  particles, the following misidentification cuts are imposed; a  $K_S^0$  candidate is rejected if all of  
 197     the following criteria are satisfied (for either  $\Lambda$  or  $\bar{\Lambda}$  hypothesis):

- 198       –  $|m_{inv, \Lambda(\bar{\Lambda}) \text{ Hypothesis}} - m_{PDG, \Lambda(\bar{\Lambda})}| < 9.0 \text{ MeV}/c^2$
- 199       – Positive daughter passes  $p^+(\pi^+)$  daughter cut implemented for  $\Lambda(\bar{\Lambda})$  reconstruction
- 200       – Negative daughter passes  $\pi^-(\bar{p}^-)$  daughter cut implemented by  $\Lambda(\bar{\Lambda})$  reconstruction
- 201       –  $|m_{inv, \Lambda(\bar{\Lambda}) \text{ Hypothesis}} - m_{PDG, \Lambda(\bar{\Lambda})}| < |m_{inv, K_S^0 \text{ Hypothesis}} - m_{PDG, K_S^0}|$

202     **3.4 Cascade Reconstruction**

203     Our motivation for studying  $\Xi K^\pm$  systems is to hopefully better understand the striking difference in the  
 204      $\Lambda K^+$  and  $\Lambda K^-$  data at low  $k^*$  (Figure 14).

205     The reconstruction of  $\Xi$  particles is one step above V0 reconstruction. V0 particles are topologically  
 206     reconstructed by searching for the charged daughters' tracks into which they decay. With  $\Xi$  particles, we  
 207     search for the V0 particle and charged daughter into which the  $\Xi$  decays. In the case of  $\Xi^-$ , we search  
 208     for the  $\Lambda$  (V0) and  $\pi^-$  (track) daughters. We will refer to this  $\pi$  as the “bachelor  $\pi$ ”.

209     The following cuts were used to select good  $\Xi^- (\bar{\Xi}^+)$  candidates:

210       1. V0 Daughter Reconstruction

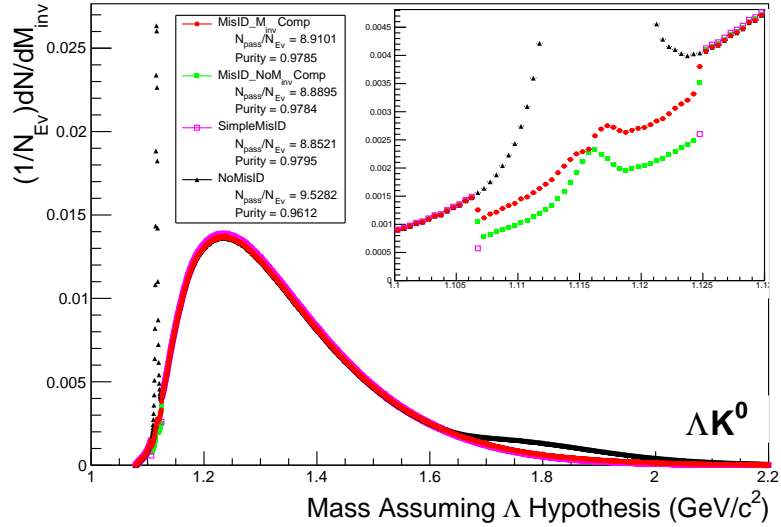
211           (a) V0 Daughter Particle Cuts

212              i. Cuts Common to Both Daughters

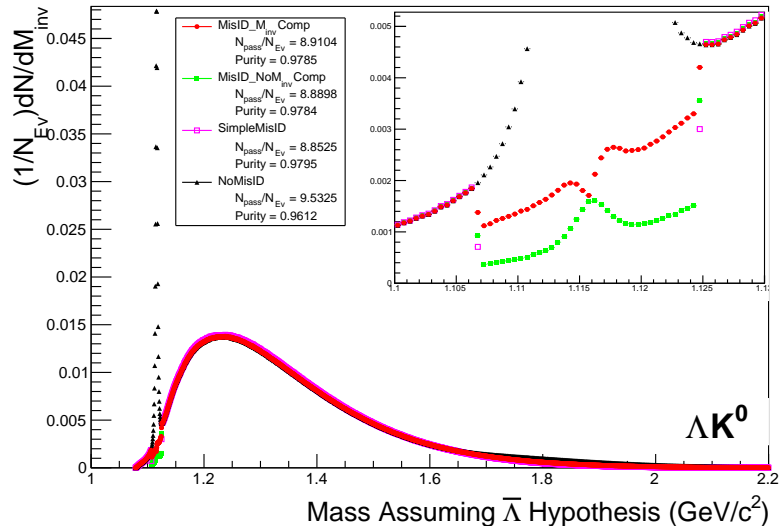
- 213               A.  $|\eta| < 0.8$
- 214               B. SetTPCnclsDaughters(80)
- 215               C. SetStatusDaughters(AliESDtrack::kTPCrefic)
- 216               D. SetMaxDcaV0Daughters(0.4)

217              ii. Pion Specific Daughter Cuts

- 218               A.  $p_T > 0.16$



(a) Mass assuming  $\Lambda$ -hypothesis for  $K_S^0$  collection, i.e. assume the daughters are  $p^+ \pi^-$  instead of  $\pi^+ \pi^-$ .



(b) Mass assuming  $\bar{\Lambda}$ -hypothesis for  $K_S^0$  collection, i.e. assume the daughters are  $p^+ \bar{p}^-$  instead of  $\pi^+ \pi^-$ .

**Fig. 4:** Mass assuming  $\Lambda$ -hypothesis (4a) and  $\bar{\Lambda}$ -hypothesis (4b) for  $K_S^0$  collection. The “NoMisID” distribution (black triangles) uses the V0 finder without any attempt to remove misidentified  $\Lambda$  and  $\bar{\Lambda}$ . The peak in the “NoMisID” distribution around  $m_{\text{inv}} = 1.115 \text{ GeV}/c^2$  contains misidentified  $\Lambda$  (4a) and  $\bar{\Lambda}$  (4b) particles in our  $K_S^0$  collection. “SimpleMisID” (pink squares) simply cuts out the entire peak, which throws away some good  $K_S^0$  particles. “MisID\_NoM<sub>inv</sub>Comp” (green squares) uses the misidentification cut outlined in the text, but does not utilize the invariant mass comparison method. “MisID\_M<sub>inv</sub>Comp” (red circles) utilizes the full misidentification methods, and is currently used for this analysis. “ $N_{\text{pass}}/N_{\text{ev}}$ ” is the total number of  $K_S^0$  particles found, normalized by the total number of events. The purity of the collection is also listed. Also note, the relative excess of the “NoMisID” distribution around  $1.65 < m_{\text{inv}} < 2.1 \text{ GeV}/c^2$  shows misidentified  $\bar{\Lambda}$  (4a) and  $\Lambda$  (4b) particles in our  $K_S^0$  collection.

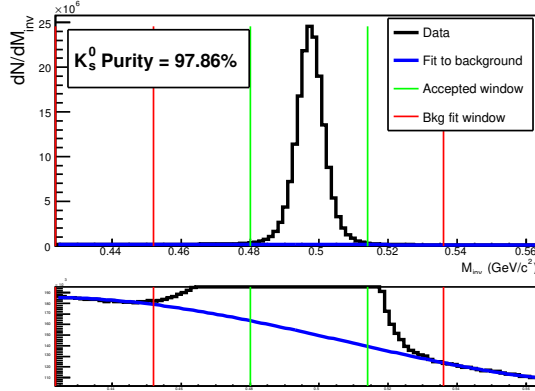


**Fig. 5:** Invariant mass ( $M_{inv}$ ) distribution of all  $K_s^0$  candidates immediately before the final invariant mass cut. The bottom figure is zoomed to show the background with fit. The vertical green lines represent the  $M_{inv}$  cut used in the analyses, the red vertical lines delineate the region over which the background was fit, and the blue line shows the background fit. This distribution is used to calculate the collection purity,  $Purity(K_s^0) \approx 98\%$ .

221                   A.  $p_T > 0.5(p)[0.3(\bar{p})] \text{ GeV}/c$

222                   B. DCA to prim vertex  $> 0.1$

223                   (b) V0 Cuts

224                   i.  $|\eta| < 0.8$

225                   ii.  $p_T > 0.4 \text{ GeV}/c$

226                   iii.  $|m_{inv} - m_{PDG}| < 3.8 \text{ MeV}$

227                   iv. DCA to prim. vertex  $> 0.2 \text{ cm}$

228                   v. Cosine of pointing angle to  $\Xi$  decay vertex  $> 0.9993$

229                   vi. OnFlyStatus = false

230                   vii. Decay Length  $< 60 \text{ cm}$

231                   viii. The misidentification cuts described in Section 3.3.1 are utilized

232                   2. Bachelor  $\pi$  Cuts

233                   (a)  $|\eta| < 0.8$

234                   (b)  $p_T < 100 \text{ GeV}/c$

235                   (c) DCA to prim vertex  $> 0.1 \text{ cm}$

236                   (d) SetTPCnclsDaughters(70)

237                   (e) SetStatusDaughters(AliESDtrack::kTPCrefic)

238                   3.  $\Xi$  Cuts

239                   (a)  $|\eta| < 0.8$

240                   (b)  $0.8 < p_T < 100 \text{ GeV}/c$

241                   (c)  $|m_{inv} - m_{PDG}| < 3.0 \text{ MeV}$

242                   (d) DCA to prim. vertex  $< 0.3 \text{ cm}$

243                   (e) Cosine of pointing angle  $> 0.9992$

244                   4. Shared Daughter Cut for  $\Xi$  Collection

- 245                   – Iterate through  $\Xi$  collection to ensure that no daughter is used in more than one  $\Xi$  candidate

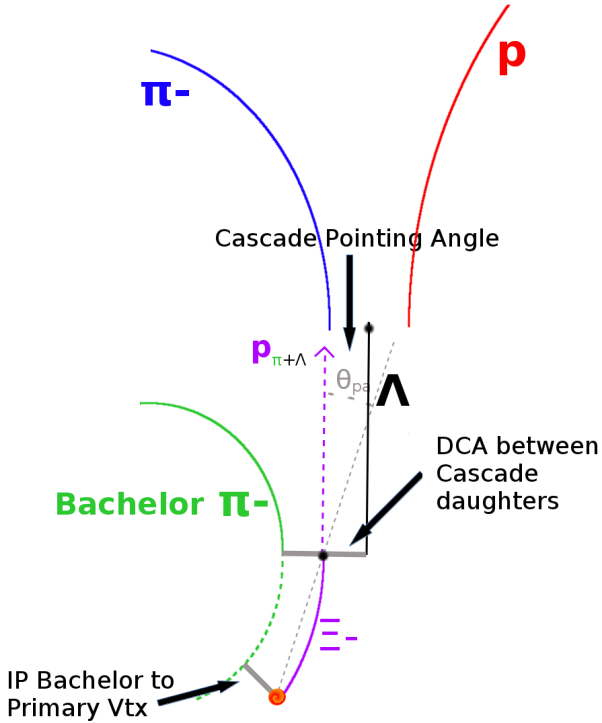


**Fig. 6:**  $\Xi$  Reconstruction

246 The purity of our  $\Xi$  and  $\bar{\Xi}$  collections are calculated just as those of our V0 collections 3.3. Figure 7,  
247 which is used to calculate the purity, shows the  $m_{inv}$  distribution of our  $\Xi(\bar{\Xi})$  candidates just before the  
248 final  $m_{inv}$  cut. Currently, we have Purity( $\Xi^-$ )  $\approx$  90% and Purity( $\bar{\Xi}^+$ )  $\approx$  92%.

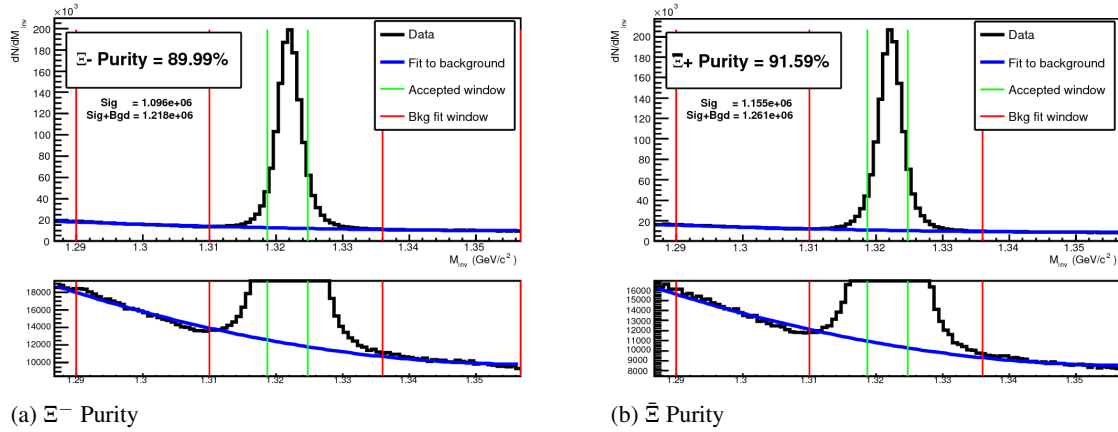


**Fig. 7:**  $\Xi^- (\bar{\Xi}^+)$  Purity 0-10%: Purity( $\Xi^-$ )  $\approx$  90% and Purity( $\bar{\Xi}^+$ )  $\approx$  92%.

### 249 3.5 Pair Selection

250 It is important to obtain true particle pairs in the analysis. In particular, contamination from pairs con-  
251 structed with split or merged tracks, and pairs sharing daughters, can introduce an artificial signal into  
252 the correlation function, obscuring the actual physics.

#### 253 1. Shared Daughter Cut for Pairs

##### 254 (a) V0-V0 Pairs (i.e. $\Lambda(\bar{\Lambda})K_S^0$ analyses)

- Remove all pairs which share a daughter
    - Ex.  $\Lambda$  and  $K_S^0$  particles which share a  $\pi^-$  daughter are not included
- (b) V0-Track Pairs (i.e.  $\Lambda(\bar{\Lambda})K^\pm$  analyses)
- Remove pairs if Track is also used as a daughter of the V0
    - In these analyses, this could only occur if, for instance, a  $K$  is misidentified as a  $\pi$  or  $p$  in the V0 reconstruction
- (c)  $\Xi$ -Track Pairs
- Remove pairs if Track is also used as a daughter of the  $\Xi$ 
    - In these analyses, this could only occur if, for instance, a  $K$  is misidentified as a  $\pi$  or  $p$  in the V0 reconstruction, or misidentified as bachelor  $\pi$ .
  - Remove pair if bachelor  $\pi$  is also a daughter of the  $\Lambda$ 
    - This is not a pair cut, but is included here because this cut occurs in the AliFemtoXiTrackPairCut class

## 2. Average Separation Cuts

- Used to cut out splitting and merging effects
- The motivation for these cuts can be seen in Figures 8, 9, and 10, in which average separation correlation functions are presented

- (a)  $\Lambda(\bar{\Lambda})K_S^0$  Analyses
- Average separation  $> 6 \text{ cm}$  for like charge sign daughters
    - ex.  $p$  daughter of  $\Lambda$  and  $\pi^+$  daughter of  $K_S^0$
    - No cut for unlike-sign daughters
- (b)  $\Lambda(\bar{\Lambda})K^\pm$  Analyses
- Average Separation  $> 6 \text{ cm}$  for daughter of  $\Lambda(\bar{\Lambda})$  sharing charge sign of  $K^\pm$ 
    - ex. in  $\Lambda K^+$  analysis,  $p$  daughter of  $\Lambda$  with  $K^+$
    - No cut for unlike signs
- (c)  $\Xi(\bar{\Xi})K^\pm$  Analyses
- Average Separation  $> 8.0 \text{ cm}$  for any daughter of  $\Xi$  sharing charge sign of  $K^\pm$ 
    - ex. in  $\Xi^- K^-$  analysis,  $\pi^-$  daughter of  $\Lambda$  daughter with  $K^-$ , and bachelor  $\pi^-$  daughter with  $K^-$
    - No cut for unlike signs

## 4 Correlation Functions

This analysis studies the momentum correlations of both  $\Lambda$ - $K$  and  $\Xi$ - $K$  pairs using the two-particle correlation function, defined as  $C(k^*) = A(k^*)/B(k^*)$ , where  $A(k^*)$  is the signal distribution,  $B(k^*)$  is the reference (or background) distribution, and  $k^*$  is the momentum of one of the particles in the pair rest frame. In practice,  $A(k^*)$  is constructed by binning in  $k^*$  pairs from the same event. Ideally,  $B(k^*)$  is similar to  $A(k^*)$  in all respects excluding the presence of femtoscopic correlations [2]; as such,  $B(k^*)$  is used to divide out the phase-space effects, leaving only the femtoscopic effects in the correlation function.

In practice,  $B(k^*)$  is obtained by forming mixed-event pairs, i.e. particles from a given event are paired with particles from  $N_{mix} (= 5)$  other events, and these pairs are then binned in  $k^*$ . In forming the background distribution, it is important to mix only similar events; mixing events with different phase-spaces

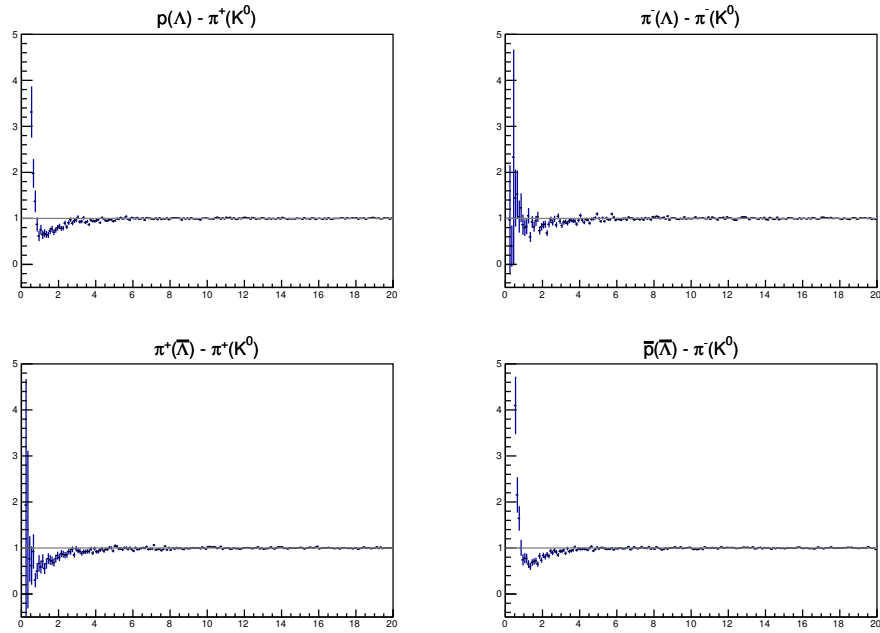


**Fig. 8:** Average separation (cm) correlation functions of  $\Lambda(\bar{\Lambda})$  and  $K_S^0$  Daughters. Only like-sign daughter pairs are shown (the distributions for unlike-signs were found to be flat). The title of each subfigure shows the daughter pair, as well as the mother of each daughter (in “()”), ex. top left is  $p$  from  $\Lambda$  with  $\pi^+$  from  $K_S^0$ .

295 can lead to artificial signals in the correlation function. Therefore, in this analysis, we mix events with  
 296 primary vertices within 2 cm and centralities within 5% of each other. Also note, a vertex correction is  
 297 also applied to each event, which essentially recenters the primary vertices to  $z = 0$ .

298 This analysis presents correlation functions for three centrality bins (0-10%, 10-30%, and 30-50%),  
 299 and is currently pair transverse momentum ( $k_T = 0.5|\mathbf{p}_{T,1} + \mathbf{p}_{T,2}|$ ) integrated (i.e. not binned in  $k_T$ ).  
 300 The correlation functions are constructed separately for the two magnetic field configurations, and are  
 301 combined using a weighted average:

$$C_{combined}(k^*) = \frac{\sum_i w_i C_i(k^*)}{\sum_i w_i} \quad (3)$$

302 where the sum runs over the correlation functions to be combined, and the weight,  $w_i$ , is the number of  
 303 numerator pairs in  $C_i(k^*)$ . Here, the sum is over the two field configurations.

304 Figures 11, 12, and 13 show the correlation functions for all centralities studied for  $\Lambda K_S^0(\bar{\Lambda} K_S^0)$ ,  $\Lambda K^+(\bar{\Lambda} K^-)$ ,  
 305 and  $\Lambda K^-(\bar{\Lambda} K^+)$ , respectively. All were normalized in the range  $0.32 < k^* < 0.4$  GeV/c.

## 306 5 Fitting

### 307 5.1 Model: $\Lambda K_S^0$ , $\Lambda K^\pm$ , $\Xi^{ch} K_S^0$

308 The two-particle relative momentum correlation function may be written theoretically by the Koonin-  
 309 Pratt equation [3, 4]:

$$C(\mathbf{k}^*) = \int S(\mathbf{r}^*) |\Psi_{\mathbf{k}^*}(\mathbf{r}^*)|^2 d^3 \mathbf{r}^* \quad (4)$$

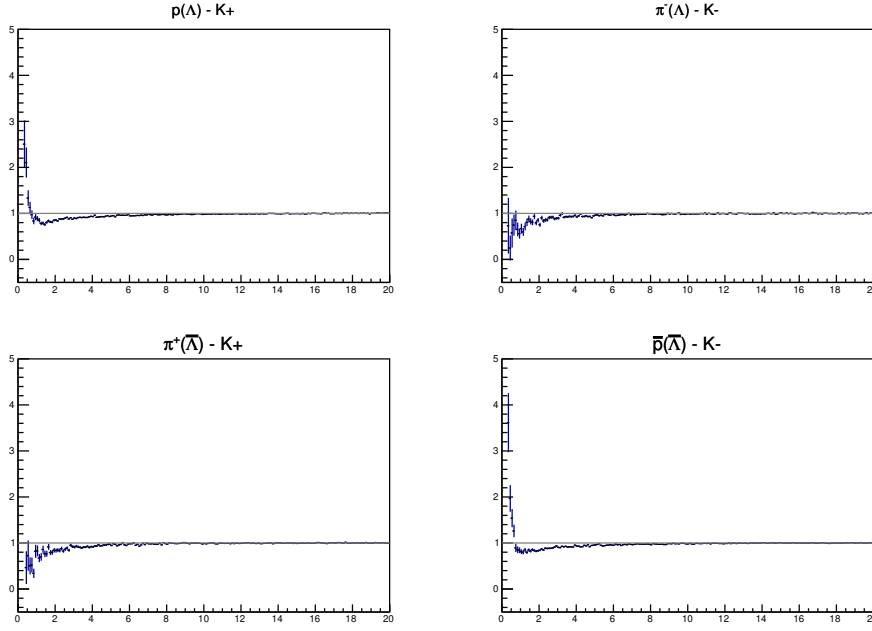


**Fig. 9:** Average separation (cm) correlation functions of  $\Lambda(\bar{\Lambda})$  Daughter and  $K^\pm$ . Only like-sign pairs are shown (unlike-signs were flat). In the subfigure titles, the particles in “()” represent the mothers, ex. top left is  $p$  from  $\Lambda$  with  $K^+$ .

310 In the absence of Coulomb effects, and assuming a spherically gaussian source of width  $R$ , the 1D  
 311 femtoscopic correlation function can be calculated analytically using:

$$C(k^*) = 1 + \lambda [C_{QI}(k^*) + C_{FSI}(k^*)] \quad (5)$$

312  $C_{QI}$  describes plane-wave quantum interference:

$$C_{QI}(k^*) = \alpha \exp(-4k^{*2}R^2) \quad (6)$$

313 where  $\alpha = (-1)^{2j}/(2j+1)$  for identical particles with spin  $j$ , and  $\alpha = 0$  for non-identical particles.  
 314 Obviously,  $\alpha = 0$  for all analyses presented in this note.  $C_{FSI}$  describes the s-wave strong final state  
 315 interaction between the particles:

$$\begin{aligned} C_{FSI}(k^*) &= (1 + \alpha) [\frac{1}{2} |\frac{f(k^*)}{R}|^2 (1 - \frac{d_0}{2\sqrt{\pi}R}) + \frac{2\mathbb{R}f(k^*)}{\sqrt{\pi}R} F_1(2k^*R) - \frac{\mathbb{I}f(k^*)}{R} F_2(2k^*R)] \\ f(k^*) &= (\frac{1}{f_0} + \frac{1}{2} d_0 k^{*2} - ik^*)^{-1}; \quad F_1(z) = \int_0^z \frac{e^{x^2-z^2}}{z} dx; \quad F_2(z) = \frac{1-e^{-z^2}}{z} \end{aligned} \quad (7)$$

316 where  $R$  is the source size,  $f(k^*)$  is the s-wave scattering amplitude,  $f_0$  is the complex scattering length,  
 317 and  $d_0$  is the effective range of the interaction.

318 The code developed to fit the data is called “LednickyFitter”, and utilizes the ROOT TMinuit implemen-  
 319 tation of the MINUIT fitting package. In short, given a function with a number of parameters, the fitter  
 320 explores the parameter space searching for the minimum of the equation. In this implementation, the  
 321 function to be minimized should represent the difference between the measure and theoretical corre-  
 322 lation functions. However, a simple  $\chi^2$  test is inappropriate for fitting correlation functions, as the ratio  
 323 two Poisson distributions does not result in a Poisson distribution. Instead, a log-likelihood fit function  
 324 of the following form is used [2]:

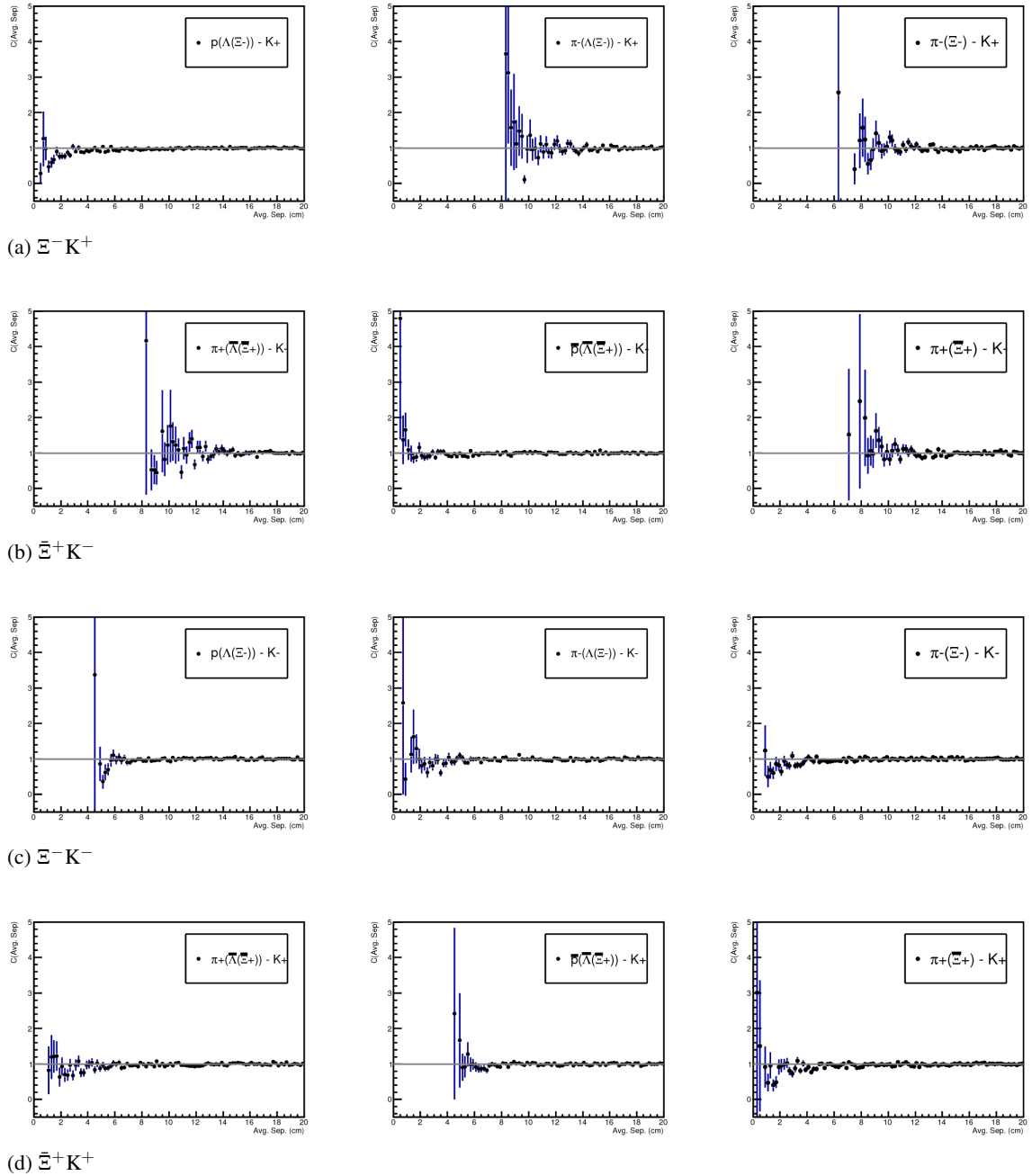


**Fig. 10:** Average separation (cm) correlation functions of  $\Xi$  Daughter and  $K^\pm$ . In the subfigure titles, the particles in “()” represent the mothers, ex. top left is  $p$  from  $\Lambda$  from  $\Xi^-$  with  $K^+$ .

$$\chi_{PML}^2 = -2 \left[ A \ln \left( \frac{C(A+B)}{A(C+1)} \right) + B \ln \left( \frac{A+B}{B(C+1)} \right) \right] \quad (8)$$

325 where  $A$  is the experimental signal distribution (numerator),  $B$  is the experimental background distribution  
326 (denominator), and  $C$  is the theoretical fit correlation function.

327 The LednickyFitter uses Equations 5 – 7 to build the theoretical fit, and Equation 8 as the statistic quantifying  
328 the quality of the fit. The parameters to be varied by MINUIT are:  $\lambda$ ,  $R$ ,  $f_0$  ( $\mathbb{R}f_0$  and  $\mathbb{I}f_0$  separately),  
329  $d_0$ , and normalization  $N$ . The fitter currently includes methods to correct for momentum resolution and  
330 a non-flat background. These corrections are applied to the fit function, the data is never touched. The

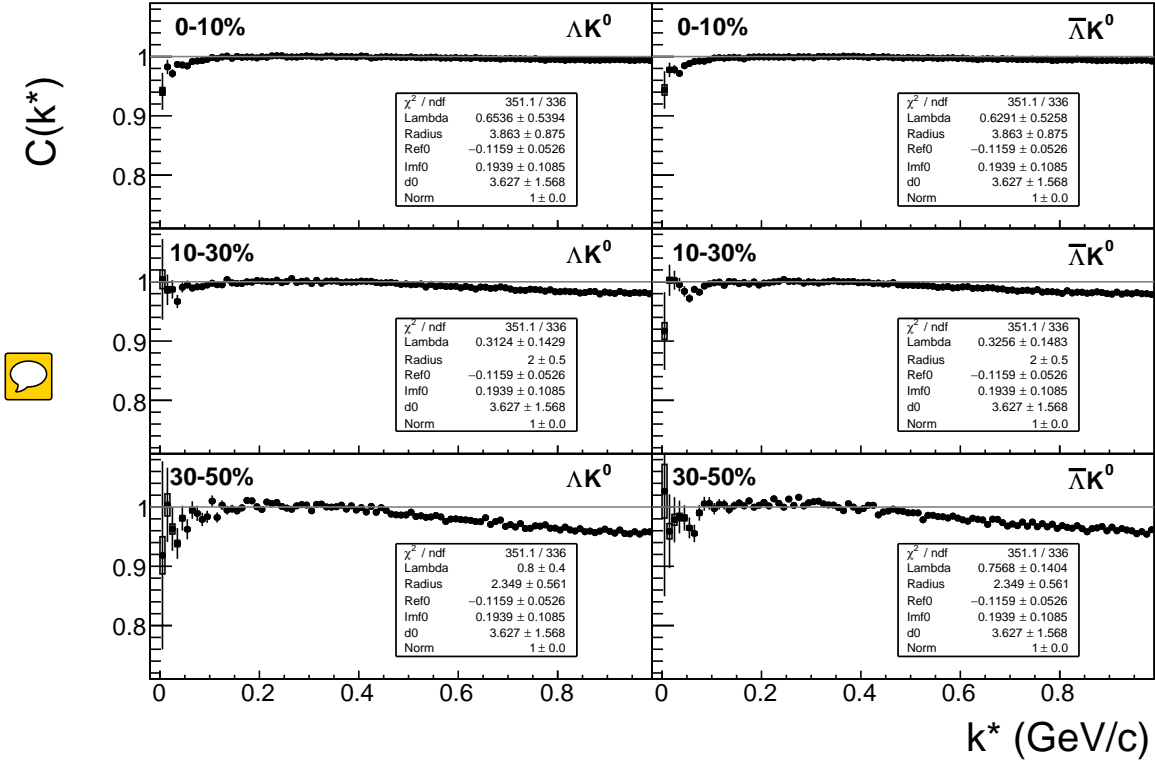


**Fig. 11:**  $\Lambda K_S^0$  (left) and  $\bar{\Lambda} K_S^0$  (right) correlation functions for 0-10% (top), 10-30%(middle), and 30-50%(bottom) centralities. The lines represent the statistical errors, while the boxes represent the systematic errors.

fitter is able to share parameters between different analyses and fit all simultaneously.  
 In a typical fit, a given pair is fit with its conjugate (ex.  $\Lambda K^+$  with  $\bar{\Lambda} K^-$ ) across all centralities (0-10%, 10-30%, 30-50%), for a total of 6 simultaneous analyses. Each analysis has a unique  $\lambda$  and normalization parameter. The radii are shared between analyses of like centrality, as these should have similar source sizes. The scattering parameters ( $\mathbb{R} f_0$ ,  $\mathbb{I} f_0$ ,  $d_0$ ) are shared amongst all.

Figures 29, 31, and 33 (36, 38, and 40, or 43, 45, and 47), in Section 7, show experimental data with fits for all studied centralities for  $\Lambda K_S^0$  with  $\bar{\Lambda} K_S^0$ ,  $\Lambda K^+$  with  $\bar{\Lambda} K^-$ , and  $\Lambda K^-$  with  $\bar{\Lambda} K^+$ , respectively. In the figures, the black solid line represents the “raw” fit, i.e. not corrected for momentum resolution effects nor non-flat background. The green line shows the fit to the non-flat background. The purple points show the fit after momentum resolution, non-flat background, and residual correlations (if applicable) corrections have been applied. The initial values of the parameters is listed, as well as the final fit values with uncertainties. 

## 5.2 Model: $\Xi^{ch} K^{ch}$

When fitting the  $\Xi^-(\bar{\Xi}^+)K^\pm$  results, it is necessary to include both strong and Coulomb effects. In this case, Equation 5 is no longer valid, and, in fact, there is no analytical form with which to fit. Therefore, we must begin with the wave function describing the pair interaction, and simulate many particle pairs to obtain a theoretical fit correlation function. The code developed to achieve this functionality is called “CoulombFitter”. Currently, in order to generate the statistics needed for a stable fit, we find that  $\sim 10^4$  simulated pairs per 10 MeV bin are necessary. Unfortunately, the nature of this process means that the “CoulombFitter” takes much longer to run than the “LednickyFitter” of Section 5.1.

The two-particle correlation function may be written as:

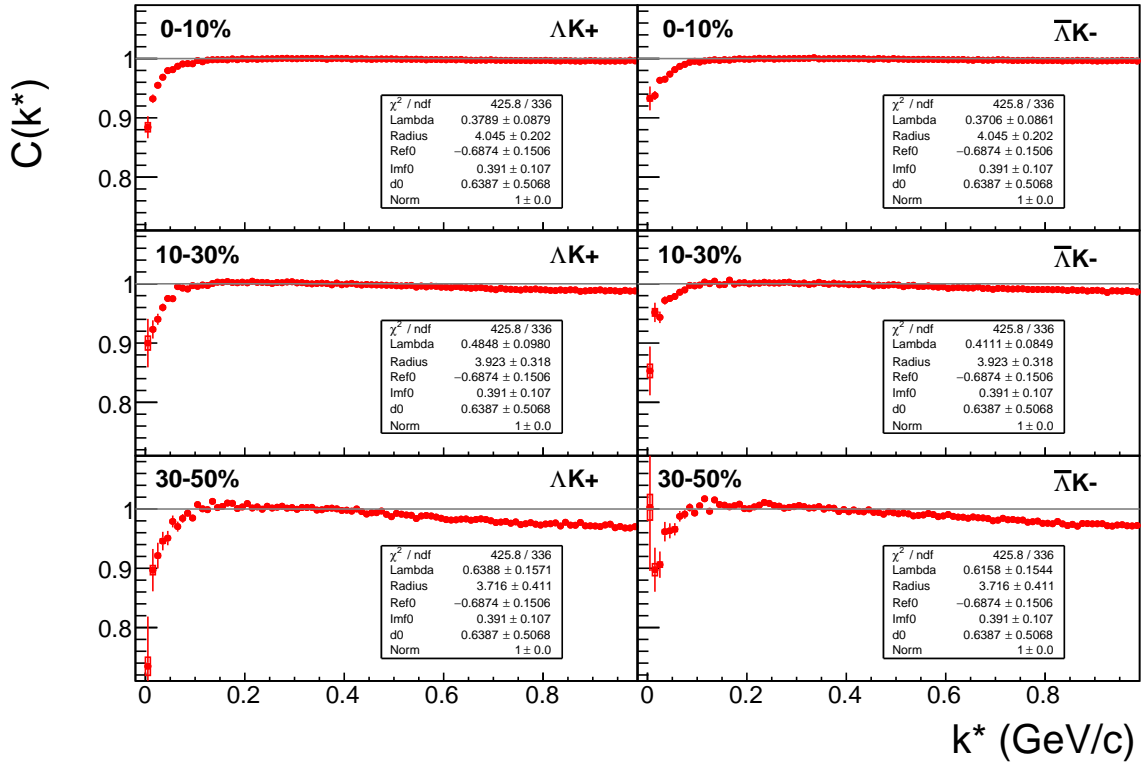


**Fig. 12:**  $\Lambda K^+$  (left) and  $\bar{\Lambda} K^-$  (right) correlation functions for 0-10% (top), 10-30% (middle), and 30-50% (bottom) centralities. The lines represent the statistical errors, while the boxes represent the systematic errors.

$$C(\mathbf{k}^*) = \sum_S \rho_S \int S(\mathbf{r}^*) |\Psi_{\mathbf{k}^*}^S(\mathbf{r}^*)|^2 d^3 \mathbf{r}^* \quad (9)$$

where  $\rho_S$  is the normalized emission probability of particles in a state with spin  $S$ ,  $S(\mathbf{r}^*)$  is the pair emission source distribution (assumed to be Gaussian), and  $\Psi_{\mathbf{k}^*}^S(\mathbf{r}^*)$  is the two-particle wave-function including both strong and Coulomb interactions [5]:

$$\Psi_{\mathbf{k}^*}(\mathbf{r}^*) = e^{i\delta_c} \sqrt{A_c(\eta)} [e^{i\mathbf{k}^* \cdot \mathbf{r}^*} F(-i\eta, 1, i\xi) + f_c(k^*) \frac{\tilde{G}(\rho, \eta)}{r^*}] \quad (10)$$

where  $\rho = k^* r^*$ ,  $\eta = (k^* a_c)^{-1}$ ,  $\xi = \mathbf{k}^* \cdot \mathbf{r}^* + k^* r^* \equiv \rho(1 + \cos \theta^*)$ , and  $a_c = (\mu z_1 z_2 e^2)^{-1}$  is the two-particle Bohr radius (including the sign of the interaction).  $\delta_c$  is the Coulomb s-wave phase shift,  $A_c(\eta)$  is the Coulomb penetration factor,  $\tilde{G} = \sqrt{A_c}(G_0 + iF_0)$  is a combination of the regular ( $F_0$ ) and singular ( $G_0$ ) s-wave Coulomb functions.  $f_c(k^*)$  is the s-wave scattering amplitude:

$$f_c(k^*) = [\frac{1}{f_0} + \frac{1}{2} d_0 k^{*2} - \frac{2}{a_c} h(\eta) - ik^* A_c(\eta)]^{-1} \quad (11)$$

where, the “h-function”,  $h(\eta)$ , is expressed through the digamma function,  $\psi(z) = \Gamma'(z)/\Gamma(z)$  as:

$$h(\eta) = 0.5[\psi(i\eta) + \psi(-i\eta) - \ln(\eta^2)] \quad (12)$$

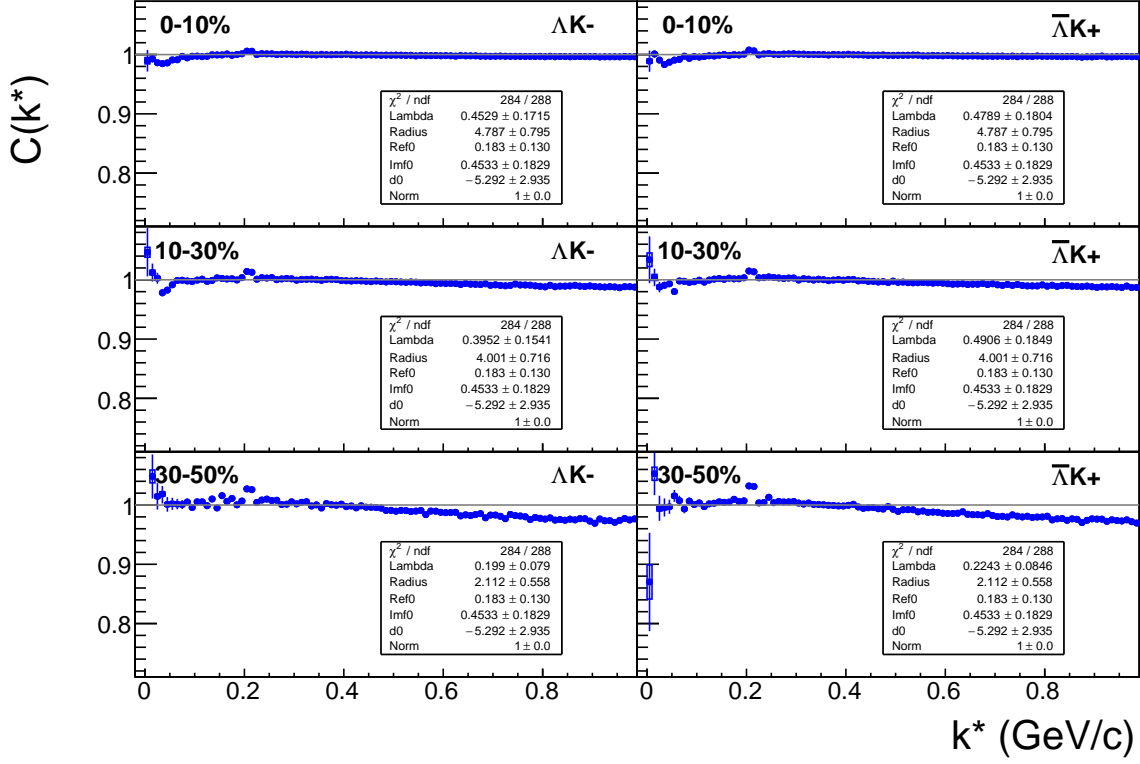


**Fig. 13:**  $\Lambda K^-$  (left) and  $\bar{\Lambda} K^+$  (right) correlation functions for 0-10% (top), 10-30% (middle), and 30-50% (bottom) centralities. The lines represent the statistical errors, while the boxes represent the systematic errors. The peak at  $k^* \approx 0.2$  GeV/c is due to the  $\Omega^-$  resonance.

360 Unfortunately, with this analysis, we are not sensitive to, and therefore not able to distinguish between,  
 361 the iso-spin singlet and triplet states. We proceed with our analysis, but the results must be interpreted  
 362 as iso-spin averaged scattering parameters.

363 As stated before, to generate a fit correlation function, we must simulate a large number of pairs, calculate  
 364 the wave-function, and average  $\Psi^2$  over all pairs in a given  $k^*$  bin. Essentially, we calculate Equation 9  
 365 by hand:

$$\begin{aligned}
 C(\mathbf{k}^*) &= \sum_S \rho_S \int S(\mathbf{r}^*) |\Psi_{\mathbf{k}^*}^S(\mathbf{r}^*)|^2 d^3 \mathbf{r}^* \\
 &\rightarrow C(|\mathbf{k}^*|) \equiv C(k^*) = \sum_S \rho_S \langle |\Psi^S(\mathbf{k}_i^*, \mathbf{r}_i^*)|^2 \rangle_i \\
 &\rightarrow C(k^*) = \lambda \sum_S \rho_S \langle |\Psi^S(\mathbf{k}_i^*, \mathbf{r}_i^*)|^2 \rangle_i + (1 - \lambda)
 \end{aligned} \tag{13}$$

366 where  $\langle \rangle_i$  represents an average over all pairs in a given  $k^*$  bin.

367 In summary, for a given  $k^*$  bin, we must draw  $N_{\text{pairs}} \sim 10^4$  pairs, and for each pair:

- 368 1. Draw a random  $\mathbf{r}^*$  vector according to our Gaussian source distribution  $S(\mathbf{r}^*)$   
 369 2. Draw a random  $\mathbf{k}^*$  vector satisfying the  $|\mathbf{k}^*|$  restriction of the bin

370 – We draw from real  $k^*$  vectors obtained from the data

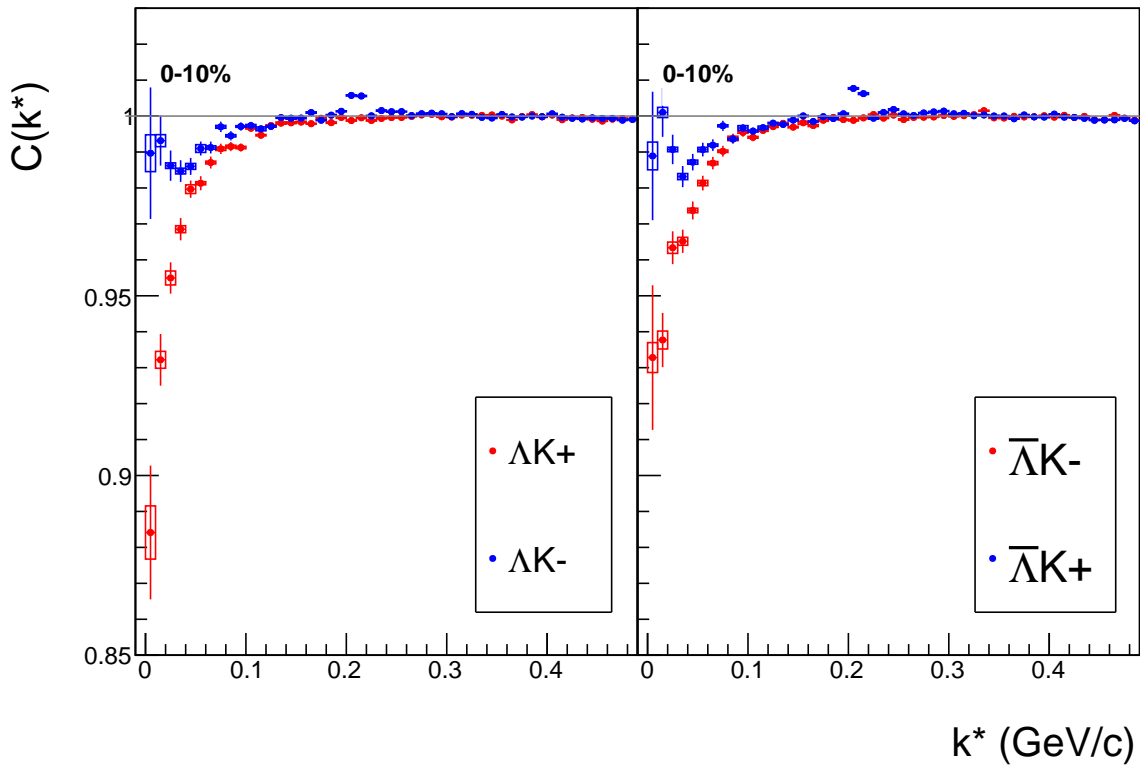


**Fig. 14:** Correlation Functions:  $\Lambda K^+$  vs  $\Lambda K^-$  ( $\bar{\Lambda} K^+$  vs  $\bar{\Lambda} K^-$ ) for 0-10% centrality. The peak in  $\Lambda K^- (\bar{\Lambda} K^+)$  at  $k^* \approx 0.2$  GeV/c is due to the  $\Omega^-$  resonance. The lines represent the statistical errors. (NOTE: This figure is slightly dated, and a new one will be generated which includes both statistical and systematic uncertainties)

371 – However, we find that drawing from a distribution flat in  $k^*$  gives similar results

372     3. Construct the wave-function  $\Psi$

373 After all pairs for a given  $k^*$  bin are simulated and wave-functions obtained, the results are averaged to  
374 give the fit result.

375 Construction of the wave-functions, Equation 10, involves a number of complex functions not included  
376 in standard C++ or ROOT libraries (namely,  $h(\eta)$ ,  $\tilde{G}(\rho, \eta)$ ), and  $F(-i\eta, 1, i\xi)$ . These functions were  
377 even difficult to find and implement from elsewhere. Our solution was to embed a Mathematica kernel  
378 into our C++ code to evaluate these functions. However, having Mathematica work on-the-fly with the  
379 fitter was far too time consuming (fitter would have taken day, maybe weeks to finish). Our solution  
380 was to use Mathematica to create matrices representing these functions for different parameter values.  
381 During fitting, these matrices were then interpolated and the results used to build the wave-functions.  
382 This method decreased the running time dramatically, and we are not able to generate results in under  $\sim$   
383 1 hour. This process will be explained in more detail in future versions of the note.

384     **5.3 Momentum Resolution Corrections**

385 Finite track momentum resolution causes the reconstructed momentum of a particle to smear around the  
386 true value. This, of course, also holds true for V0 particles. The effect is propagated up to the pairs  
387 of interest, which causes the reconstructed relative momentum ( $k_{Rec}^*$ ) to differ from the true momentum  
388 ( $k_{True}^*$ ). Smearing of the momentum typically will result in a suppression of the signal.

389 The effect of finite momentum resolution can be investigated using the MC data, for which both the true

and reconstructed momenta are available. Figure 15 shows sample  $k_{True}^*$  vs.  $k_{Rec}^*$  plots for  $\Lambda(\bar{\Lambda})K^\pm$  0-10% analyses; Figure 15a was generated using same-event pairs, while Figure 15b was generated using mixed-event pairs (with  $N_{mix} = 5$ ).

If there are no contaminations in our particle collection, the plots in Figure 15 should be smeared around  $k_{True}^* = k_{Rec}^*$ ; this is mostly true in our analyses. However, there are some interesting features of our results which demonstrate a small (notice the log-scale on the z-axis) contamination in our particle collection. The structure around  $k_{Rec}^* = k_{True}^* - 0.15$  is mainly caused by  $K_S^0$  contamination in our  $\Lambda(\bar{\Lambda})$  sample. The remaining structure not distributed about  $k_{Rec}^* = k_{True}^*$  is due to  $\pi$  and  $e$  contamination in our  $K^\pm$  sample. These contaminations are more visible in Figure 16, which show  $k_{Rec}^*$  vs.  $k_{True}^*$  plots (for a small sample of the  $\Lambda K^\pm$  0-10% central analysis), for which the MC truth (i.e. true, known identity of the particle) was used to eliminate misidentified particles in the  $K^+$ (a) and  $\Lambda$ (b) collections. (NOTE: This is an old figure and is for a small sample of the data. A new version will be generated shortly. It, nonetheless, demonstrates the point well).

Information gained from looking at  $k_{Rec}^*$  vs  $k_{True}^*$  can be used to apply corrections to account for the effects of finite momentum resolution on the correlation functions. A typical method involves using the MC HIJING data to build two correlation functions,  $C_{Rec}(k^*)$  and  $C_{True}(k^*)$ , using the generator-level momentum ( $k_{True}^*$ ) and the measured detector-level momentum ( $k_{Rec}^*$ ). The data is then corrected by multiplying by the ratio,  $C_{True}/C_{Rec}$ , before fitting. This essentially unsmears the data, which that can be compared directly to theoretical predictions and fits. Although this is conceptually simple, there are a couple of big disadvantages to this method. First, HIJING does not incorporate final-state interactions, so weights must be used when building same-event (numerator) distributions. These weights account for the interactions, and, in the absence of Coulomb interactions, can be calculated using Eq. 5. Of course, these weights are valid only for a particular set of fit parameters. Therefore, in the fitting process, during which the fitter explores a large parameter set, the corrections will not remain valid. As such, applying the momentum resolution correction and fitting becomes a long and drawn out iterative process. An initial parameter set is obtained (through fitting without momentum resolution corrections, theoretical models, or a good guess), then the MC data is run over to obtain the correction factor, the data is fit using the correction factor, a refined parameter set is extracted, the MC data is run over again to obtain the new correction factor, etc. This process continues until the parameter set stabilizes. The second issue concerns statistics. With the MC data available on the grid, we were not able to generate the statistics necessary to use the raw  $C_{True}/C_{Rec}$  ratio. The ratio was not stable, and when applied to the data, obscured the signal. Attempting to fit the ratio to generate the corrections also proved problematic. However, as HIJING does not include final-state interactions, the same-event and mixed-event pairs are very similar (with the exception of things like energy and momentum conservation, etc). Therefore, one may build the numerator distribution using mixed-event pairs. This corresponds, more or less, to simply running a the weight generator through the detector framework.

A second approach is to use information gained from plots like those in Figure 15, which can be considered response matrices. The response matrix describes quantitatively how each  $k_{Rec}^*$  bin receives contributions from multiple  $k_{True}^*$  bins, and can be used to account for the effects of finite momentum resolution. With this approach, the resolution correction is applied on-the-fly during the fitting process by propagating the theoretical (fit) correlation function through the response matrix, according to:

$$C_{fit}(k_{Rec}^*) = \frac{\sum_{k_{True}^*} M_{k_{Rec}^*, k_{True}^*} C_{fit}(k_{True}^*)}{\sum_{k_{True}^*} M_{k_{Rec}^*, k_{True}^*}} \quad (14)$$

where  $M_{k_{Rec}^*, k_{True}^*}$  is the response matrix (Figure 15),  $C_{fit}(k_{True}^*)$  is the fit binned in  $k_{True}^*$ , and the denominator normalizes the result.

433 Equation 14 describes that, for a given  $k_{Rec}^*$  bin, the observed value of  $C(k_{Rec}^*)$  is a weighted average of  
 434 all  $C(k_{True}^*)$  values, where the weights are the normalized number of counts in the  $[k_{Rec}^*, k_{True}^*]$  bin. As  
 435 seen in Figure 15, overwhelmingly the main contributions comes from the  $k_{Rec}^* = k_{True}^*$  bins. Although  
 436 the correction is small, it is non-negligible for the low- $k^*$  region of the correlation function.

437 Here, the momentum resolution correction is applied to the fit, not the data. In other words, during  
 438 fitting, the theoretical correlation function is smeared just as real data would be, instead of unsmearing  
 439 the data. This may not be ideal for the theorist attempting to compare a model to experimental data, but  
 440 it leaves the experimental data unadulterated. The current analyses use this second approach to applying  
 441 momentum resolution corrections because of two major advantages. First, the MC data must be analyzed  
 442 only once, and no assumptions about the fit are needed. Secondly, the momentum resolution correction  
 443 is applied on-the-fly by the fitter, delegating the iterative process to a computer instead of the user.

#### 444 5.4 Residual Correlations

445 The purpose of this analysis is study the interaction and scale of the emitting source of the pairs. In  
 446 order to obtain correct results, it is important for our particle collections to consist of primary particles.  
 447 In practice, this is difficult to achieve for our  $\Lambda$  and  $\bar{\Lambda}$  collections. Many of our  $\Lambda$  particles are not  
 448 primary, but originate as decay products from other hyperons, including  $\Sigma^0$ ,  $\Xi^0$ ,  $\Xi^-$  and  $\Sigma^{*(+,-,0)}(1385)$ .  
 449 Additionally, many of our K particles are not primary, but decay from  $K^{*(+,-,0)}(892)$  parents. In these  
 450 decays, the  $\Lambda$  carries away a momentum very similar to that of its parent. As a result, the correlation  
 451 function between a secondary  $\Lambda$  and, for instance, a  $K^+$  will be sensitive to, and dependent upon, the  
 452 interaction between the parent of the  $\Lambda$  and the  $K^+$ . In effect, the correlation between the parent of  
 453 the  $\Lambda$  and the  $K^+$  (ex.  $\Sigma^0 K^+$ ) will be visible, although smeared out, in the  $\Lambda K^+$  data. We call this a  
 454 residual correlation resulting from feed-down. Residual correlations are important in an analysis when  
 455 three criteria are met [6]: i) the parent correlation signal is large, ii) a large fraction of pairs in the sample  
 456 originate from the particular parent system, and iii) the decay momenta are comparable to the expected  
 457 correlation width in  $k^*$ .

458 As it is difficult for us to eliminate these residual correlations in our analyses, we must attempt to account  
 459 for them in our fitter. To achieve this, we will simultaneously fit the data for both the primary correlation  
 460 function and the residual correlations. For example, in the simple case of a  $\Lambda K^+$  analysis with residuals  
 461 arising solely from  $\Sigma^0 K^+$  feed-down:

$$C_{measured}(k_{\Lambda K^+}^*) = 1 + \lambda_{\Lambda K^+}[C_{\Lambda K^+}(k_{\Lambda K^+}^*) - 1] + \lambda_{\Sigma^0 K^+}[C_{\Sigma^0 K^+}(k_{\Lambda K^+}^*) - 1]$$

$$C_{\Sigma^0 K^+}(k_{\Lambda K^+}^*) \equiv \frac{\sum_{k_{\Sigma^0 K^+}^*} C_{\Sigma^0 K^+}(k_{\Sigma^0 K^+}^*) T(k_{\Sigma^0 K^+}^*, k_{\Lambda K^+}^*)}{\sum_{k_{\Sigma^0 K^+}^*} T(k_{\Sigma^0 K^+}^*, k_{\Lambda K^+}^*)} \quad (15)$$

462  $C_{\Sigma^0 K^+}(k_{\Sigma^0 K^+}^*)$  is the  $\Sigma^0 K^+$  correlation function from, for instance, Equation 5, and  $T$  is the transform  
 463 matrix generated with THERMINATOR. The transform matrix is formed for a given parent pair, AB,  
 464 by taking all  $\Lambda K$  pairs originating from AB, calculating the relative momentum of the parents ( $k_{AB}^*$ )  
 465 and daughters ( $k_{\Lambda K}^*$ ), and filling a two-dimensional histogram with the values. The transform matrix  
 466 is essentially an unnormalized probability distribution mapping the  $k^*$  of the parent pair to that of the  
 467 daughter pair when one or both parents decay. An example of such transform matrices can be found in  
 468 Figures 17 and 18.

469 The above equation can be easily extended to include feed-down from more sources:

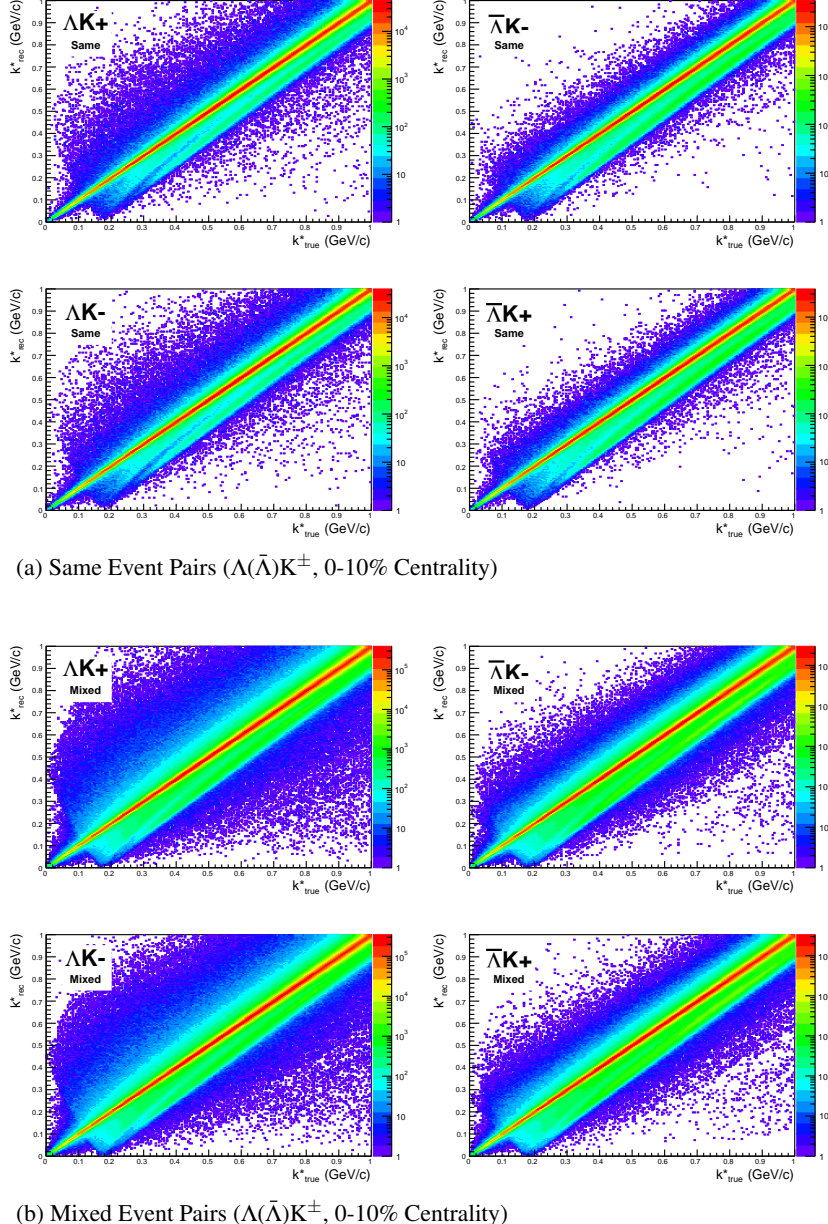
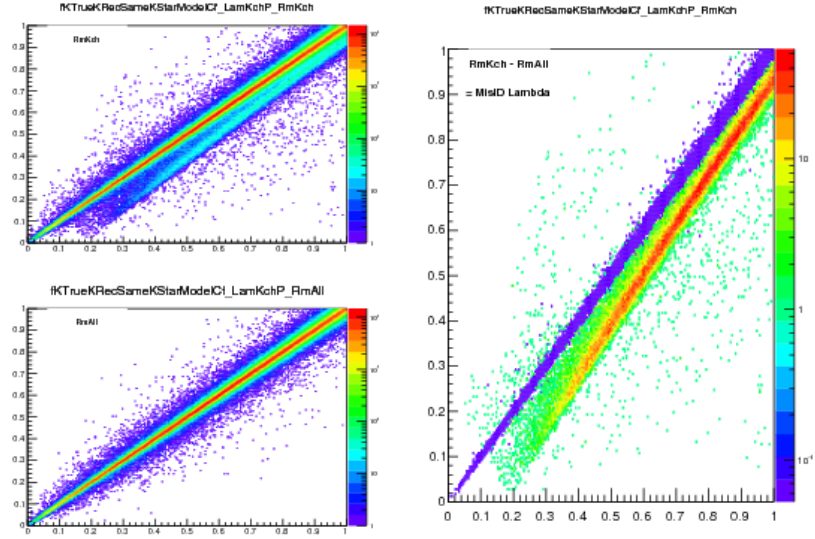


**Fig. 15:** Sample  $k_{True}^*$  vs.  $k_{Rec}^*$  plot for  $\Lambda(\bar{\Lambda})K^\pm$  0-10% analyses. The structure which appears around  $k_{Rec}^* = k_{True}^* - 0.15$  is mainly caused by  $K_S^0$  contamination in our  $\Lambda(\bar{\Lambda})$  sample. The remaining structure not distributed about  $k_{Rec}^* = k_{True}^*$  is due to  $\pi$  and  $e$  contamination in our  $K^\pm$  sample. These contaminations are more clearly visible in Figure 16

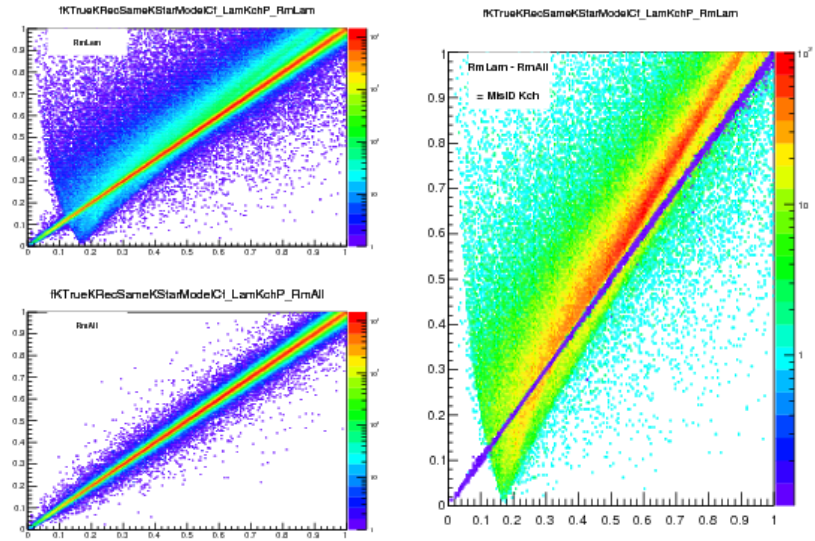
$$C_{measured}(k_{\Lambda K}^*) = 1 + \lambda_{\Lambda K} [C_{\Lambda K}(k_{\Lambda K}^*) - 1] + \lambda_{\Sigma^0 K} [C_{\Sigma^0 K}(k_{\Lambda K}^*) - 1] + \dots \\ + \lambda_{P_1 P_2} [C_{P_1 P_2}(k_{\Lambda K}^*) - 1] + \lambda_{other} [C_{other}(k_{\Lambda K}^*) - 1]$$

$$C_{P_1 P_2}(k_{\Lambda K}^*) \equiv \frac{\sum_{k_{P_1 P_2}^*} C_{P_1 P_2}(k_{P_1 P_2}^*) T(k_{P_1 P_2}^*, k_{\Lambda K}^*)}{\sum_{k_{P_1 P_2}^*} T(k_{P_1 P_2}^*, k_{\Lambda K}^*)} \quad (16)$$

470 Or, more compactly:



(a) (Top Left) All misidentified  $K^+$  excluded. (Bottom Left) All misidentified  $\Lambda$  and  $K^+$  excluded. (Right) The difference of (Top Left) - (Bottom Left), which reveals the contamination in our  $\Lambda$  collection. The structure which appears around  $k_{Rec}^* = k_{True}^* - 0.15$  is mainly caused by  $K_S^0$  contamination in our  $\Lambda(\bar{\Lambda})$  sample.



(b) (Top Left) All misidentified  $\Lambda$  excluded. (Bottom Left) All misidentified  $\Lambda$  and  $K^+$  excluded. (Right) The difference of (Top Left) - (Bottom Left), which reveals the contamination in our  $K^+$  collection. The structure not distributed about  $k_{Rec}^* = k_{True}^*$  is due to  $\pi$  and  $e^-$  contamination in our  $K^\pm$  sample.

**Fig. 16:** Note: This is an old figure and is for a small sample of the data. A new version will be generated shortly.  
 $y\text{-axis} = k_{Rec}^*$ ,  $x\text{-axis} = k_{True}^*$ .

(Left)  $k_{Rec}^*$  vs.  $k_{True}^*$  plots for a small sample of the  $\Lambda K^+$  0-10% central analysis, MC truth was used to eliminate misidentified particles in the  $K^+$ (a) and  $\Lambda$ (b) collections. (Right) The difference of the top left and bottom left plots. Contaminations in our particle collections are clearly visible. Figure (a) demonstrates a  $K_S^0$  contamination in our  $\Lambda$  collection; Figure (b) demonstrates a  $\pi$  and  $e^-$  contamination in our  $K^\pm$  collection.

$$C_{measured}(k_{\Lambda K}^*) = 1 + \sum_i \lambda_i [C_i(k_{\Lambda K}^*) - 1] \quad (17)$$

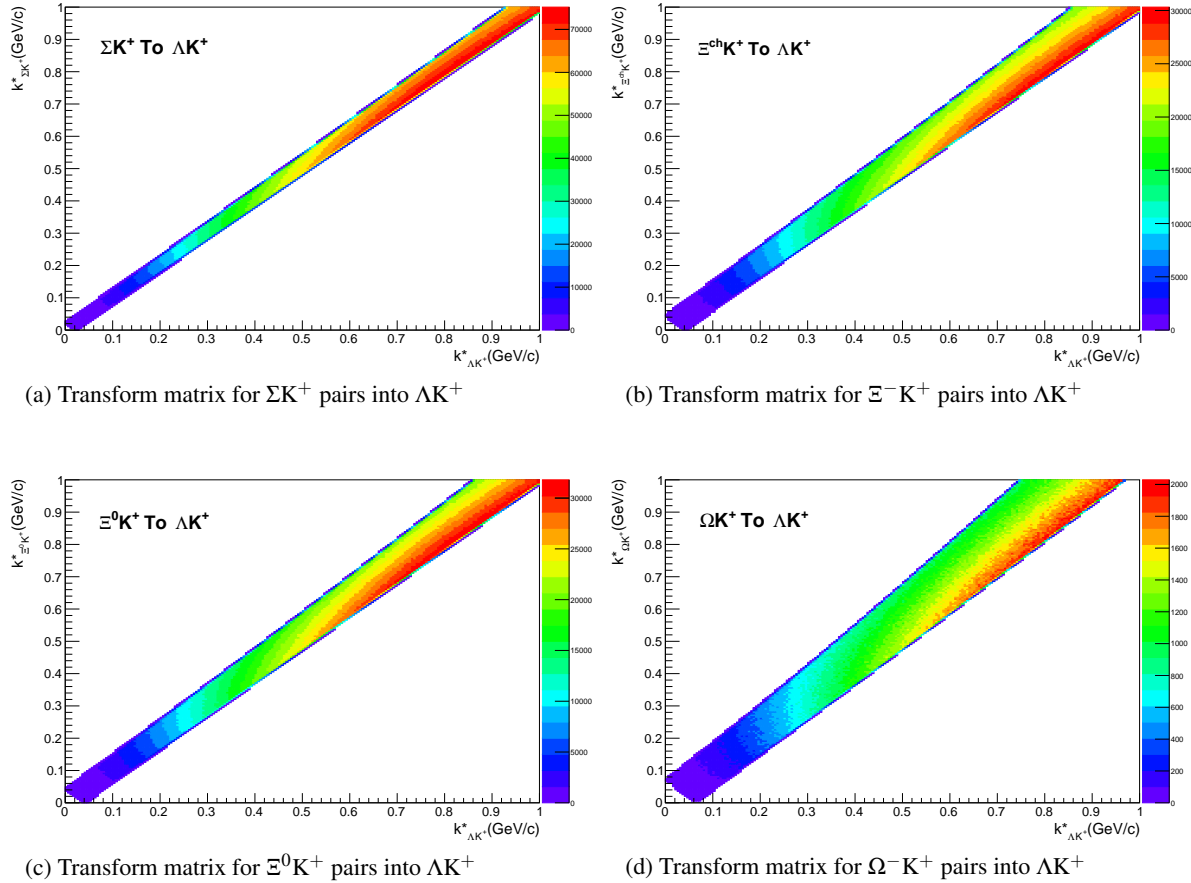


**Fig. 17:** Transform Matrices generated with THERMINATOR for  $\Lambda K^+$  Analysis

471 So, in practice, we model the correlation function of the parents, and run the correlation function through  
 472 the appropriate transform matrix to determine the contribution to the daughter correlation function. A  
 473 few questions still remain. First, what  $\lambda$  values should be used in the above equation? One option  
 474 would be to leave all of these  $\lambda$ -parameters free during the fit process. However, this would introduce  
 475 a huge number of new parameters into the fitter, and would make the fit results less trustworthy. The  $\lambda$   
 476 parameters roughly dictate the strength of the parent contribution to the daughter pair. Additionally, as  
 477 found in [7], the reconstruction efficiency for primary  $\Lambda$  particles is nearly equal to that of  $\Lambda$  particles  
 478 originating from  $\Sigma$ ,  $\Sigma^*$ ,  $\Xi^0$ ,  $\Xi^-$ , and  $\Omega$  hyperons. Therefore, the  $\lambda$  parameter for parent system AB can  
 479 be estimated using THERMINATOR as the total number of  $\Lambda K$  pairs originating from AB ( $N_{AB}$ ) divided  
 480 by the total number of  $\Lambda K$  pairs ( $N_{Total}$ ):

$$\lambda_{AB} = \frac{N_{AB}}{N_{Total}} \quad (18)$$

481 Now, the remaining question is how do we model the parent correlation functions? In an ideal world, we  
 482 would simply look up the parent interaction in some table, and input this into our Lednicky equation (for  
 483 the case of one or more charge neutral particle in the pair), or run it through the CoulombFitter machinery  
 484 described in Sec. 5.2. Unfortunately, the world in which we live is not perfect, such a table does not  
 485 exist, and little is known about the interaction between the residual pairs in this study. One solution  
 486 would be to introduce a set of scattering parameters and radii for each residual system. However, as will  
 487 be the case of the  $\lambda$ -parameters above, this would introduce a large number of additional fit parameters,  
 488 and would make our fitter too unconstrained and would yield untrustworthy results. The second option,

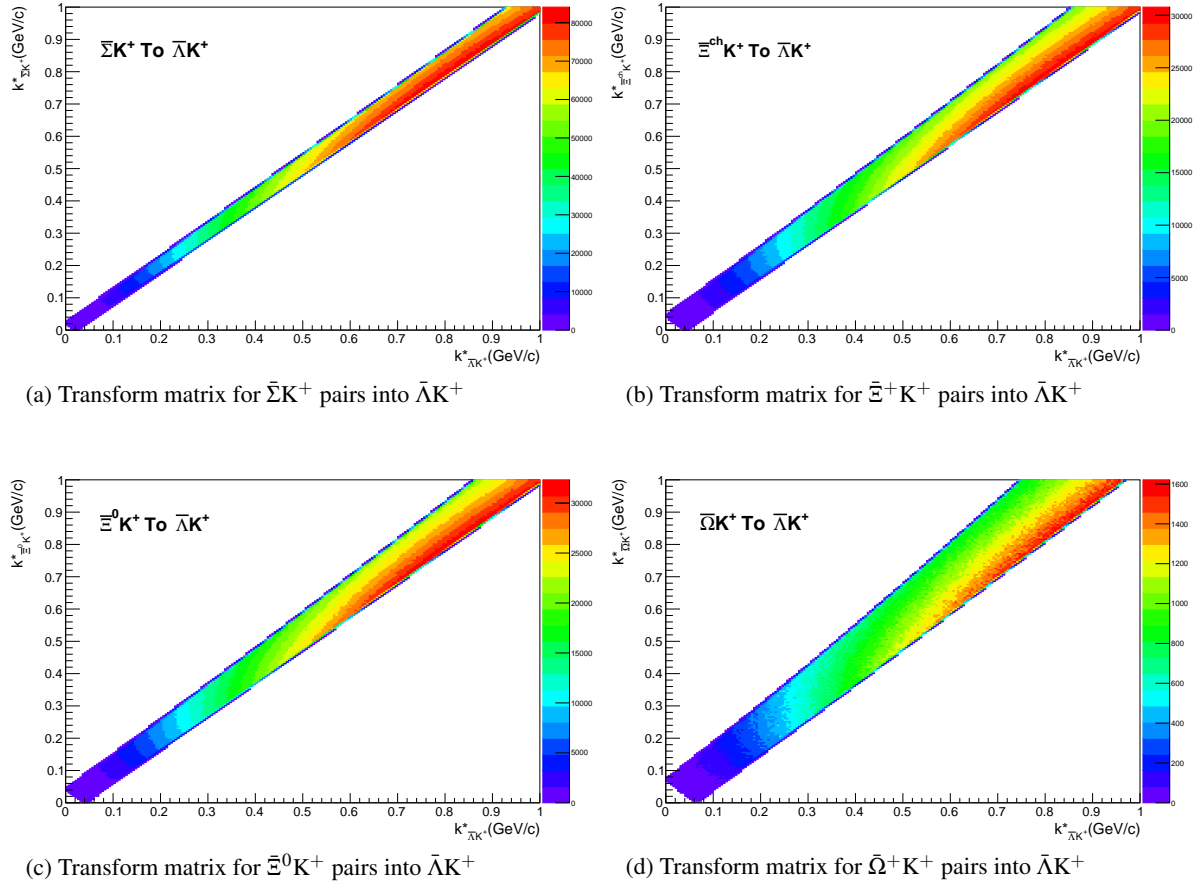


**Fig. 18:** Transform Matrices generated with THERMINATOR for  $\bar{\Lambda}K^+$  Analysis

which is adopted in this analysis, is to assume all residual pairs have the same source size as the daughter pair, and all Coulomb-neutral residual pairs also share the same scattering parameters as the daughter pair (the case of charged pairs will be described below).

Concerning the radii of the residual parent pairs, it was suggested that these should be set to smaller values. In the interest of minimizing the number of parameters in the fitter, we tested this by introducing an  $m_T$ -scaling of the parent radii. The motivation for this scaling comes from the approximate  $m_T$ -scaling of the radii observed in 49. To achieve this scaling, we assume the radii follow an inverse-square distribution:  $R_{AB} = \alpha m_T^{1/2}$ . Then, it follows that we should scale the parent radii as:

$$R_{AB} = R_{\Lambda K} \left( \frac{m_{T,AB}}{m_{T,\Lambda K}} \right)^{1/2} \quad (19)$$

The values for  $m_T$  for each pair system was taken from THERMINATOR. As the fitter dances around parameter space and selects new radii for the  $\Lambda K$  pairs, the radii of the residuals is scaled by the above factor. In the end, this scaling factor made no significant difference in our fit results, so this complication is excluded from our final results. Note that this is not surprising, as the most extreme scaling factor was, in the case of using 10 residual systems, between  $\Lambda K^+$  with  $m_{T,\Lambda K^+} \approx 1.4 \text{ GeV}/c^2$  and  $\Xi^- K^{*0}$  with  $m_{T,\Xi^- K^{*0}} \approx 1.8 \text{ GeV}/c^2$ , resulting in a scale factor of  $\approx 0.9$ .

Now, as hinted above, accounting for charged residuals adds a complication in that they necessitate the inclusion of the CoulombFitter into the process. The complication of combining the two fitters is not

troubling, but it increases the fitting time drastically (the parallelization of the CoulombFitter across a large number of GPU cores, to drastically decrease run-time, is currently underway). We have two solutions to bypass such a large increase in run time. First, we can use our experimental  $\Xi^{\text{ch}}K^{\text{ch}}$  data to represent all charged parent pair system. In this case, there is no need to make any assumption about scattering parameters or source sizes, as we already have the experimental data. The downside is that, especially in the 30-50% centrality bin, the error bars on the data are large. Alternatively, we can assume the strong interaction is negligible in the charged residual, and generate the parent correlation function given radius and  $\lambda$  parameters. We find in our  $\Xi^{\text{ch}}K^{\text{ch}}$  study that a Coulomb-only description of the system describes, reasonably well, the broad features of the correlation. The strong interaction is necessary for the fine details. However, as these correlations are run through a transform matrix, which largely flattens out and fine details, a Coulomb-only description should be sufficient. In practice, this Coulomb-only scenario is achieved by first building a large number of Coulomb-only correlations for various radii and  $\lambda$  parameter values, and interpolating from this grid during the fitting process. We find consistent results between using the  $\Xi K$  data and the Coulomb-only interpolation method. When the number of residual pairs used is increased to 10, so that pairs such as  $\Sigma^{*+}K^-$  enter the picture, the Coulomb-only interpolation method is used. In other words, the  $\Xi K$  experimental data is only used to model the  $\Xi K$  residual contribution, all other charged pairs are treated with the Coulomb-only interpolation method.

Two examples of how very different transform matrices can alter a correlation function are shown in Figures 19 and 20 below. These figures were taken using parameter values obtained from fits to the data. In the top left corner of the figures, the input correlation function (closed symbols) is shown together with the output, transformed, correlation function (open symbols). In the bottom left, the transformed correlation is shown by itself. This is especially helpful when the  $\lambda$  parameter is very small, in which case the contribution in the top left can look flat, but the zoomed in view in the bottom left shows the structure. The right two plots in each figure show the transform matrix without (top right) and with (bottom right) a log-scale on the z-axis. Note, more examples of these transforms can be found in Sec. 9.

## 6 Systematic Errors

In order to understand my systematic uncertainties, the analysis code was run many times using slightly different values for a number of important cuts, and the results were compared.

In order to quantify the systematic errors on the data, all correlation functions built using all varied cut values were bin-by-bin averaged, and the resulting variance of each bin was taken as the systematic error. The cuts which were utilized in this study are presented in Sections 6.1.1 ( $\Lambda K_S^0$ ) and 6.2.1 ( $\Lambda K^\pm$ ).

Similarly, the fit parameters extracted from all of these correlation functions were averaged, and the resulting variances were taken as the systematic errors for the fit parameters. As with the systematic errors on the data, this was performed for all varied cut values. Additionally, a systematic analysis was done on our fit method (which, for now, just includes our choice of fit range). These two sources of uncertainty were combined in quadrature to obtain the final systematic uncertainties on the extracted fit parameters.

### 6.1 Systematic Errors: $\Lambda K_S^0$

#### 6.1.1 Particle and Pair Cuts

The cuts included in the systematic study, as well as the values used in the variations, are listed below. Note, the central value corresponds to that used in the analysis.

- 547 1. DCA  $\Lambda(\bar{\Lambda})$ : {4, 5, 6 mm}

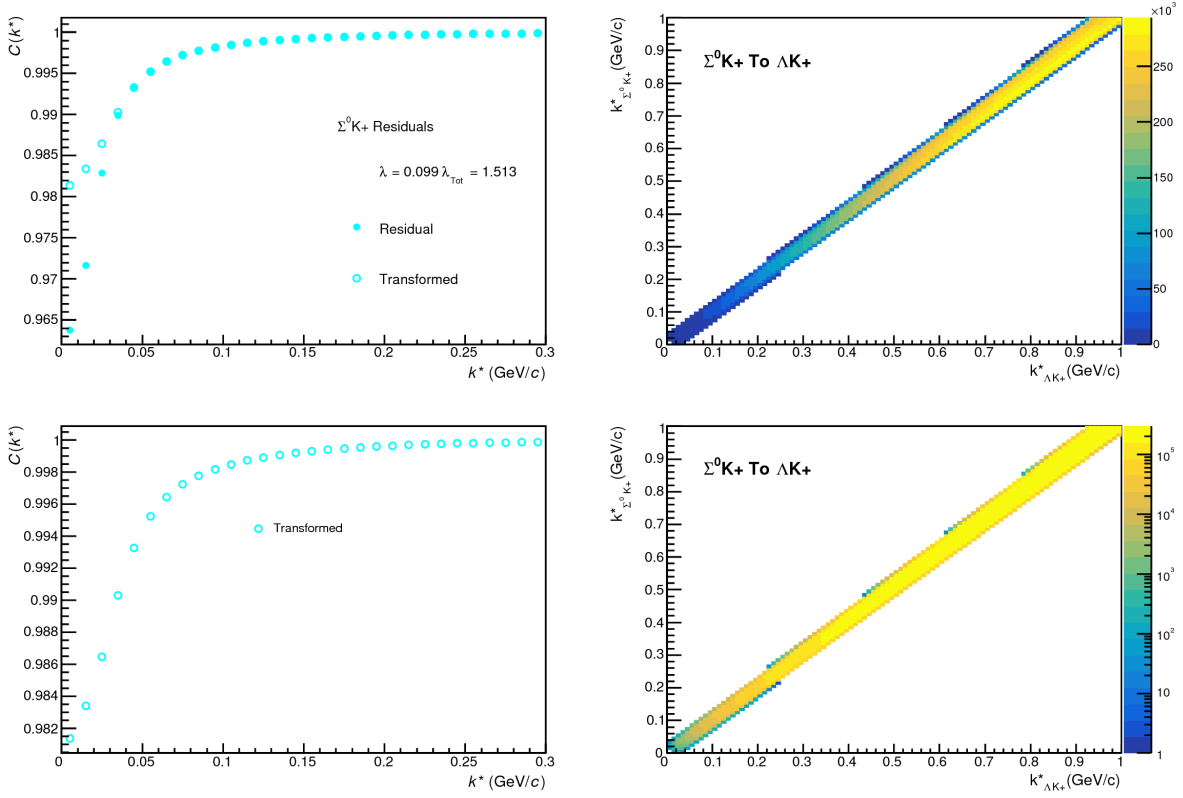


**Fig. 19:**  $\Sigma^0 K^+$  Transform. These figures were taken using parameter values obtained from fits to the data. In the top left corner of the figures, the input correlation function (closed symbols) is shown together with the output, transformed, correlation function (open symbols). In the bottom left, the transformed correlation is shown by itself. The right two plots in each figure show the transform matrix without (top right) and with (bottom right) a log-scale on the z-axis.

- 548      2. DCA  $K_S^0$ : {2, 3, 4 mm}
- 549      3. DCA  $\Lambda(\bar{\Lambda})$  Daughters: {3, 4, 5 mm}
- 550      4. DCA  $K_S^0$  Daughters: {2, 3, 4 mm}
- 551      5.  $\Lambda(\bar{\Lambda})$  Cosine of Pointing Angle: {0.9992, 0.9993, 0.9994}
- 552      6.  $K_S^0$  Cosine of Pointing Angle: {0.9992, 0.9993, 0.9994}
- 553      7. DCA to Primary Vertex of  $p(\bar{p})$  Daughter of  $\Lambda(\bar{\Lambda})$ : {0.5, 1, 2 mm}
- 554      8. DCA to Primary Vertex of  $\pi^-(\pi^+)$  Daughter of  $\Lambda(\bar{\Lambda})$ : {2, 3, 4 mm}
- 555      9. DCA to Primary Vertex of  $\pi^+$  Daughter of  $K_S^0$ : {2, 3, 4 mm}
- 556      10. DCA to Primary Vertex of  $\pi^-$  Daughter of  $K_S^0$ : {2, 3, 4 mm}
- 557      11. Average Separation of Like-Charge Daughters: {5, 6, 7 cm}

### 558      6.1.2 Non-Flat Background

559      We fit our non-flat background with a linear function. To study the contribution of this choice to our sys-  
 560      tematic errors, we also fit with a quadratic and Gaussian form. The resulting uncertainties are combined  
 561      with the uncertainties arising from our particle cuts.



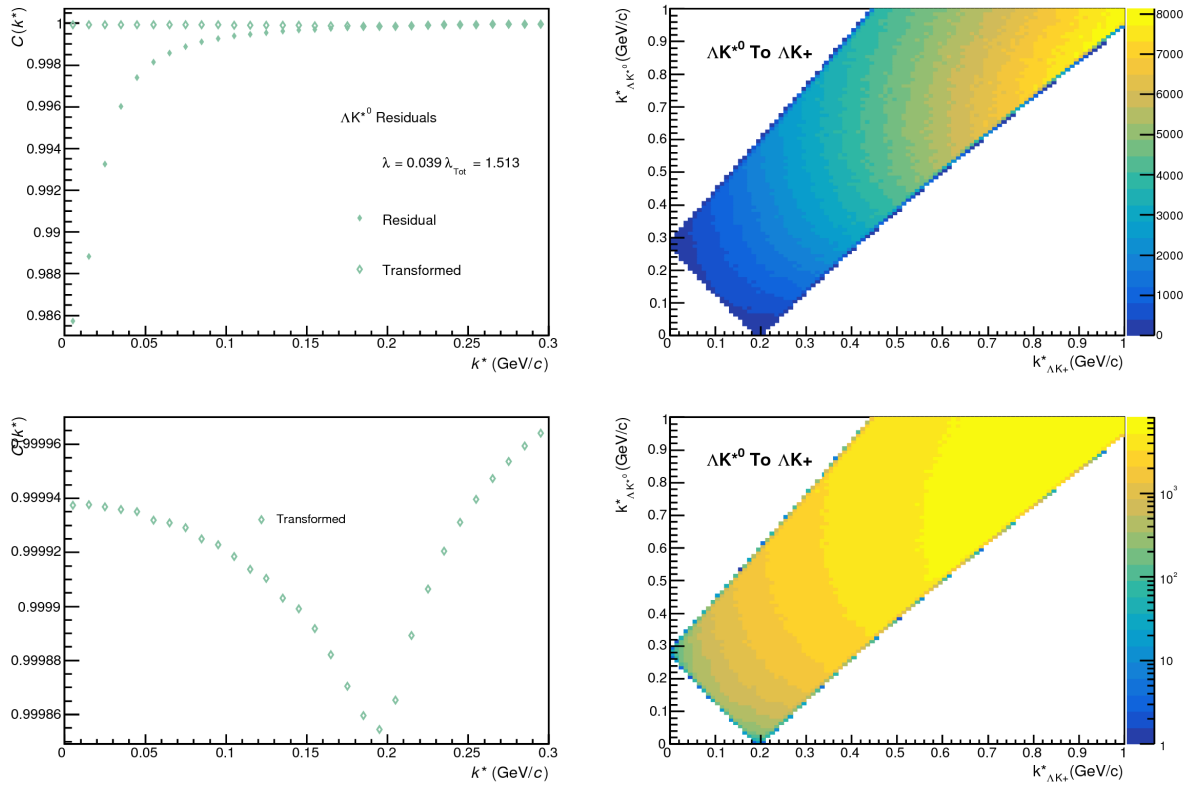


**Fig. 20:**  $\Sigma^0 K^+$  Transform. These figures were taken using parameter values obtained from fits to the data. In the top left corner of the figures, the input correlation function (closed symbols) is shown together with the output, transformed, correlation function (open symbols). In the bottom left, the transformed correlation is shown by itself. The right two plots in each figure show the transform matrix without (top right) and with (bottom right) a log-scale on the z-axis.

### 562 6.1.3 Fit Range

563 Our choice of  $k^*$  fit range was varied by  $\pm 25\%$ . The resulting uncertainties in the extracted parameter  
564 sets were combined with our uncertainties arising from our particle and pair cuts.

## 565 6.2 Systematic Errors: $\Lambda K^\pm$

### 566 6.2.1 Particle and Pair Cuts

567 The cuts included in the systematic study, as well as the values used in the variations, are listed below.  
568 Note, the central value corresponds to that used in the analysis.

- 569 1. DCA  $\Lambda(\bar{\Lambda})$ : {4, 5, 6 mm}
- 570 2. DCA  $\Lambda(\bar{\Lambda})$  Daughters: {3, 4, 5 mm}
- 571 3.  $\Lambda(\bar{\Lambda})$  Cosine of Pointing Angle: {0.9992, 0.9993, 0.9994}
- 572 4. DCA to Primary Vertex of  $p(\bar{p})$  Daughter of  $\Lambda(\bar{\Lambda})$ : {0.5, 1, 2 mm}
- 573 5. DCA to Primary Vertex of  $\pi^-(\pi^+)$  Daughter of  $\Lambda(\bar{\Lambda})$ : {2, 3, 4 mm}
- 574 6. Average Separation of  $\Lambda(\bar{\Lambda})$  Daughter with Same Charge as  $K^\pm$ : {7, 8, 9 cm}
- 575 7. Max. DCA to Primary Vertex in Transverse Plane of  $K^\pm$ : {1.92, 2.4, 2.88}

576     8. Max. DCA to Primary Vertex in Longitudinal Direction of  $K^\pm$ : {2.4, 3.0, 3.6}

577     **6.2.2 Non-Flat Background**

578     We fit our non-flat background with a linear function. To study the contribution of this choice to our sys-  
 579     tematic errors, we also fit with a quadratic and Gaussian form. The resulting uncertainties are combined  
 580     with the uncertainties arising from our particle cuts.

581     **6.2.3 Fit Range**

582     Our choice of  $k^*$  fit range was varied by  $\pm 25\%$ . The resulting uncertainties in the extracted parameter  
 583     sets were combined with our uncertainties arising from our particle and pair cuts.

584     **6.3 Systematic Errors:  $\Xi K^\pm$**

585     **6.3.1 Particle and Pair Cuts**

586     The cuts included in the systematic study, as well as the values used in the variations, are listed below.  
 587     Note, the central value corresponds to that used in the analysis.

588       1. Max. DCA  $\Xi(\bar{\Xi})$ : {x, y, z mm}

589       2. Max. DCA  $\Xi(\bar{\Xi})$  Daughters: {x, y, z mm}

590       3. Min.  $\Xi(\bar{\Xi})$  Cosine of Pointing Angle to Primary Vertex: {0.9991, 0.9992, 0.9993}

591       4. Min.  $\Lambda(\bar{\Lambda})$  Cosine of Pointing Angle to  $\Xi(\bar{\Xi})$  Decay Vertex: {0.9992, 0.9993, 0.9994}

592       5. Min. DCA Bachelor  $\pi$ : {0.2, 0.3, 0.4 mm}

593       6. Min. DCA  $\Lambda(\bar{\Lambda})$ : {0.5, 1, 2 mm}

594       7. Max. DCA  $\Lambda(\bar{\Lambda})$  Daughters: {3, 4, 5 mm}

595       8. Min.  $\Lambda(\bar{\Lambda})$  Cosine of Pointing Angle To Primary Vertex: {0.9992, 0.9993, 0.9994}

596       9. Min. DCA to Primary Vertex of  $p(\bar{p})$  Daughter of  $\Lambda(\bar{\Lambda})$ : {0.5, 1, 2 mm}

597       10. Min. DCA to Primary Vertex of  $\pi^-(\pi^+)$  Daughter of  $\Lambda(\bar{\Lambda})$ : {2, 3, 4 mm}

598       11. Min. Average Separation of  $\Lambda(\bar{\Lambda})$  Daughter and  $K^\pm$  with like charge: {7, 8, 9 cm}

599       12. Min. Average Separation of Bachelor  $\pi$  and  $K^\pm$  with like charge: {x, y, z cm}

600       13. Max. DCA to Primary Vertex in Transverse Plane of  $K^\pm$ : {1.92, 2.4, 2.88}

601       14. Max. DCA to Primary Vertex in Longitudinal Direction of  $K^\pm$ : {2.4, 3.0, 3.6}

602     **7 Results and Discussion**

603     **7.1 Results:  $\Lambda K_S^0$  and  $\Lambda K^\pm$**

604     I first collect all of the summary results, and will show the actual fits to the data in Sections 7.1.1, 7.1.2,  
 605     and 7.1.3. In the first of the summary plots, we show the extracted scattering parameters in the form of a  
 606      $\text{Im}[f_0]$  vs  $\text{Re}[f_0]$  plot, which includes the  $d_0$  values to the right side. The next three summary plots show  
 607     the  $\lambda$  vs. Radius parameters. The first group of plots shows: 1) results without any residual correlations  
 608     included in the fit (marked as "QM 2017"), 2) results with 10 residual pairs included, and 3) results  
 609     with 3 residual pairs included. The second group of plots also includes the case where we fixed the  $d_0$   
 610     parameter to zero.



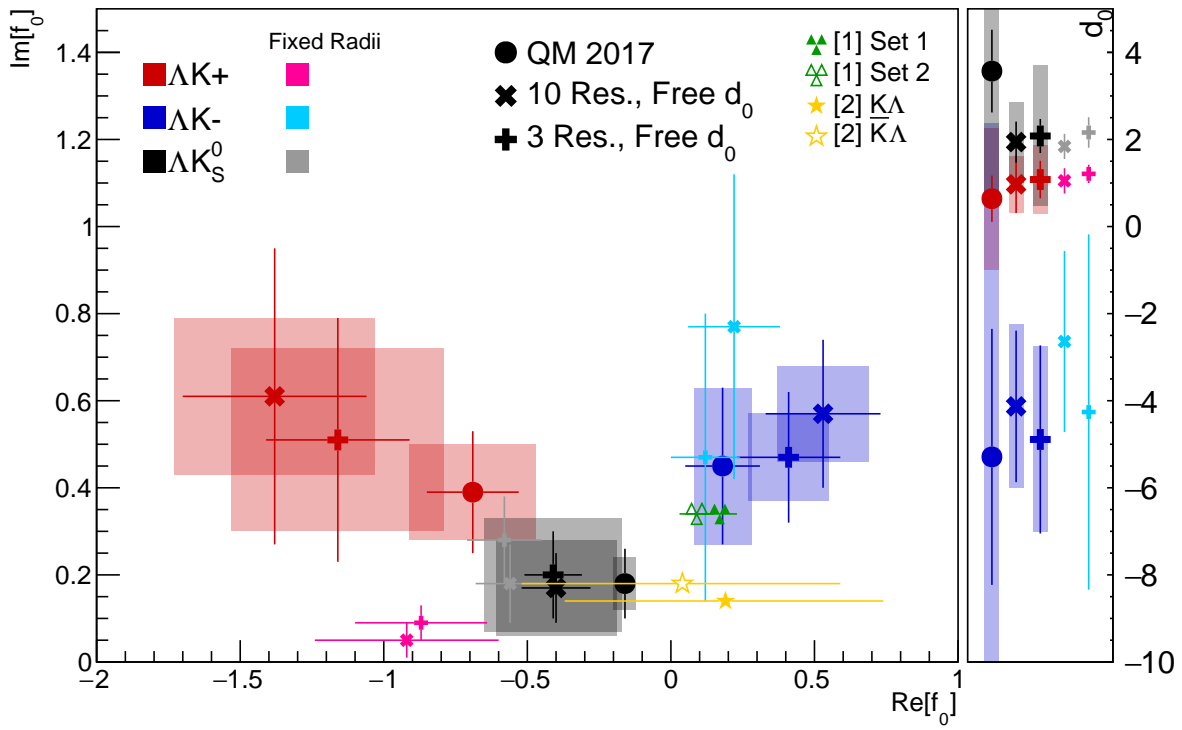


**Fig. 21:** Extracted scattering parameter results,  $\text{Im}[f_0]$  vs.  $\text{Re}[f_0]$ , together with  $d_0$  to the right, for all of our  $\Lambda K$  systems. The plot shows results including no residuals (circles), 10 residual pairs (X), and 3 residual pairs (+). The lighter color markers (pink, sky blue, gray) show the extracted parameters when we fix the radii to roughly align with the  $m_T$ -scaling plot, Fig. 35. The green [8] and yellow [9] points show theoretical predictions made using chiral perturbation theory. Note,  $\Lambda K^+$  on the plot is shorthand for  $\Lambda K^+$  and  $\bar{\Lambda} K^-$ , and similar for the others.

### 611 7.1.1 Results: $\Lambda K_S^0$ and $\Lambda K^\pm$ : No Residual Correlations Included in Fit

612 Figures 29, 31, and 33 (Section 7) show experimental data with fits for all studied centralities for  $\Lambda K_S^0$   
 613 with  $\bar{\Lambda} K_S^0$ ,  $\Lambda K^+$  with  $\bar{\Lambda} K^-$ , and  $\Lambda K^-$  with  $\bar{\Lambda} K^+$ , respectively. The parameter sets extracted from the fits  
 614 can be found in Tables 1 and 2. All correlation functions were normalized in the range  $0.32 < k^* < 0.40$   
 615 GeV/c, and fit in the range  $0.0 < k^* < 0.30$  GeV/c. For the  $\Lambda K^-$  and  $\bar{\Lambda} K^+$  analyses, the region  $0.19 < k^* < 0.23$  GeV/c was excluded from the fit to exclude the bump caused by the  $\Omega^-$  resonance. The  
 616 non-flat background was fit with a linear form from  $0.6 < k^* < 0.9$  GeV/c. The theoretical fit function  
 617 was then multiplied by this background during the fitting process.

619 In the figures (29, 31, and 33), the black solid line represents the “raw” fit, i.e. not corrected for momen-  
 620 tum resolution effects nor non-flat background. The green line shows the fit to the non-flat background.  
 621 The purple points show the fit after momentum resolution and non-flat background corrections have been  
 622 applied. The initial values of the parameters is listed, as well as the final fit values with uncertainties.

623 For the  $\Lambda K_S^0$  fits,  $R$  was restricted to  $[2.0, 10.0 \text{ fm}]$  and  $\lambda$  was restricted to  $[0.1, 0.8]$ . This gave the lowest  
 624  $\chi^2$  value, but loosening this restriction changes the fit parameters slightly. Notice, the 10-30% radius is  
 625 at its limit, as is  $\lambda$  from the 30-50%  $\Lambda K_S^0$  analysis. This accounts for the 0.000 systematic uncertainty of  
 626 the 10-30%  $R$  value currently quoted in Table 1. An estimate for this uncertainty should be included in  
 627 the next version of this note. In the future, we may need to throw out the 30-50% data from the fit, but  
 628 this is not ideal.

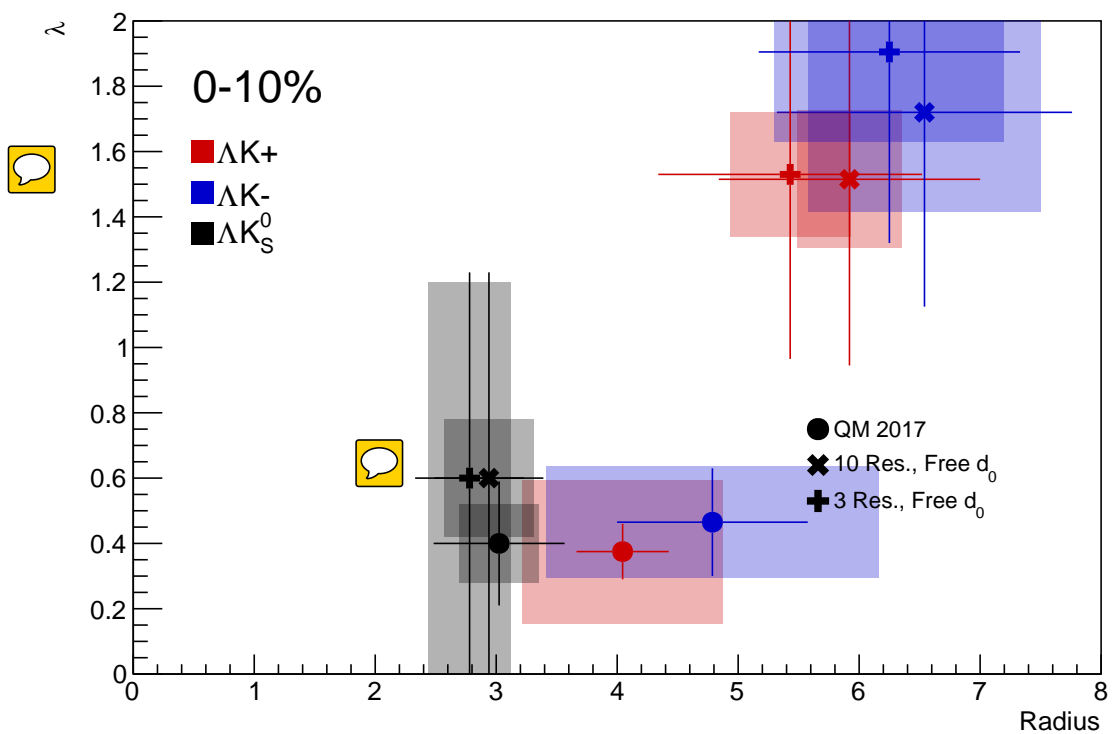


**Fig. 22:** Extracted  $\lambda$  vs Radius results, for the 0-10% centrality bin, for all of our  $\Lambda K$  systems. The plot shows results including no residuals (circles), 10 residual pairs (X), and 3 residual pairs (+). Note,  $\Lambda K^+$  on the plot is shorthand for  $\Lambda K^+$  and  $\bar{\Lambda}K^-$ , and similar for the others.

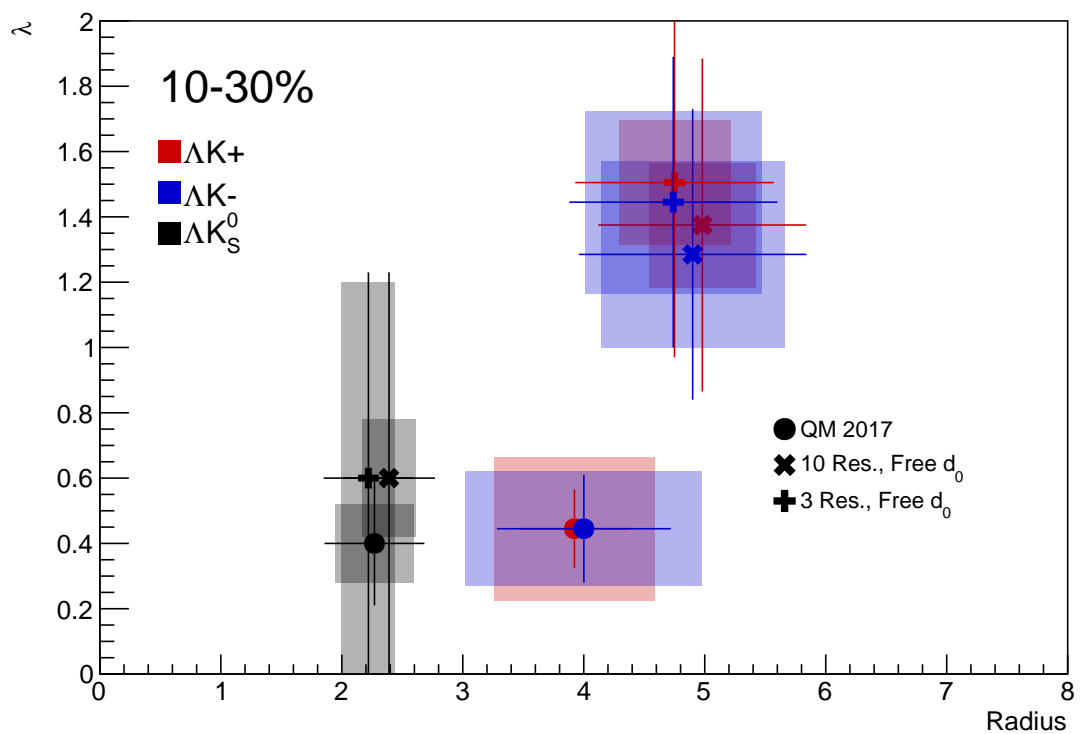


**Fig. 23:** Extracted  $\lambda$  vs Radius results, for the 10-30% centrality bin, for all of our  $\Lambda K$  systems. The plot shows results including no residuals (circles), 10 residual pairs (X), and 3 residual pairs (+). Note,  $\Lambda K^+$  on the plot is shorthand for  $\Lambda K^+$  and  $\bar{\Lambda} K^-$ , and similar for the others.

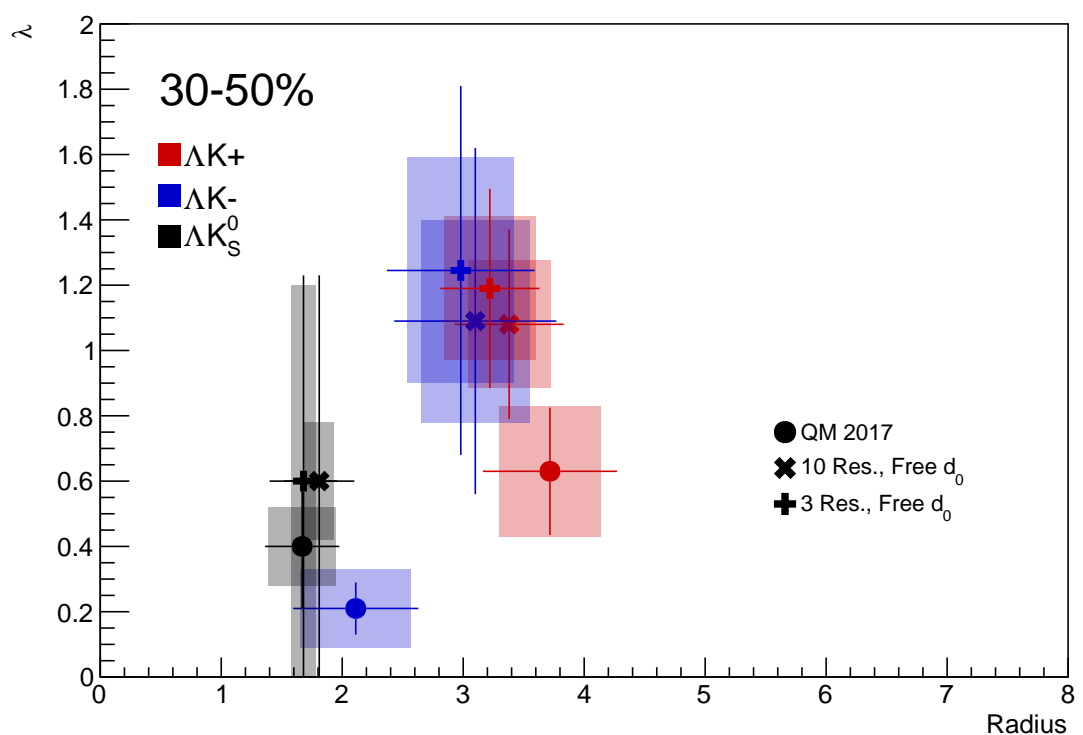


**Fig. 24:** Extracted  $\lambda$  vs Radius results, for the 30-50% centrality bin, for all of our  $\Lambda K$  systems. The plot shows results including no residuals (circles), 10 residual pairs (X), and 3 residual pairs (+). Note,  $\Lambda K^+$  on the plot is shorthand for  $\Lambda K^+$  and  $\bar{\Lambda} K^-$ , and similar for the others.

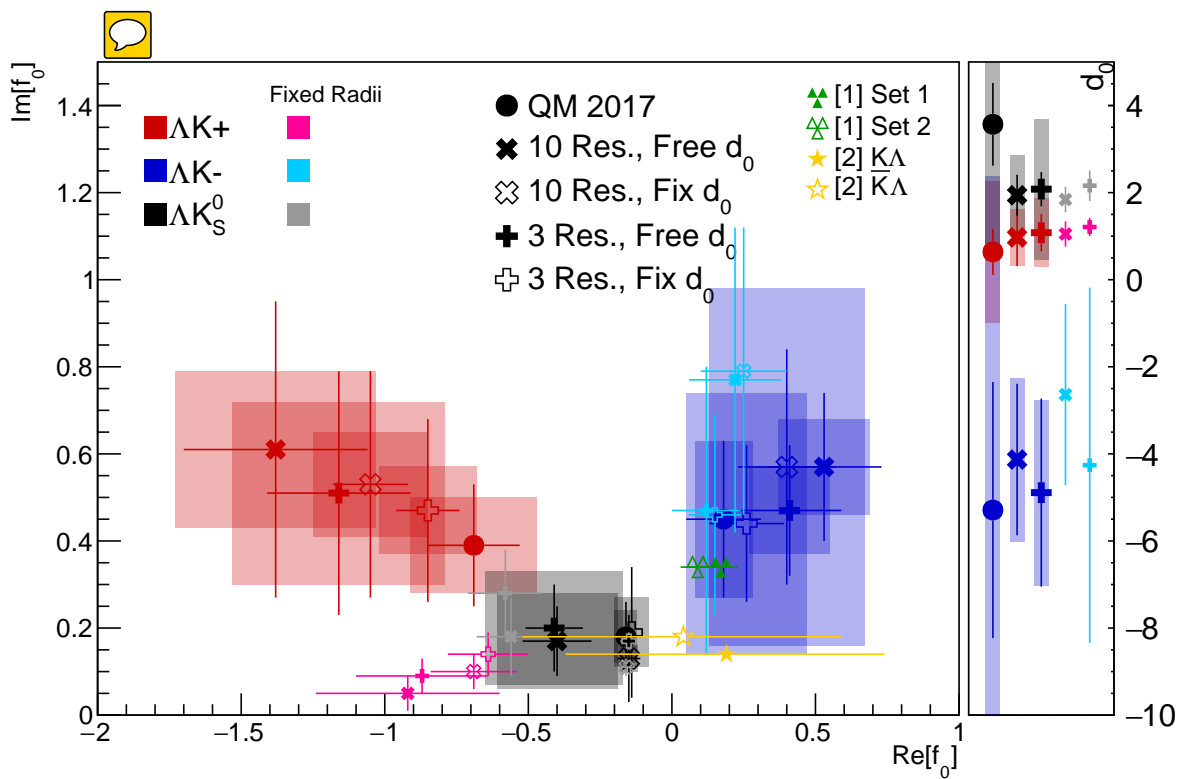


**Fig. 25:** Same as Fig. 21, but also including the case where  $d_0$  was fixed to zero in the fit.

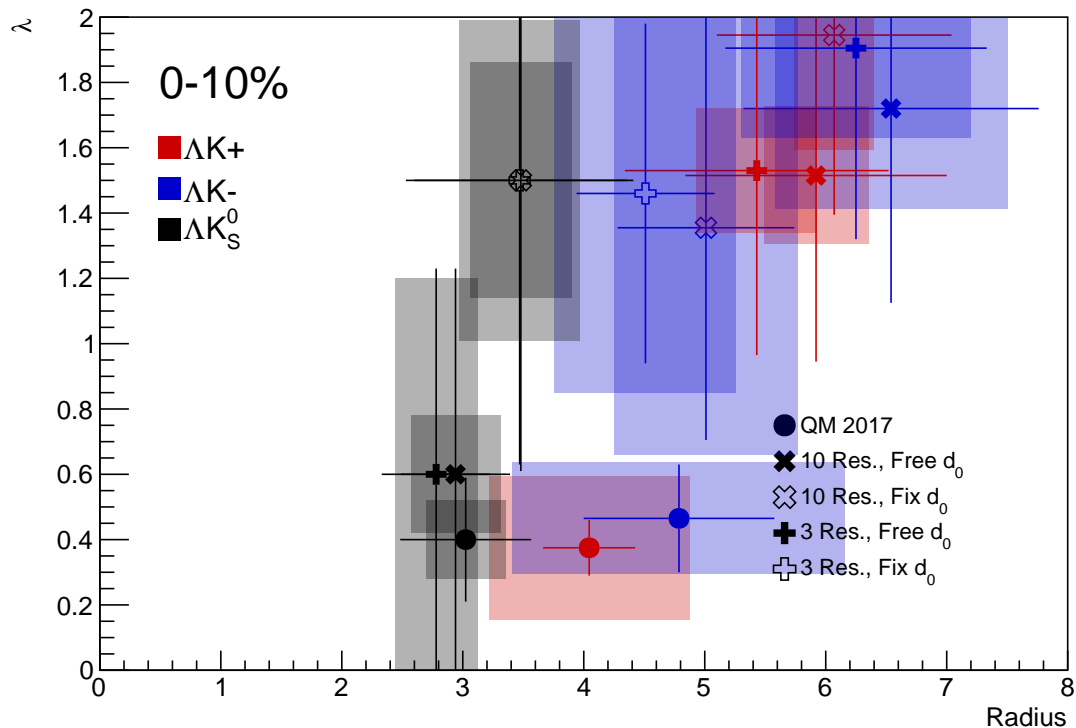


**Fig. 26:** Same as Fig. 22, but also including the case where  $d_0$  was fixed to zero in the fit.

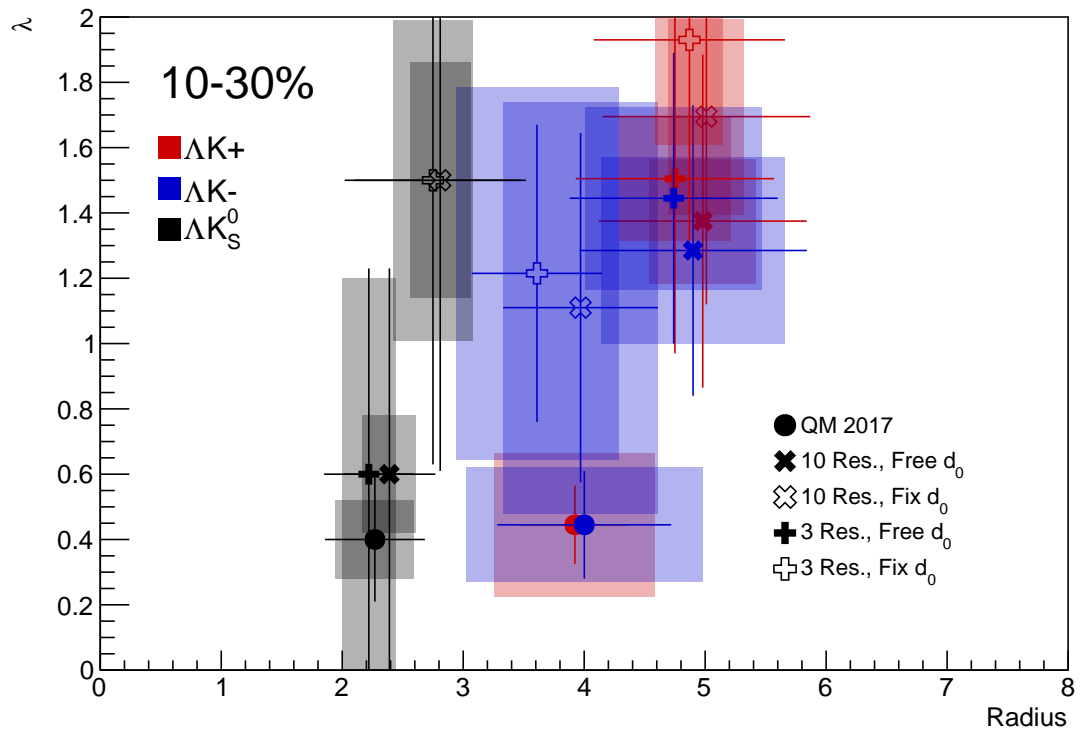


**Fig. 27:** Same as Fig. 23, but also including the case where  $d_0$  was fixed to zero in the fit.

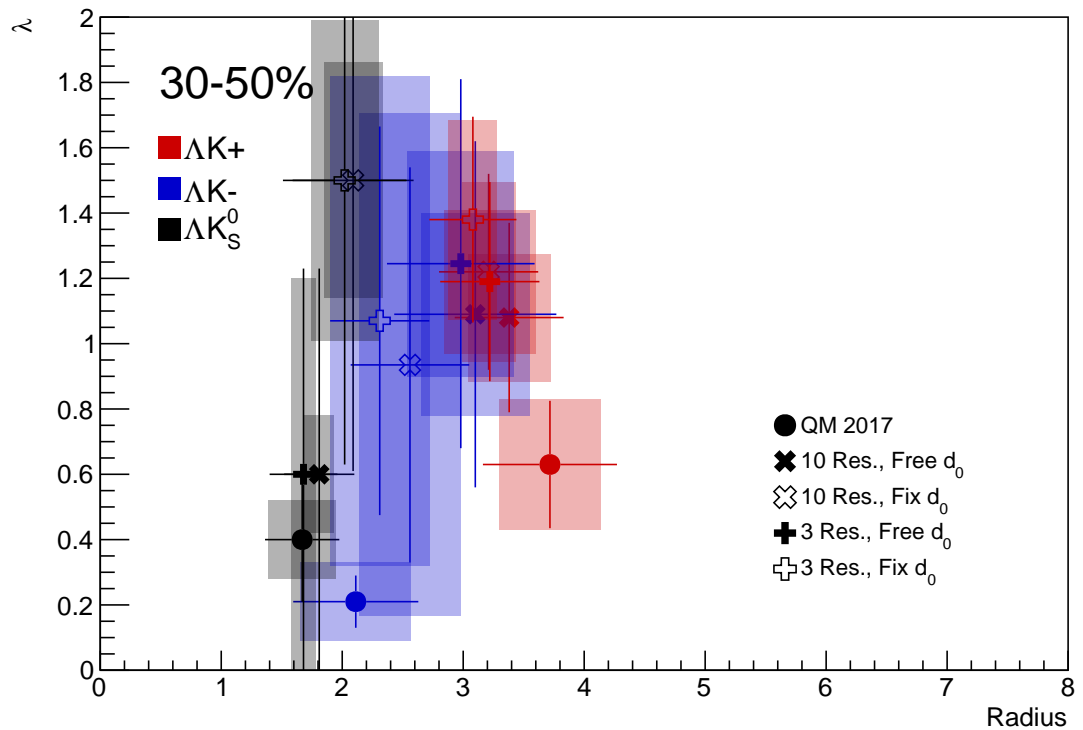
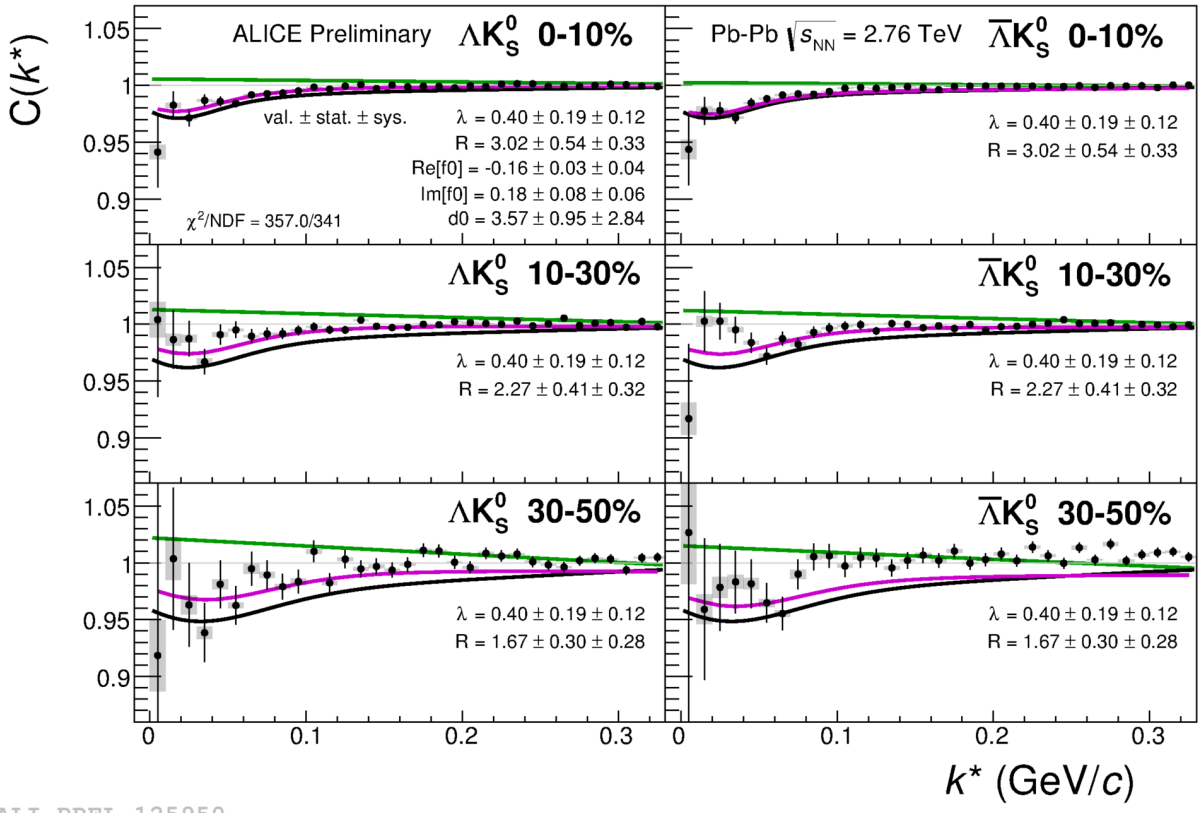


**Fig. 28:** Same as Fig. 24, but also including the case where  $d_0$  was fixed to zero in the fit.



ALI-PREL-125950

**Fig. 29:** Fits, with NO residual correlations included, to the  $\Lambda K_S^0$  (left) and  $\bar{\Lambda} K_S^0$  (right) data for the centralities 0-10% (top), 10-30% (middle), and 30-50% (bottom). The lines represent the statistical errors, while the boxes represent the systematic errors. Each has unique  $\lambda$  and normalization parameters. The radii are shared amongst like centralities; the scattering parameters ( $\mathbb{R}f_0, \mathbb{I}f_0, d_0$ ) are shared amongst all. The black solid line represents the “raw” fit, i.e. not corrected for momentum resolution effects nor non-flat background. The green line shows the fit to the non-flat background. The purple points show the fit after momentum resolution and non-flat background corrections have been applied. The initial values of the parameters is listed, as well as the final fit values with uncertainties. Here,  $R$  was restricted to [2.,10.] and  $\Lambda$  was restricted to [0.1,0.8].

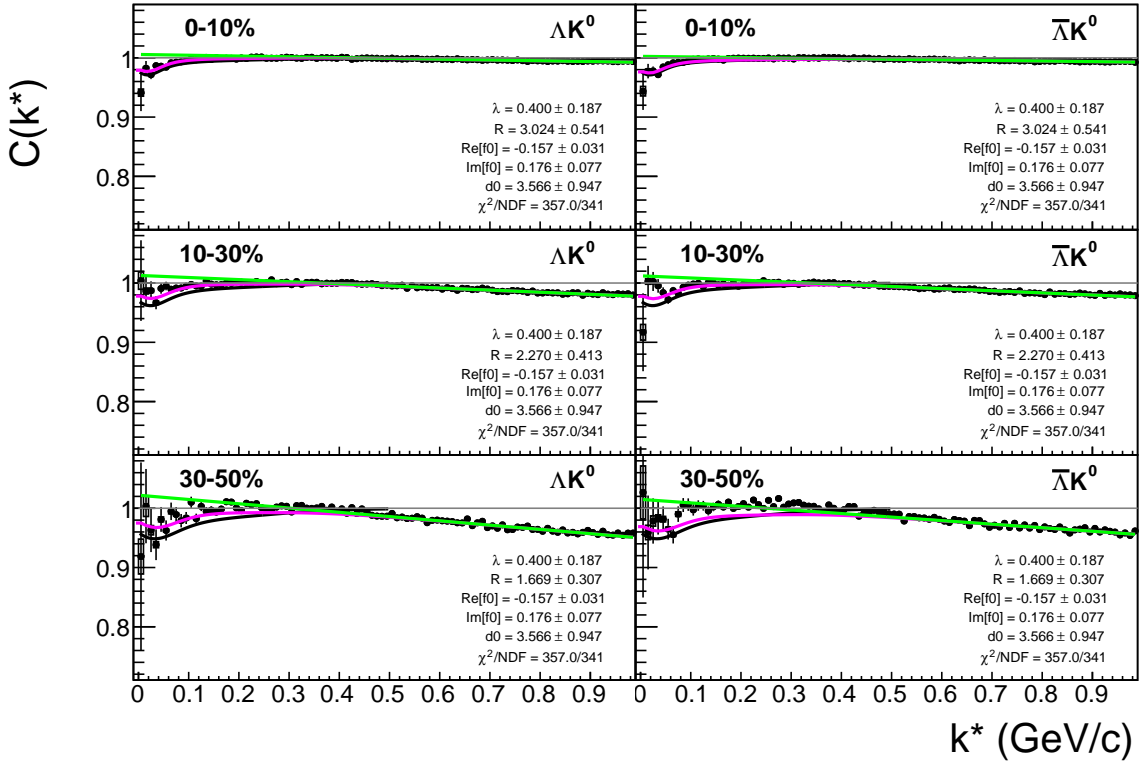
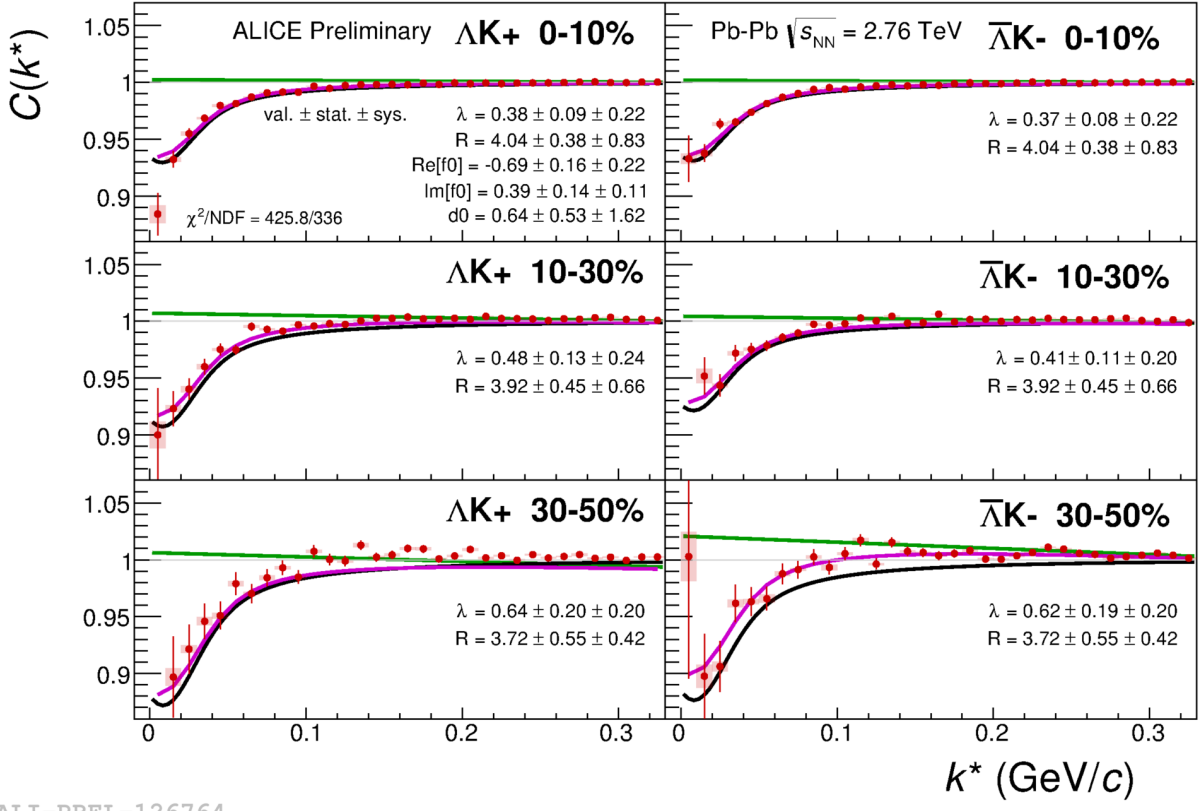


**Fig. 30:** Same as Fig. 29, but with a wider range of view. Fits, with NO residual correlations included, to the  $\Lambda K_S^0$  (left) and  $\bar{\Lambda} K_S^0$  (right) data for the centralities 0-10% (top), 10-30% (middle), and 30-50% (bottom). The lines represent the statistical errors, while the boxes represent the systematic errors. Each has unique  $\lambda$  and normalization parameters. The radii are shared amongst like centralities; the scattering parameters ( $\mathbb{R}f_0$ ,  $\mathbb{I}f_0$ ,  $d_0$ ) are shared amongst all. The black solid line represents the “raw” fit, i.e. not corrected for momentum resolution effects nor non-flat background. The green line shows the fit to the non-flat background. The purple points show the fit after momentum resolution and non-flat background corrections have been applied. The initial values of the parameters is listed, as well as the final fit values with uncertainties. Here,  $R$  was restricted to [2.,10.] and  $\Lambda$  was restricted to [0.1,0.8].



ALI-PREL-126764

**Fig. 31:** Fits to the  $\Lambda K^+$  (left) and  $\bar{\Lambda} K^-$  (right) data for the centralities 0-10% (top), 10-30% (middle), and 30-50% (bottom). The lines represent the statistical errors, while the boxes represent the systematic errors. Each has unique  $\lambda$  and normalization parameters. The radii are shared amongst like centralities; the scattering parameters ( $\text{Re}[f_0]$ ,  $\text{Im}[f_0]$ ,  $d_0$ ) are shared amongst all. The black solid line represents the “raw” fit, i.e. not corrected for momentum resolution effects nor non-flat background. The green line shows the fit to the non-flat background. The purple points show the fit after momentum resolution and non-flat background corrections have been applied. The initial values of the parameters is listed, as well as the final fit values with uncertainties.

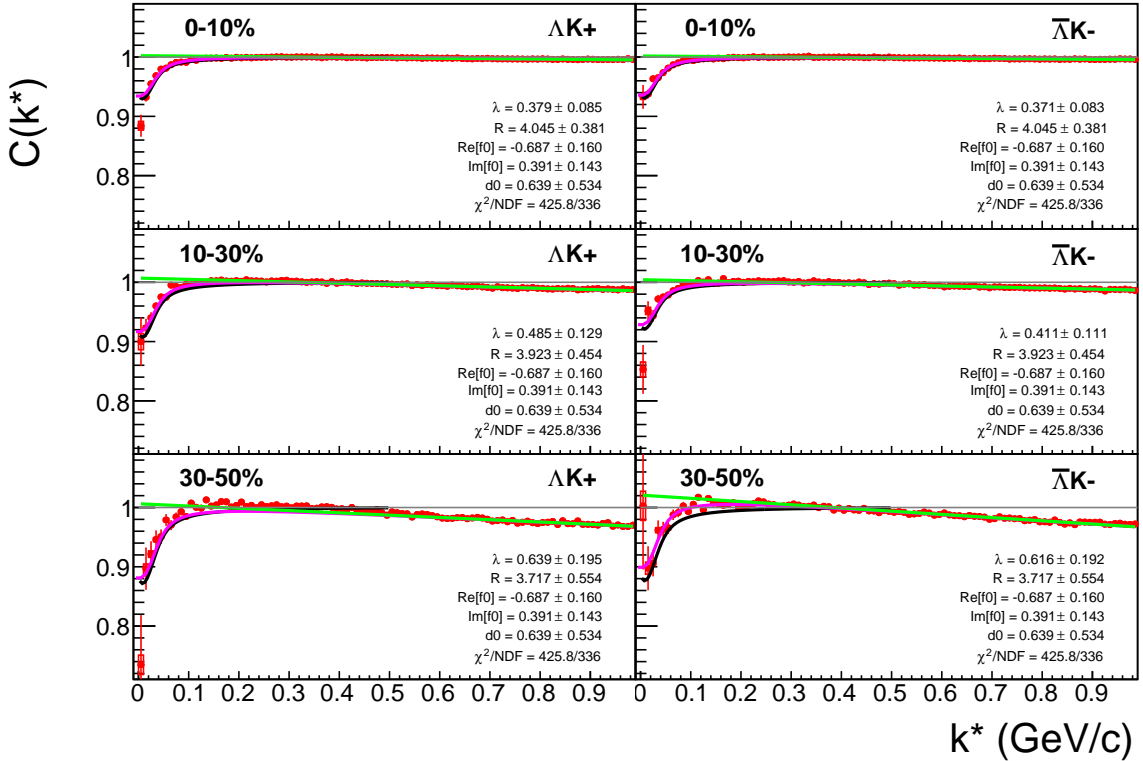
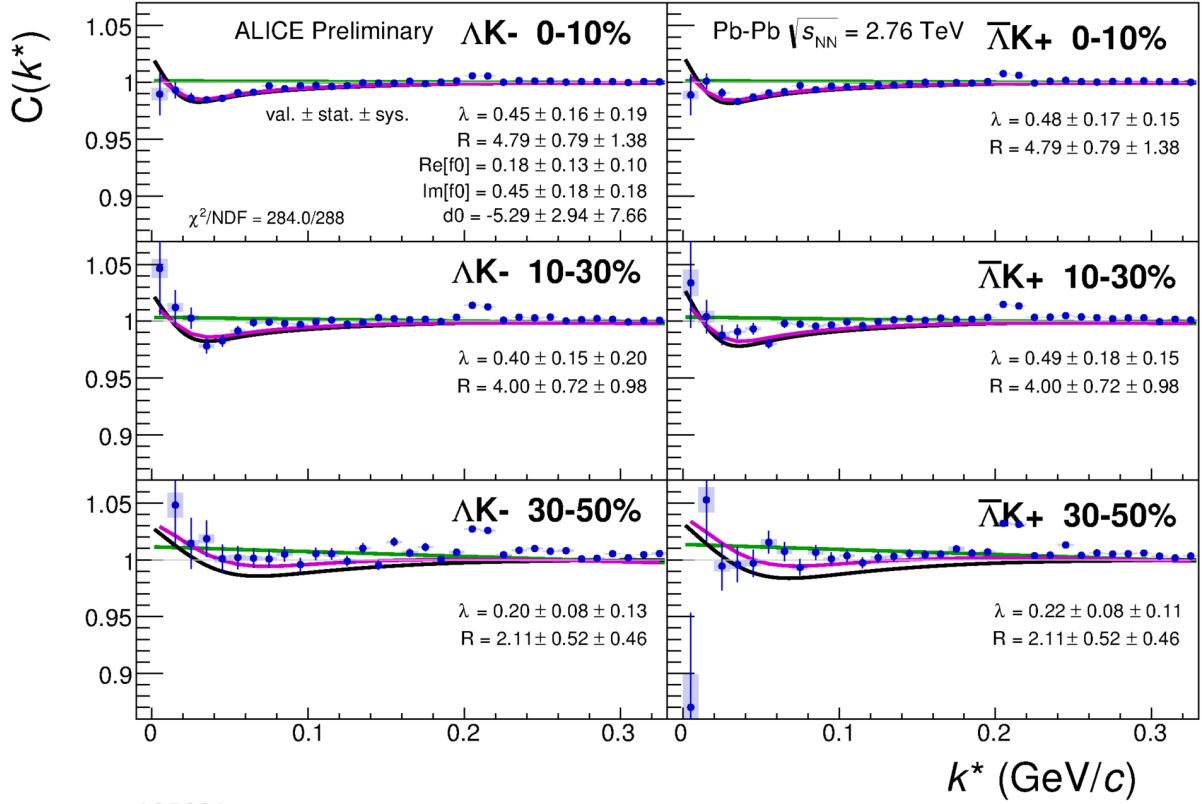


**Fig. 32:** Same as Fig. 31, but with a wider range of view. Fits, with NO residual correlations included, to the  $\Delta K^+$  (left) and  $\bar{\Delta} K^-$  (right) data for the centralities 0-10% (top), 10-30% (middle), and 30-50% (bottom). The lines represent the statistical errors, while the boxes represent the systematic errors. Each has unique  $\lambda$  and normalization parameters. The radii are shared amongst like centralities; the scattering parameters ( $\mathbb{R} f_0$ ,  $\mathbb{I} f_0$ ,  $d_0$ ) are shared amongst all. The black solid line represents the “raw” fit, i.e. not corrected for momentum resolution effects nor non-flat background. The green line shows the fit to the non-flat background. The purple points show the fit after momentum resolution and non-flat background corrections have been applied. The initial values of the parameters is listed, as well as the final fit values with uncertainties.



ALI-PREL-125931

**Fig. 33:** Fits, with NO residual correlations included, to the  $\Lambda K^-$  (left) with  $\bar{\Lambda} K^+$  (right) data for the centralities 0-10% (top), 10-30% (middle), and 30-50% (bottom). The lines represent the statistical errors, while the boxes represent the systematic errors. Each has unique  $\lambda$  and normalization parameters. The radii are shared amongst like centralities; the scattering parameters ( $\mathbb{R}f_0$ ,  $\mathbb{I}f_0$ ,  $d_0$ ) are shared amongst all. The black solid line represents the “raw” fit, i.e. not corrected for momentum resolution effects nor non-flat background. The green line shows the fit to the non-flat background. The purple points show the fit after momentum resolution and non-flat background corrections have been applied. The initial values of the parameters is listed, as well as the final fit values with uncertainties.

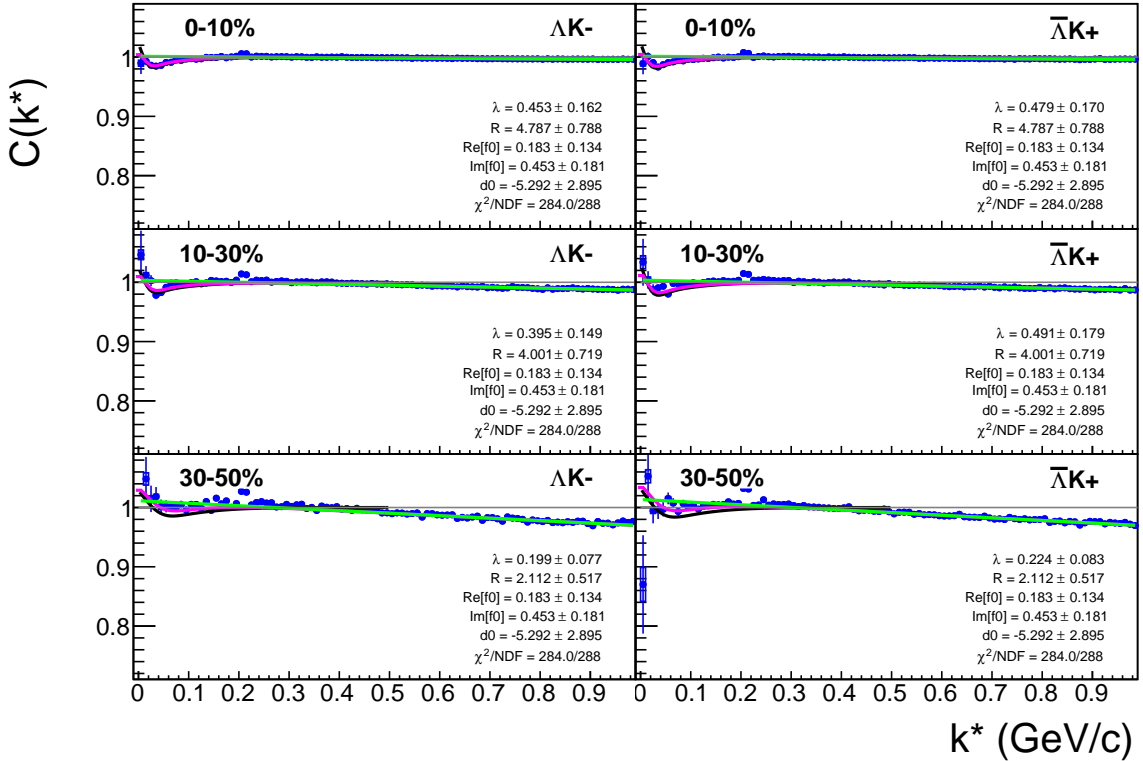


**Fig. 34:** Same as Fig. 33, but with a wider range of view. Fits, with NO residual correlations included, to the  $\Lambda K^-$  (left) with  $\bar{\Lambda} K^+$  (right) data for the centralities 0-10% (top), 10-30% (middle), and 30-50% (bottom). The lines represent the statistical errors, while the boxes represent the systematic errors. Each has unique  $\lambda$  and normalization parameters. The radii are shared amongst like centralities; the scattering parameters ( $\mathbb{R}f_0$ ,  $\mathbb{I}f_0$ ,  $d_0$ ) are shared amongst all. The black solid line represents the “raw” fit, i.e. not corrected for momentum resolution effects nor non-flat background. The green line shows the fit to the non-flat background. The purple points show the fit after momentum resolution and non-flat background corrections have been applied. The initial values of the parameters is listed, as well as the final fit values with uncertainties.

Fit Results $\Lambda(\bar{\Lambda})K_S^0$						
Pair Type	Centrality	Fit Parameters				
		$\lambda$	$R$	$\mathbb{R}f_0$	$\mathbb{I}f_0$	$d_0$
$\Lambda K_S^0$	0-10%	$0.400 \pm 0.187$ (stat.) $\pm 0.116$ (sys.)	$3.024 \pm 0.541$ (stat.) $\pm 0.329$ (sys.)	$-0.157 \pm 0.031$ (stat.) $\pm 0.043$ (sys.)	$0.176 \pm 0.077$ (stat.) $\pm 0.059$ (sys.)	$3.566 \pm 0.947$ (stat.) $\pm 2.836$ (sys.)
	10-30%		$2.270 \pm 0.413$ (stat.) $\pm 0.324$ (sys.)			
	30-50%		$1.669 \pm 0.307$ (stat.) $\pm 0.280$ (sys.)			
$\bar{\Lambda} K_S^0$	0-10%	$0.400 \pm 0.187$ (stat.) $\pm 0.116$ (sys.)	$3.024 \pm 0.541$ (stat.) $\pm 0.329$ (sys.)	$-0.157 \pm 0.031$ (stat.) $\pm 0.043$ (sys.)	$0.176 \pm 0.077$ (stat.) $\pm 0.059$ (sys.)	$3.566 \pm 0.947$ (stat.) $\pm 2.836$ (sys.)
	10-30%		$2.270 \pm 0.413$ (stat.) $\pm 0.324$ (sys.)			
	30-50%		$1.669 \pm 0.307$ (stat.) $\pm 0.280$ (sys.)			

**Table 1:** Fit Results  $\Lambda(\bar{\Lambda})K_S^0$ . Each pair is fit simultaneously with its conjugate (ie.  $\Lambda K_S^0$  with  $\bar{\Lambda} K_S^0$ ) across all centralities (0-10%, 10-30%, 30-50%), for a total of 6 simultaneous analyses in the fit. Each analysis has a unique  $\lambda$  and normalization parameter. The radii are shared between analyses of like centrality, as these should have similar source sizes. The scattering parameters ( $\mathbb{R}f_0$ ,  $\mathbb{I}f_0$ ,  $d_0$ ) are shared amongst all. The fit is done on the data with only statistical error bars. The errors marked as “stat.” are those returned by MINUIT. The errors marked as “sys.” are those which result from my systematic analysis (as outlined in Section 6).

Fit Results $\Lambda(\bar{\Lambda})K^\pm$						
Pair Type	Centrality	Fit Parameters				
		$\lambda$	$R$	$\mathbb{R}f_0$	$\mathbb{I}f_0$	$d_0$
$\Lambda K^+$	0-10%	$0.379 \pm 0.085$ (stat.) $\pm 0.220$ (sys.)	$4.045 \pm 0.381$ (stat.) $\pm 0.830$ (sys.)	$-0.687 \pm 0.160$ (stat.) $\pm 0.223$ (sys.)	$0.391 \pm 0.143$ (stat.) $\pm 0.111$ (sys.)	$0.639 \pm 0.534$ (stat.) $\pm 1.621$ (sys.)
	10-30%		$0.485 \pm 0.129$ (stat.) $\pm 0.241$ (sys.)	$3.923 \pm 0.454$ (stat.) $\pm 0.663$ (sys.)		
	30-50%		$0.639 \pm 0.195$ (stat.) $\pm 0.204$ (sys.)	$3.717 \pm 0.554$ (stat.) $\pm 0.420$ (sys.)		
$\bar{\Lambda} K^-$	0-10%	$0.371 \pm 0.083$ (stat.) $\pm 0.217$ (sys.)	$4.045 \pm 0.381$ (stat.) $\pm 0.830$ (sys.)			
	10-30%		$0.411 \pm 0.111$ (stat.) $\pm 0.201$ (sys.)	$3.923 \pm 0.454$ (stat.) $\pm 0.663$ (sys.)		
	30-50%		$0.616 \pm 0.192$ (stat.) $\pm 0.203$ (sys.)	$3.717 \pm 0.554$ (stat.) $\pm 0.420$ (sys.)		
$\Lambda K^-$	0-10%	$0.453 \pm 0.162$ (stat.) $\pm 0.186$ (sys.)	$4.787 \pm 0.788$ (stat.) $\pm 1.375$ (sys.)	$0.183 \pm 0.134$ (stat.) $\pm 0.095$ (sys.)	$0.453 \pm 0.181$ (stat.) $\pm 0.184$ (sys.)	$-5.292 \pm 2.895$ (stat.) $\pm 7.658$ (sys.)
	10-30%		$0.395 \pm 0.149$ (stat.) $\pm 0.198$ (sys.)	$4.001 \pm 0.719$ (stat.) $\pm 0.978$ (sys.)		
	30-50%		$0.199 \pm 0.077$ (stat.) $\pm 0.132$ (sys.)	$2.112 \pm 0.517$ (stat.) $\pm 0.457$ (sys.)		
$\bar{\Lambda} K^+$	0-10%	$0.479 \pm 0.170$ (stat.) $\pm 0.152$ (sys.)	$4.787 \pm 0.788$ (stat.) $\pm 1.375$ (sys.)			
	10-30%		$0.491 \pm 0.179$ (stat.) $\pm 0.148$ (sys.)	$4.001 \pm 0.719$ (stat.) $\pm 0.978$ (sys.)		
	30-50%		$0.224 \pm 0.083$ (stat.) $\pm 0.106$ (sys.)	$2.112 \pm 0.517$ (stat.) $\pm 0.457$ (sys.)		

**Table 2:** Fit Results  $\Lambda(\bar{\Lambda})K^\pm$  Each pair is fit simultaneously with its conjugate (ie.  $\Lambda K^+$  with  $\bar{\Lambda} K^-$  and  $\Lambda K^-$  with  $\bar{\Lambda} K^+$ ) across all centralities (0-10%, 10-30%, 30-50%), for a total of 6 simultaneous analyses in the fit. Each analysis has a unique  $\lambda$  and normalization parameter. The radii are shared between analyses of like centrality, as these should have similar source sizes. The scattering parameters ( $\mathbb{R}f_0$ ,  $\mathbb{I}f_0$ ,  $d_0$ ) are shared amongst all. The fit is done on the data with only statistical error bars. The errors marked as “stat.” are those returned by MINUIT. The errors marked as “sys.” are those which result from my systematic analysis (as outlined in Section 6).



**Fit Parameters (value  $\pm$  statistical error  $\pm$  systematic error)**

Pair Type	Centrality	R		
		$\Re f_0$	$\Im f_0$	$d_0$
$\Lambda K^+ & \bar{\Lambda} K^-$	0-10%		<b><math>4.04 \pm 0.38 \pm 0.83</math></b>	
	10-30%		<b><math>3.92 \pm 0.45 \pm 0.66</math></b>	
	30-50%		<b><math>3.72 \pm 0.55 \pm 0.42</math></b>	
		<b><math>-0.69 \pm 0.16 \pm 0.22</math></b>	<b><math>0.39 \pm 0.14 \pm 0.11</math></b>	<b><math>0.64 \pm 0.53 \pm 1.62</math></b>
$\Lambda K^- & \bar{\Lambda} K^+$	0-10%		<b><math>4.79 \pm 0.79 \pm 1.38</math></b>	
	10-30%		<b><math>4.00 \pm 0.72 \pm 0.98</math></b>	
	30-50%		<b><math>2.11 \pm 0.52 \pm 0.46</math></b>	
		<b><math>0.18 \pm 0.13 \pm 0.10</math></b>	<b><math>0.45 \pm 0.18 \pm 0.18</math></b>	<b><math>-5.29 \pm 2.94 \pm 7.66</math></b>
$\Lambda K_S^0 & \bar{\Lambda} K_S^0$	0-10%		<b><math>3.02 \pm 0.54 \pm 0.33</math></b>	
	10-30%		<b><math>2.27 \pm 0.41 \pm 0.32</math></b>	
	30-50%		<b><math>1.67 \pm 0.30 \pm 0.28</math></b>	
		<b><math>-0.16 \pm 0.03 \pm 0.04</math></b>	<b><math>0.18 \pm 0.08 \pm 0.06</math></b>	<b><math>3.57 \pm 0.95 \pm 2.84</math></b>

Figure 49 shows extracted  $R_{\text{inv}}$  parameters as a function of transverse mass ( $m_T$ ) for various pair systems over several centralities. The published ALICE data [10] is shown with transparent, open symbols. The new  $\Lambda K$  results are shown with opaque, filled symbols. The radii show an increasing size with increasing centrality, as is expected from the simple geometric picture of the collisions. The radii decrease in size with increasing  $m_T$ , and we see an approximate scaling of the radii with transverse mass, as is expected in the presence of collective flow in the system.

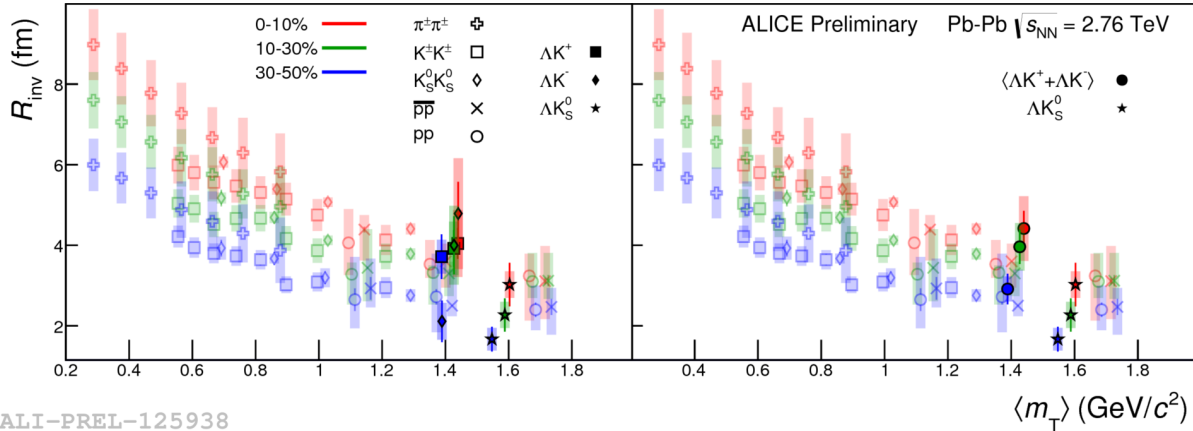


**Fig. 35:** No residual correlations in  $\Lambda K$  fits. Extracted fit  $R_{\text{inv}}$  parameters as a function of pair transverse mass ( $m_T$ ) for various pair systems over several centralities. The ALICE published data [10] is shown with transparent, open symbols. The new  $\Lambda K$  results are shown with opaque, filled symbols. In the left, the  $\Lambda K^+$  (with its conjugate pair) results are shown separately from the  $\Lambda K^-$  (with its conjugate pair) results. In the right, all  $\Lambda K^\pm$  results are averaged.

### 7.1.2 Results: $\Lambda K_S^0$ and $\Lambda K^\pm$ : 3 Residual Correlations Included in Fit

### 7.1.3 Results: $\Lambda K_S^0$ and $\Lambda K^\pm$ : 10 Residual Correlations Included in Fit

## 7.2 Results: $\Xi K^\pm$

Even without any fits to the data, the fact that the  $\Xi^- K^+$  data dips below unity (Fig. 50) is exciting, as this cannot occur purely from a Coulomb interaction. We hope that this dip signifies that we are able to peer through the overwhelming contribution from the Coulomb interaction to see the effects arising from the strong interaction.

Figure 51 demonstrates graphically, that the  $\Xi^- K^+$  results cannot be described by solely the Coulomb interaction. In this figure, we present the data along with a Coulomb-only band. The Coulomb-only band is spanned by two Coulomb-only curves, whose parameters are given in the figure. The Coulomb-only curves were generated using a technique identical to the generation of the fit function, described in Sec. 5.2, except, of course, with the nuclear scattering parameters all set to zero. The Coulomb-only curves change monotonically with varying  $\lambda$  or varying radius parameters, therefore, any curves built with parameter sets intermediate to those used in the Coulomb-only band will be contained in the band.

Including the strong interaction into the simulation can dramatically change the resulting correlation function, as shown in Figure 52. In the figure, the solid line represents a Coulomb-only curve, i.e. a simulated correlation function with the strong interaction turned off. The dashed lines represent a full simulation, including both the strong and Coulomb interactions. The two dashed lines differ only in the real part of the assumed scattering length: positive in Set 1, and negative in Set 2. In the top figure, for the  $\Xi^- K^+$  simulation, we see that parameter set 2, with a negative real part of the scattering length, causes the simulated curve to dip below unity, as is seen in the data. If there is a parallel to be drawn between this analysis and the  $\Lambda K$  analysis, we expect to see similar effects in the  $\Lambda K^+$  system and the

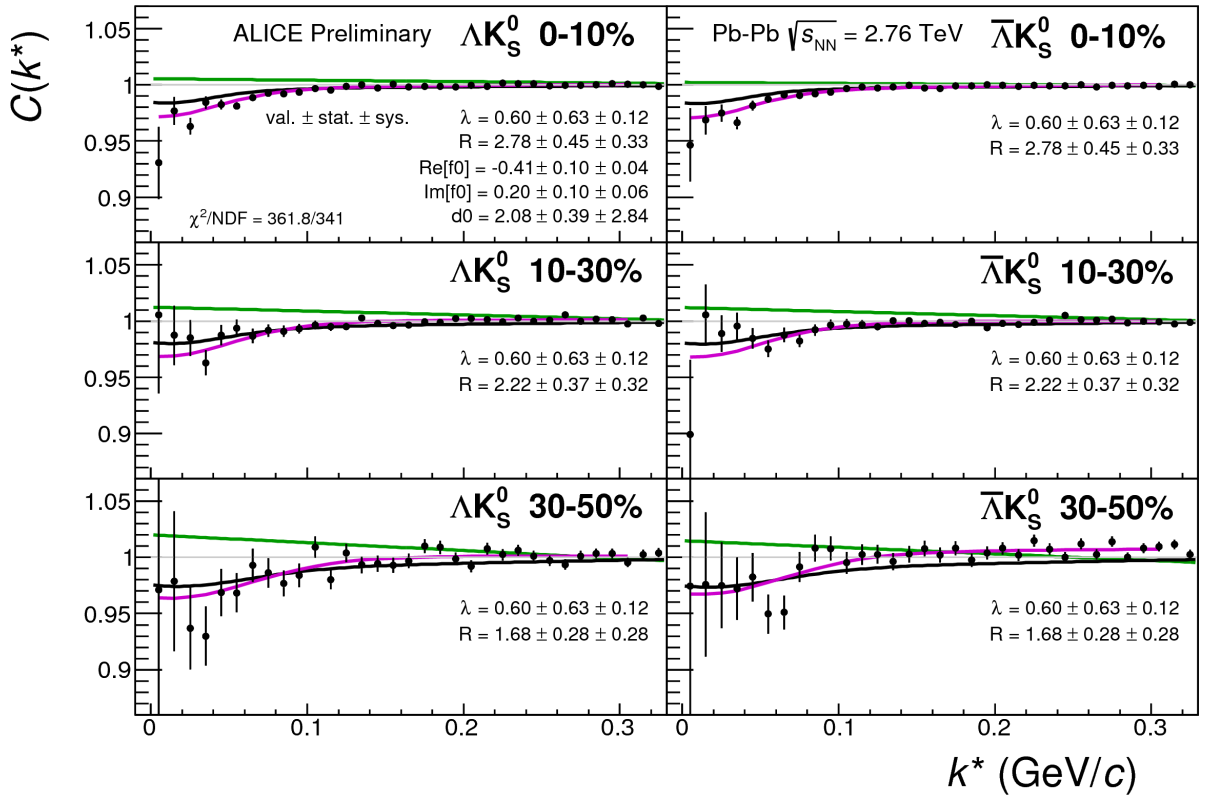
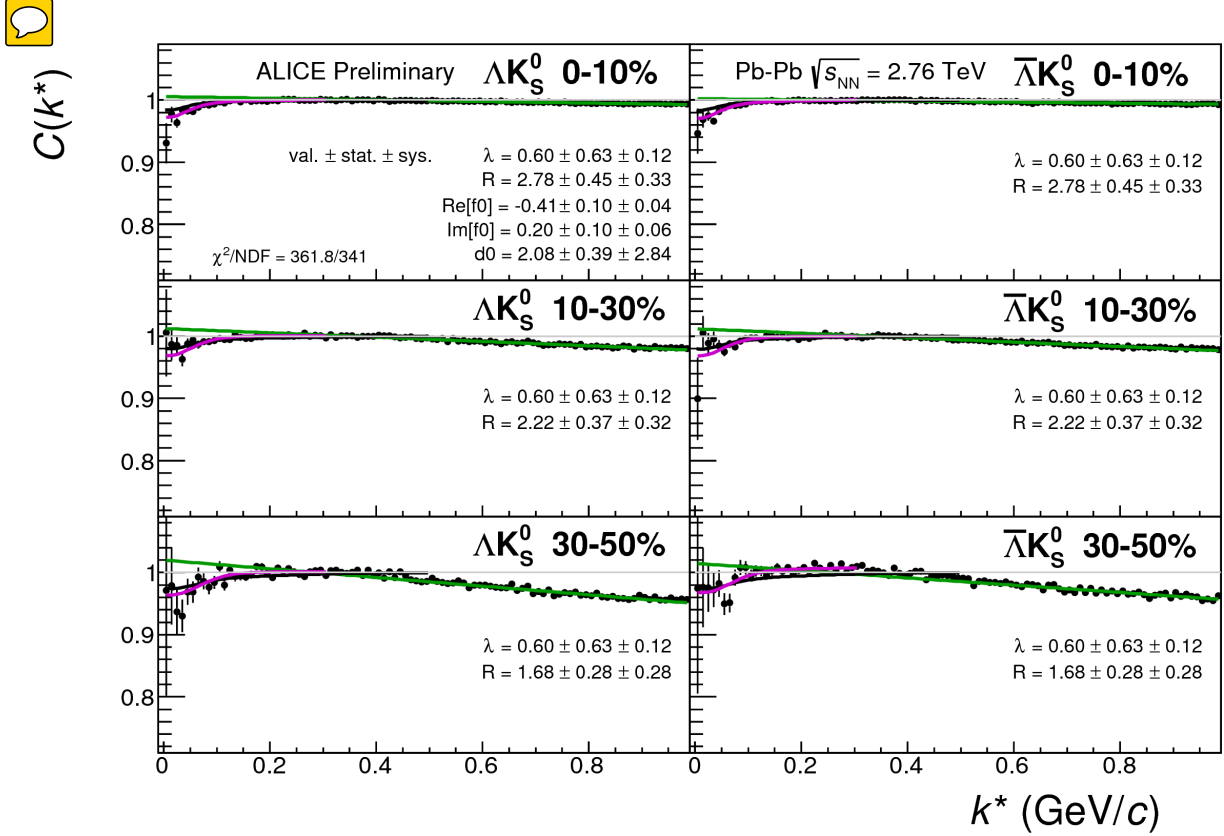


**Fig. 36:** Fits, with 3 residual correlations included, to the  $\Lambda K_s^0$  (left) and  $\bar{\Lambda} K_s^0$  (right) data for the centralities 0-10% (top), 10-30% (middle), and 30-50% (bottom). The lines represent the statistical errors, while the boxes represent the systematic errors. Each has unique  $\lambda$  and normalization parameters. The radii are shared amongst like centralities; the scattering parameters ( $\mathbb{R}f_0, \mathbb{I}f_0, d_0$ ) are shared amongst all. The black solid line represents the “raw” fit, i.e. not corrected for momentum resolution effects nor non-flat background. The green line shows the fit to the non-flat background. The purple points show the fit after momentum resolution and non-flat background corrections have been applied. The initial values of the parameters is listed, as well as the final fit values with uncertainties. Here,  $R$  was restricted to [2.,10.] and  $\Lambda$  was restricted to [0.1,0.8].

657  $\Xi^- K^+$  systems. In these systems, we could have an  $s\bar{s}$  annihilation picture. Or, another possible way of  
 658 thinking about these systems is in terms of net strangeness. The  $\Lambda K^+$  system has  $S=0$ , while the  $\Lambda K^-$   
 659 has  $S=-2$ . The  $\Xi^- K^+$  has  $S=-1$ , while the  $\Xi^- K^-$  has  $S=-3$ .

660 The author was asked to perform a global Coulomb-only fit to the data, to ensure that the system truly  
 661 could not be described simply by the Coulomb interaction. In order words, in the fit, the strong force was  
 662 turned off, and the  $\Xi^- K^+$ ,  $\bar{\Xi}^+ K^-$ ,  $\Xi^- K^-$ ,  $\bar{\Xi}^+ K^+$  systems all share one sinlge radius parameter, while the  
 663 pair and conjugate pair systems share a  $\lambda$  parameter. The results of this fit are shown in Figures 53 and  
 664 54. In Fig. 53, there was a lower limit of 0.1 fm placed on the radius parameter, and the radius parameter  
 665 was initialized to 3 fm (as seems reasonable, when considering the transverse mass of the system and  
 666 looking at Fig. 49). As is shown in the results, the radius parameter reached this unrealistic lower bound  
 667 of 0.1 fm. In Fig. 54, the parameters were all unbounded, and the radius parameter was initialized to 10  
 668 fm. In this case, the radius parameters reamins high, and ends at an unrealistic value of 10.84 fm. In both  
 669 cases, the  $\lambda$  parameters are too low. From these figures, we conclude that a global Coulomb-only fit is  
 670 not suitable for the data.

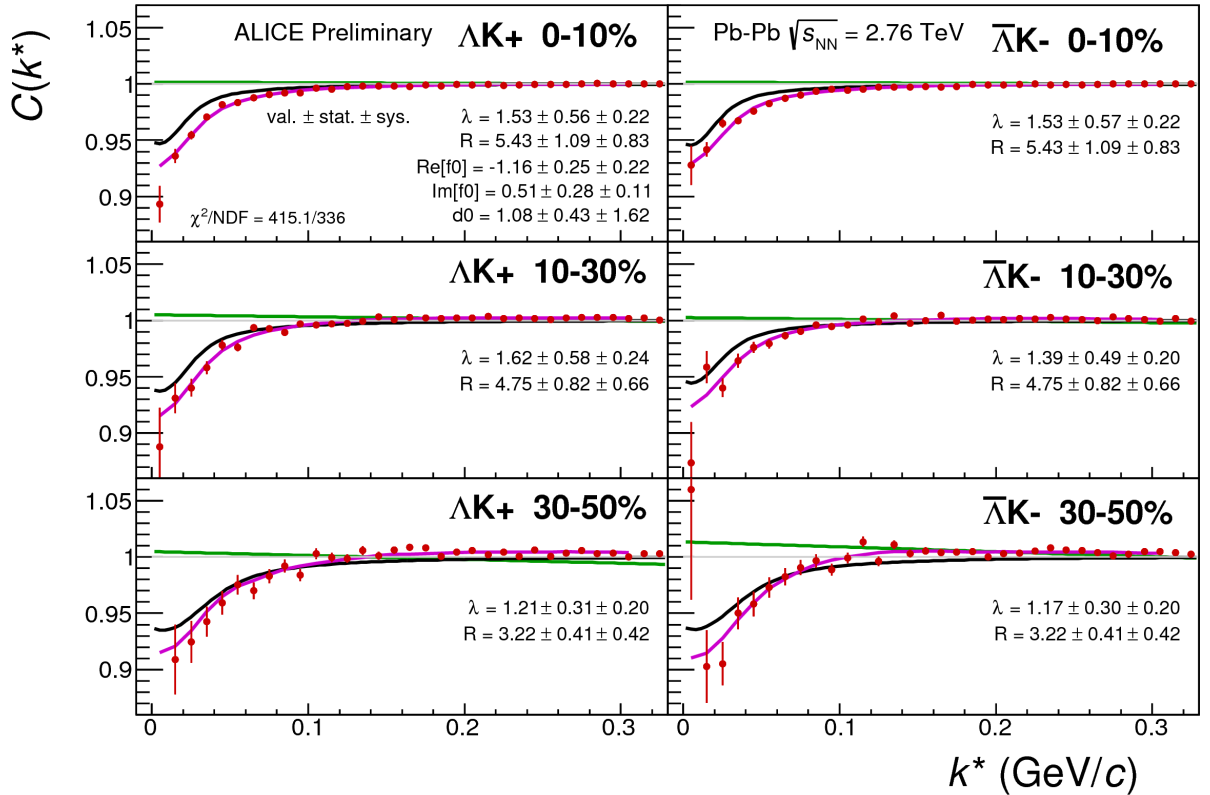
671 Although the global Coulomb-only fit failed, it is possible that a Coulomb-only fit performed on  $\Xi^- K^+$   
 672 and  $\bar{\Xi}^+ K^-$  separately from  $\Xi^- K^-$  and  $\bar{\Xi}^+ K^+$  could be suitable. The result of such fits are shown in  
 673 Figures 55 and 56. Figure 55, shows that the fit is not able to describe the dip in the  $\Xi^- K^+$  data below



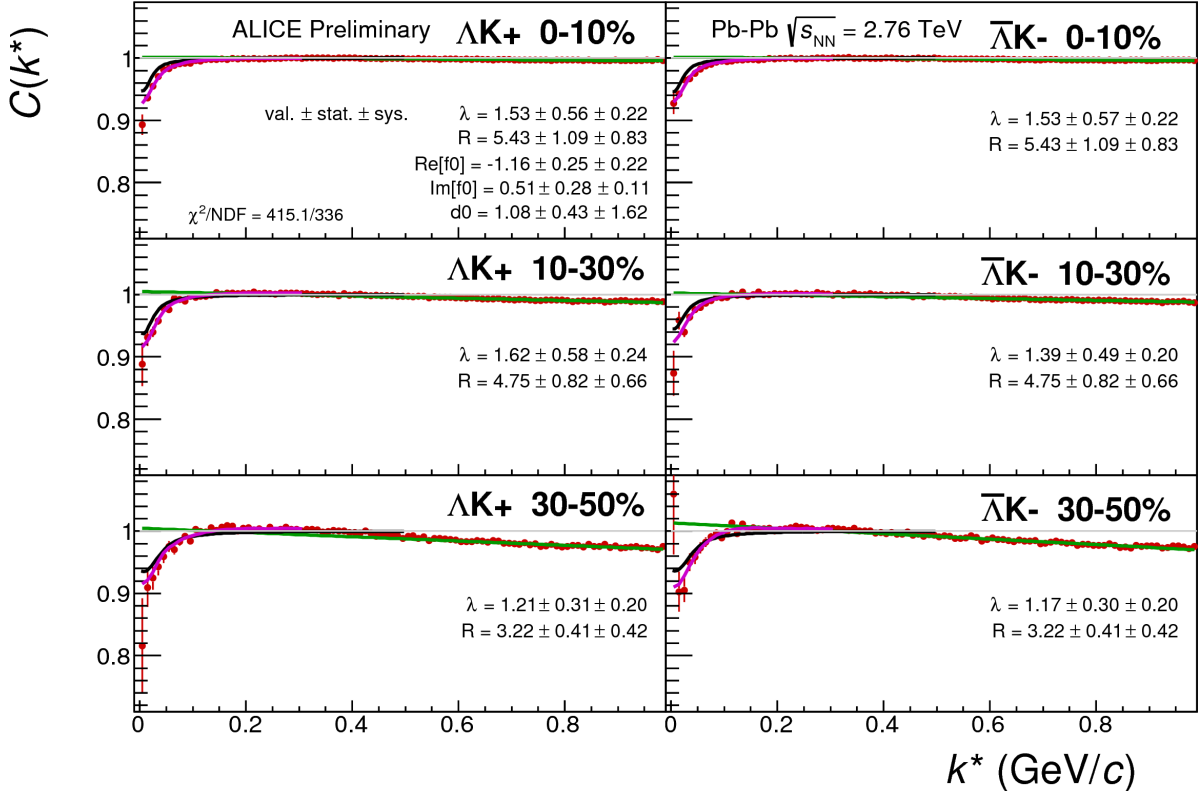
**Fig. 37:** Same as Fig. 36, but with a wider range of view. Fits, with 3 residual correlations included, to the  $\Lambda K_S^0$  (left) and  $\bar{\Lambda} K_S^0$  (right) data for the centralities 0-10% (top), 10-30% (middle), and 30-50% (bottom). The lines represent the statistical errors, while the boxes represent the systematic errors. Each has unique  $\lambda$  and normalization parameters. The radii are shared amongst like centralities; the scattering parameters ( $Re[f_0]$ ,  $Im[f_0]$ ,  $d_0$ ) are shared amongst all. The black solid line represents the “raw” fit, i.e. not corrected for momentum resolution effects nor non-flat background. The green line shows the fit to the non-flat background. The purple points show the fit after momentum resolution and non-flat background corrections have been applied. The initial values of the parameters is listed, as well as the final fit values with uncertainties. Here,  $R$  was restricted to [2.,10.] and  $\Lambda$  was restricted to [0.1,0.8].

674 unity. Of course, this is obviously true for an attractive Coulomb-only fit. The radius parameter of  
 675 8.43 fm extracted from this fit is unrealistically large. In Figure 56 shows the Coulomb-only fit can  
 676 described the  $\Xi^- K^-$  data reasonable well; although the extracted radius of 3.73 fm is somewhat larger  
 677 than expected.

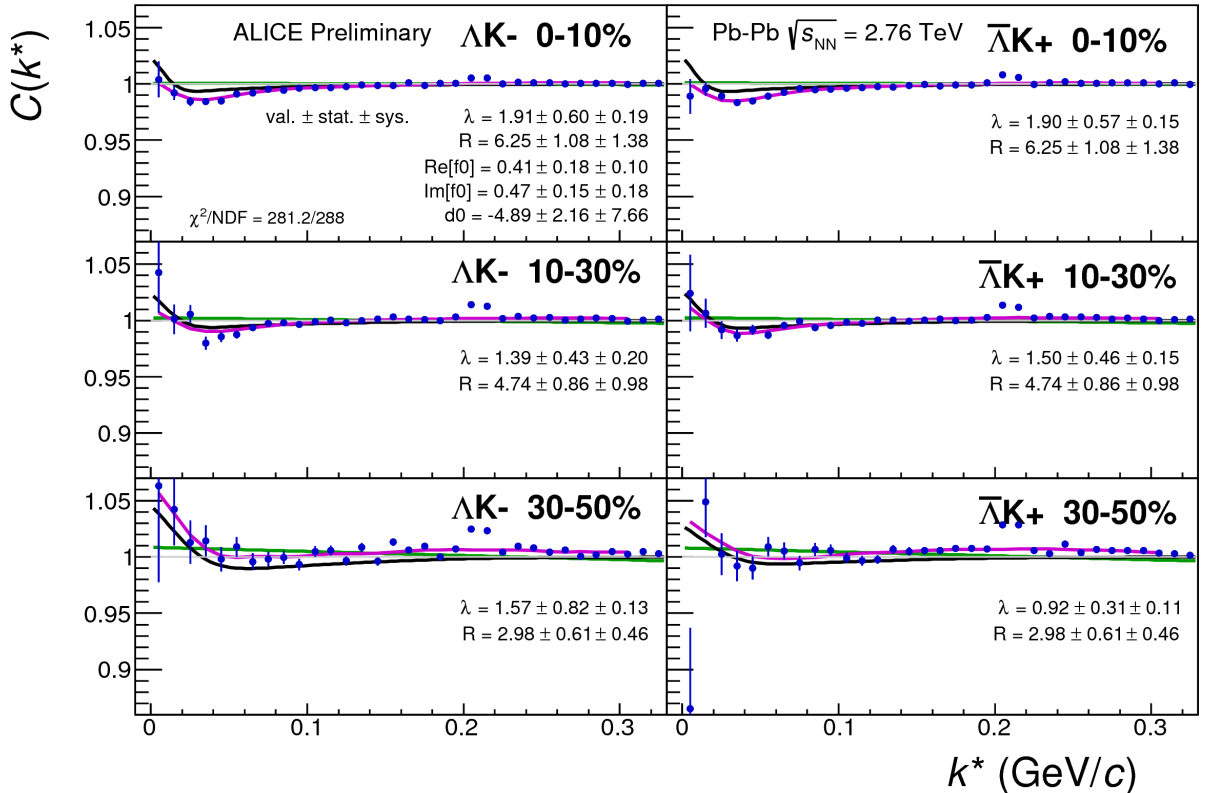
## 678 8 To Do



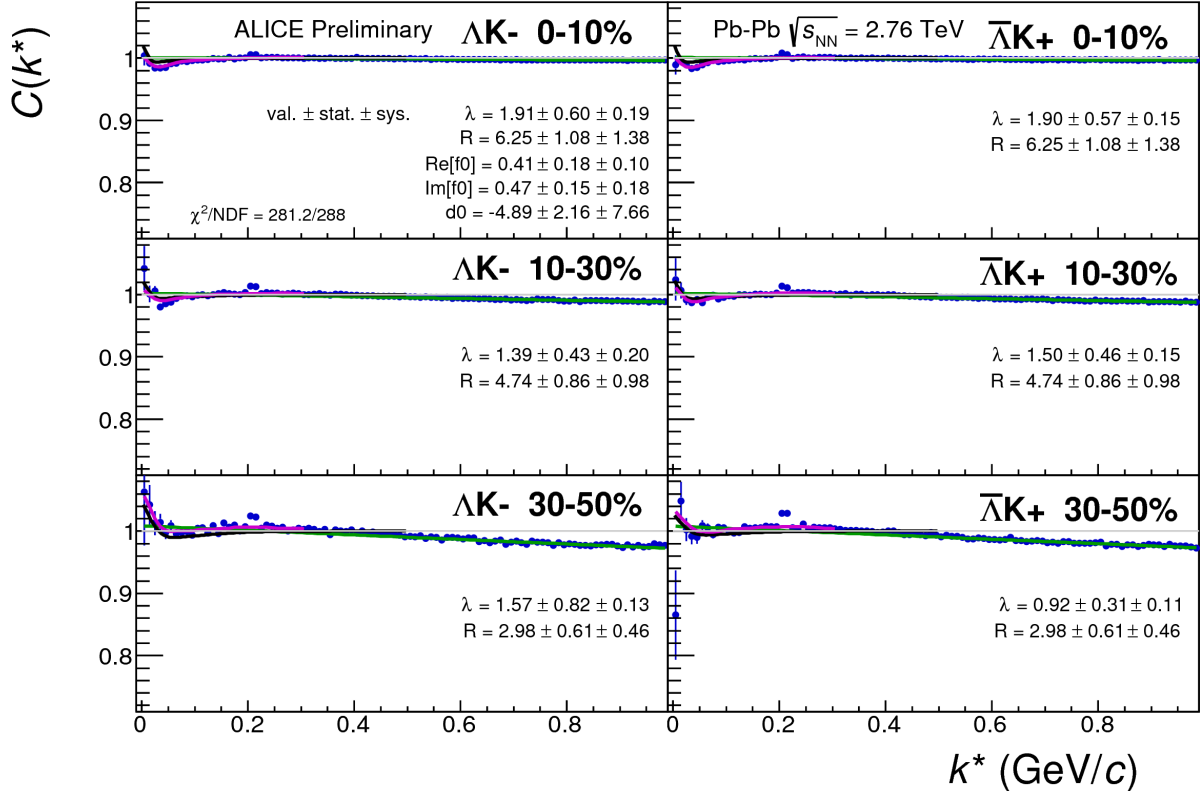
**Fig. 38:** Fits, with 3 residual correlations included, to the  $\Lambda K^+$  (left) and  $\bar{\Lambda} K^-$  (right) data for the centralities 0-10% (top), 10-30% (middle), and 30-50% (bottom). The lines represent the statistical errors, while the boxes represent the systematic errors. Each has unique  $\lambda$  and normalization parameters. The radii are shared amongst like centralities; the scattering parameters ( $\mathbb{R}f_0$ ,  $\mathbb{I}f_0$ ,  $d_0$ ) are shared amongst all. The black solid line represents the “raw” fit, i.e. not corrected for momentum resolution effects nor non-flat background. The green line shows the fit to the non-flat background. The purple points show the fit after momentum resolution and non-flat background corrections have been applied. The initial values of the parameters is listed, as well as the final fit values with uncertainties.



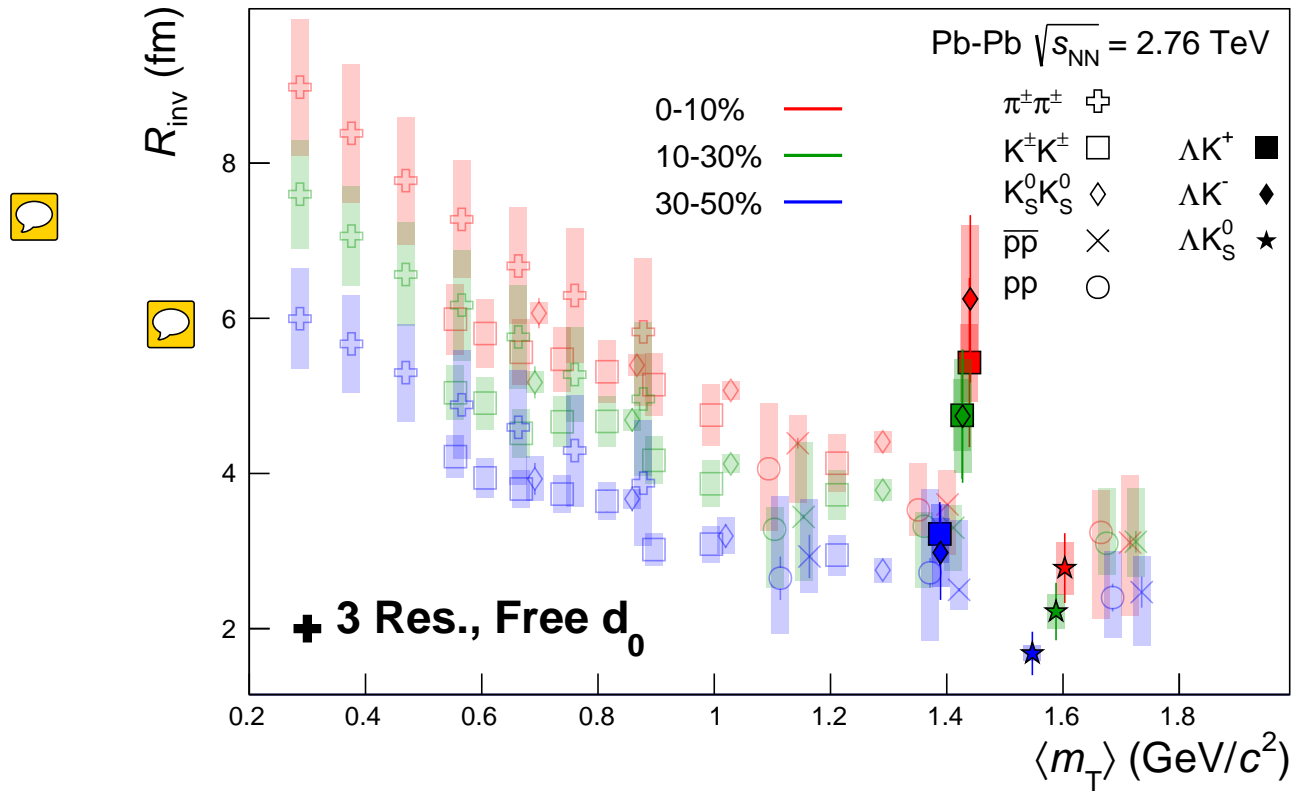
**Fig. 39:** Same as Fig. 38, but with a wider range of view. Fits, with 3 residual correlations included, to the  $\Lambda K^+$  (left) and  $\bar{\Lambda} K^-$  (right) data for the centralities 0-10% (top), 10-30% (middle), and 30-50% (bottom). The lines represent the statistical errors, while the boxes represent the systematic errors. Each has unique  $\lambda$  and normalization parameters. The radii are shared amongst like centralities; the scattering parameters ( $\mathbb{R}f_0$ ,  $\mathbb{I}f_0$ ,  $d_0$ ) are shared amongst all. The black solid line represents the “raw” fit, i.e. not corrected for momentum resolution effects nor non-flat background. The green line shows the fit to the non-flat background. The purple points show the fit after momentum resolution and non-flat background corrections have been applied. The initial values of the parameters is listed, as well as the final fit values with uncertainties.



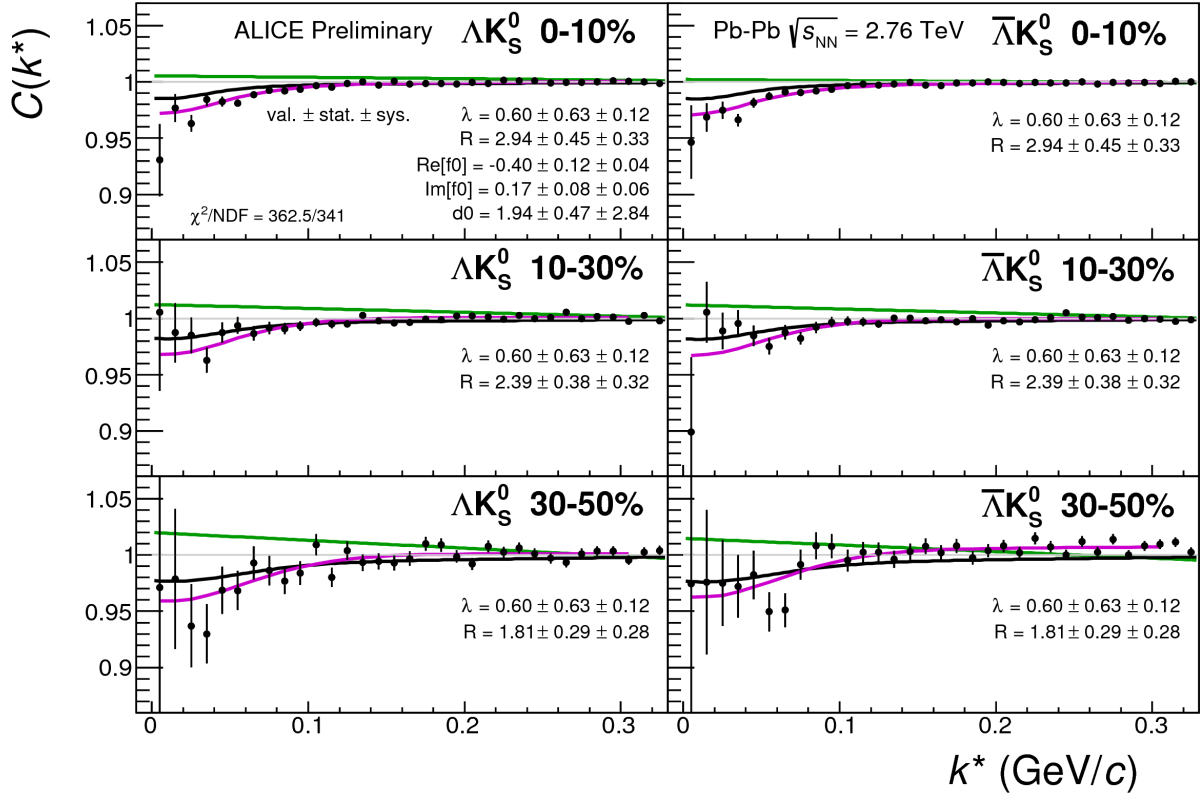
**Fig. 40:** Fits, with 3 residual correlations included, to the  $\Lambda K^-$  (left) with  $\bar{\Lambda} K^+$  (right) data for the centralities 0-10% (top), 10-30% (middle), and 30-50% (bottom). The lines represent the statistical errors, while the boxes represent the systematic errors. Each has unique  $\lambda$  and normalization parameters. The radii are shared amongst like centralities; the scattering parameters ( $\mathbb{R} f_0$ ,  $\mathbb{I} f_0$ ,  $d_0$ ) are shared amongst all. The black solid line represents the “raw” fit, i.e. not corrected for momentum resolution effects nor non-flat background. The green line shows the fit to the non-flat background. The purple points show the fit after momentum resolution and non-flat background corrections have been applied. The initial values of the parameters is listed, as well as the final fit values with uncertainties.



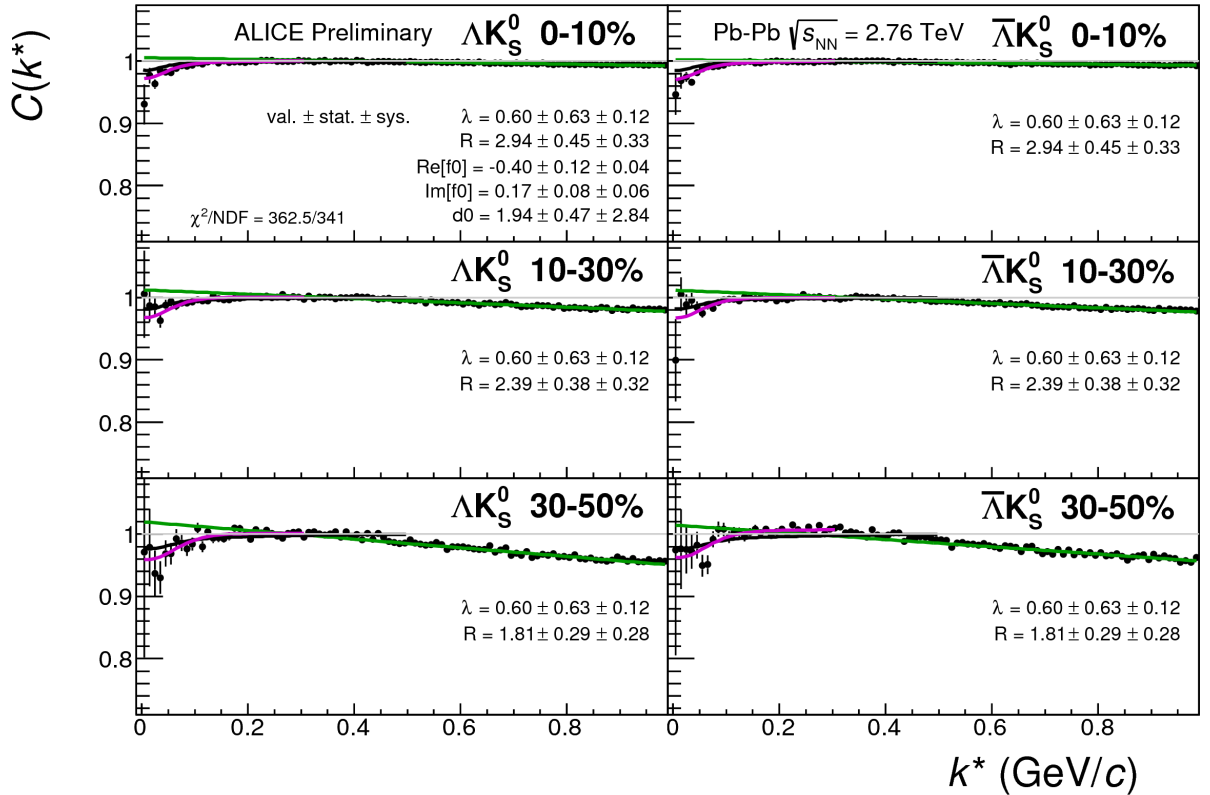
**Fig. 41:** Same as Fig. 40, but with a wider range of view. Fits, with 3 residual correlations included, to the  $\Lambda K^-$  (left) with  $\bar{\Lambda} K^+$  (right) data for the centralities 0-10% (top), 10-30% (middle), and 30-50% (bottom). The lines represent the statistical errors, while the boxes represent the systematic errors. Each has unique  $\lambda$  and normalization parameters. The radii are shared amongst like centralities; the scattering parameters ( $\text{Re}[f_0]$ ,  $\text{Im}[f_0]$ ,  $d_0$ ) are shared amongst all. The black solid line represents the “raw” fit, i.e. not corrected for momentum resolution effects nor non-flat background. The green line shows the fit to the non-flat background. The purple points show the fit after momentum resolution and non-flat background corrections have been applied. The initial values of the parameters is listed, as well as the final fit values with uncertainties.



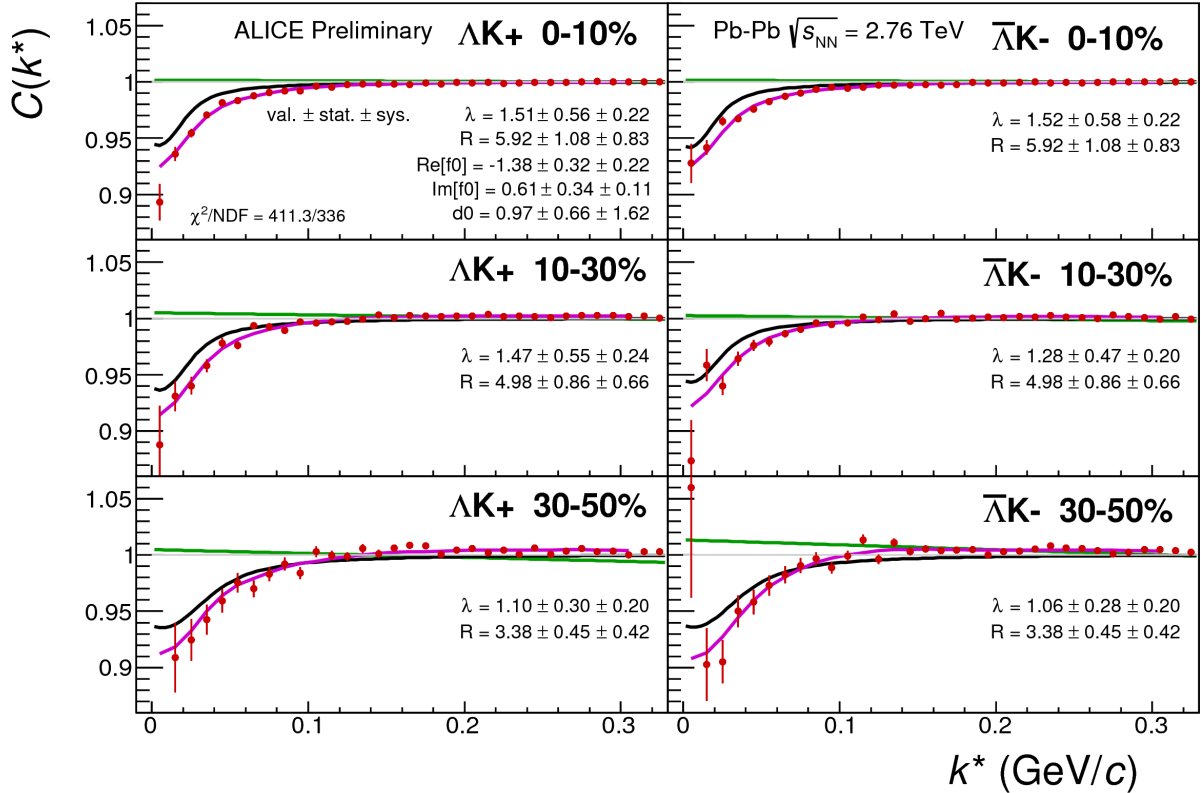
**Fig. 42:** 3 residual correlations in  $\Lambda K$  fits. Extracted fit  $R_{\text{inv}}$  parameters as a function of pair transverse mass ( $m_T$ ) for various pair systems over several centralities. The ALICE published data [10] is shown with transparent, open symbols. The new  $\Lambda K$  results are shown with opaque, filled symbols. In the left, the  $\Lambda K^+$  (with its conjugate pair) results are shown separately from the  $\Lambda K^-$  (with its conjugate pair) results. In the right, all  $\Lambda K^\pm$  results are averaged.



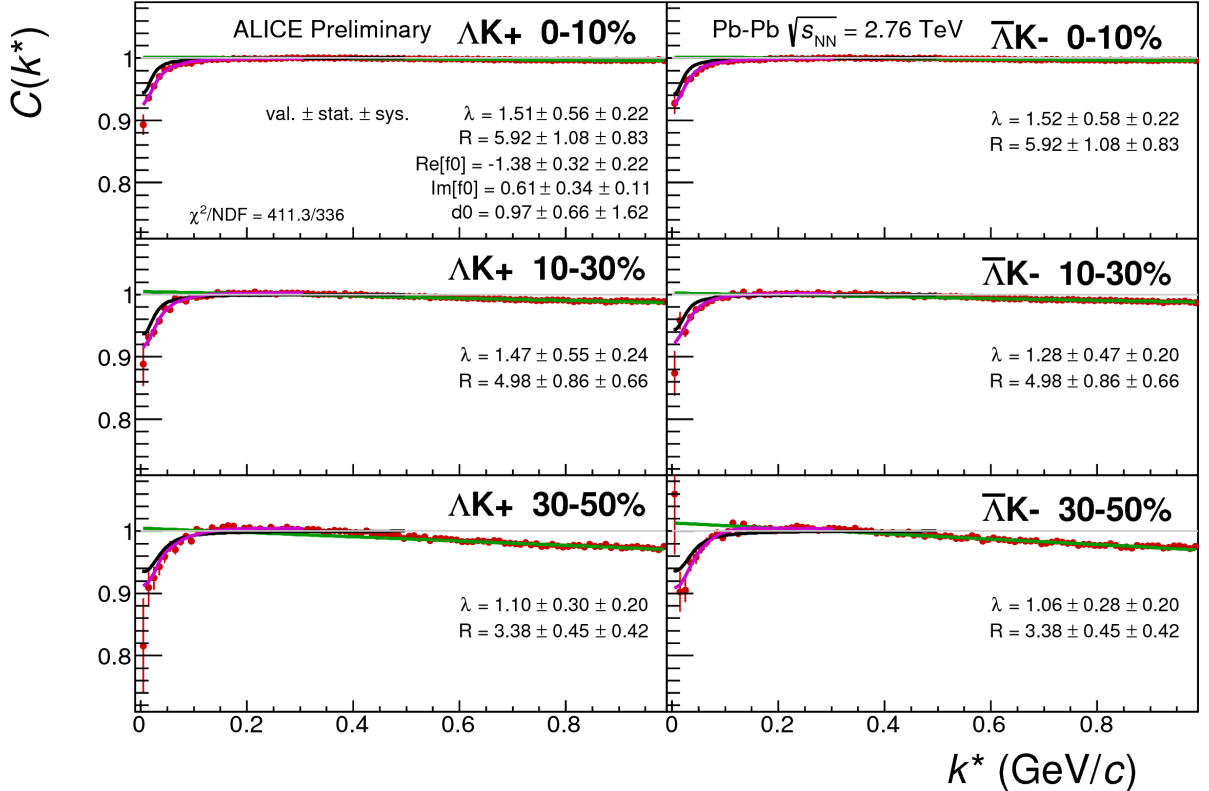
**Fig. 43:** Fits, with 10 residual correlations included, to the  $\Lambda K_S^0$  (left) and  $\bar{\Lambda} K_S^0$  (right) data for the centralities 0-10% (top), 10-30% (middle), and 30-50% (bottom). The lines represent the statistical errors, while the boxes represent the systematic errors. Each has unique  $\lambda$  and normalization parameters. The radii are shared amongst like centralities; the scattering parameters ( $\text{Re}[f_0]$ ,  $\text{Im}[f_0]$ ,  $d_0$ ) are shared amongst all. The black solid line represents the “raw” fit, i.e. not corrected for momentum resolution effects nor non-flat background. The green line shows the fit to the non-flat background. The purple points show the fit after momentum resolution and non-flat background corrections have been applied. The initial values of the parameters is listed, as well as the final fit values with uncertainties. Here,  $R$  was restricted to [2.,10.] and  $\Lambda$  was restricted to [0.1,0.8].



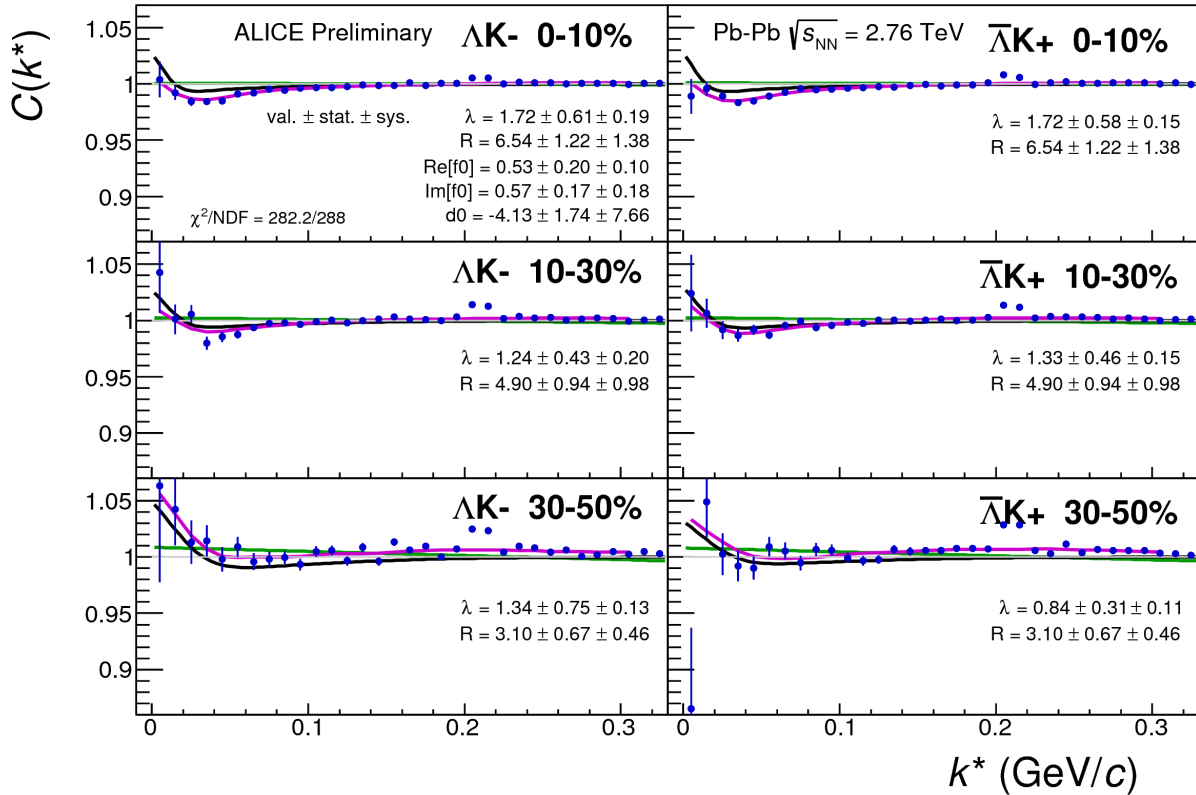
**Fig. 44:** Same as Fig. 43, but with a wider range of view. Fits, with 10 residual correlations included, to the  $\Lambda K_s^0$  (left) and  $\bar{\Lambda} K_s^0$  (right) data for the centralities 0-10% (top), 10-30% (middle), and 30-50% (bottom). The lines represent the statistical errors, while the boxes represent the systematic errors. Each has unique  $\lambda$  and normalization parameters. The radii are shared amongst like centralities; the scattering parameters ( $\mathbb{R} f_0$ ,  $\mathbb{I} f_0$ ,  $d_0$ ) are shared amongst all. The black solid line represents the “raw” fit, i.e. not corrected for momentum resolution effects nor non-flat background. The green line shows the fit to the non-flat background. The purple points show the fit after momentum resolution and non-flat background corrections have been applied. The initial values of the parameters is listed, as well as the final fit values with uncertainties. Here,  $R$  was restricted to [2.,10.] and  $\Lambda$  was restricted to [0.1,0.8].



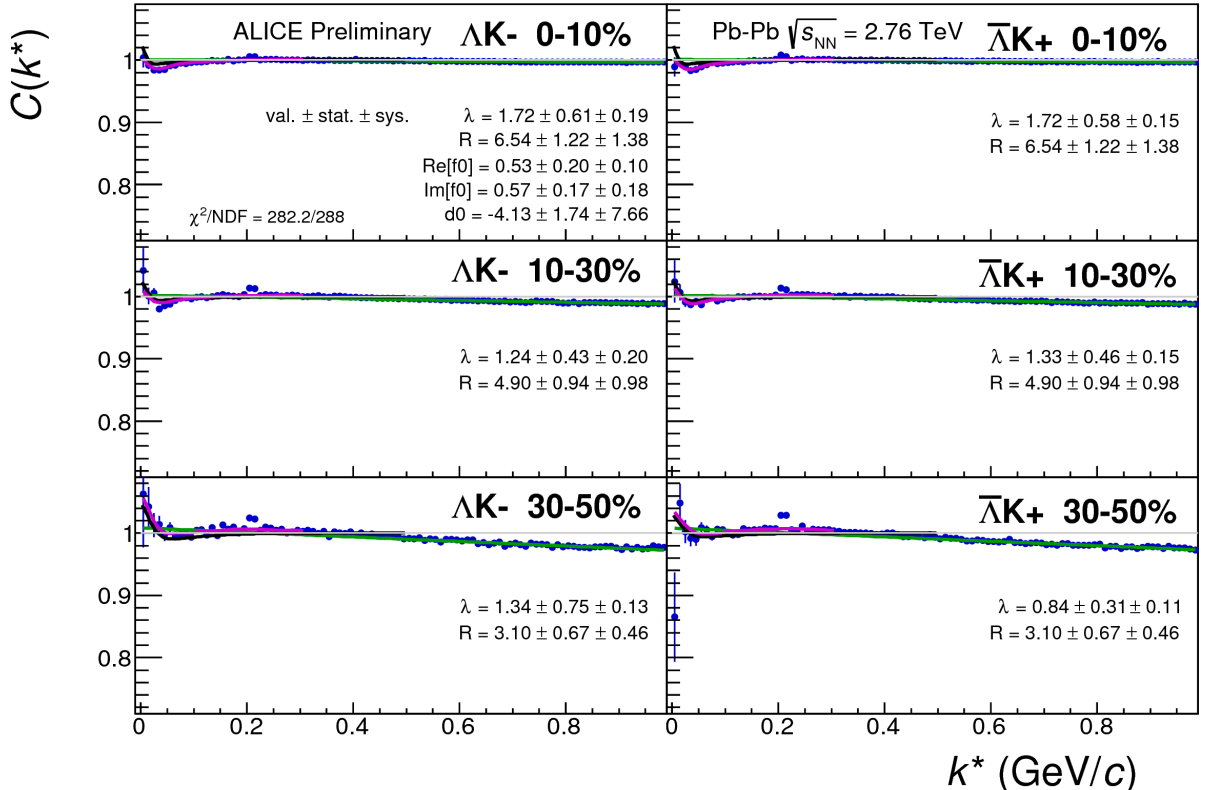
**Fig. 45:** Fits, with 10 residual correlations included, to the  $\Lambda K^+$  (left) and  $\bar{\Lambda} K^-$  (right) data for the centralities 0-10% (top), 10-30% (middle), and 30-50% (bottom). The lines represent the statistical errors, while the boxes represent the systematic errors. Each has unique  $\lambda$  and normalization parameters. The radii are shared amongst like centralities; the scattering parameters ( $\text{Re}[f_0]$ ,  $\text{Im}[f_0]$ ,  $d_0$ ) are shared amongst all. The black solid line represents the “raw” fit, i.e. not corrected for momentum resolution effects nor non-flat background. The green line shows the fit to the non-flat background. The purple points show the fit after momentum resolution and non-flat background corrections have been applied. The initial values of the parameters is listed, as well as the final fit values with uncertainties.



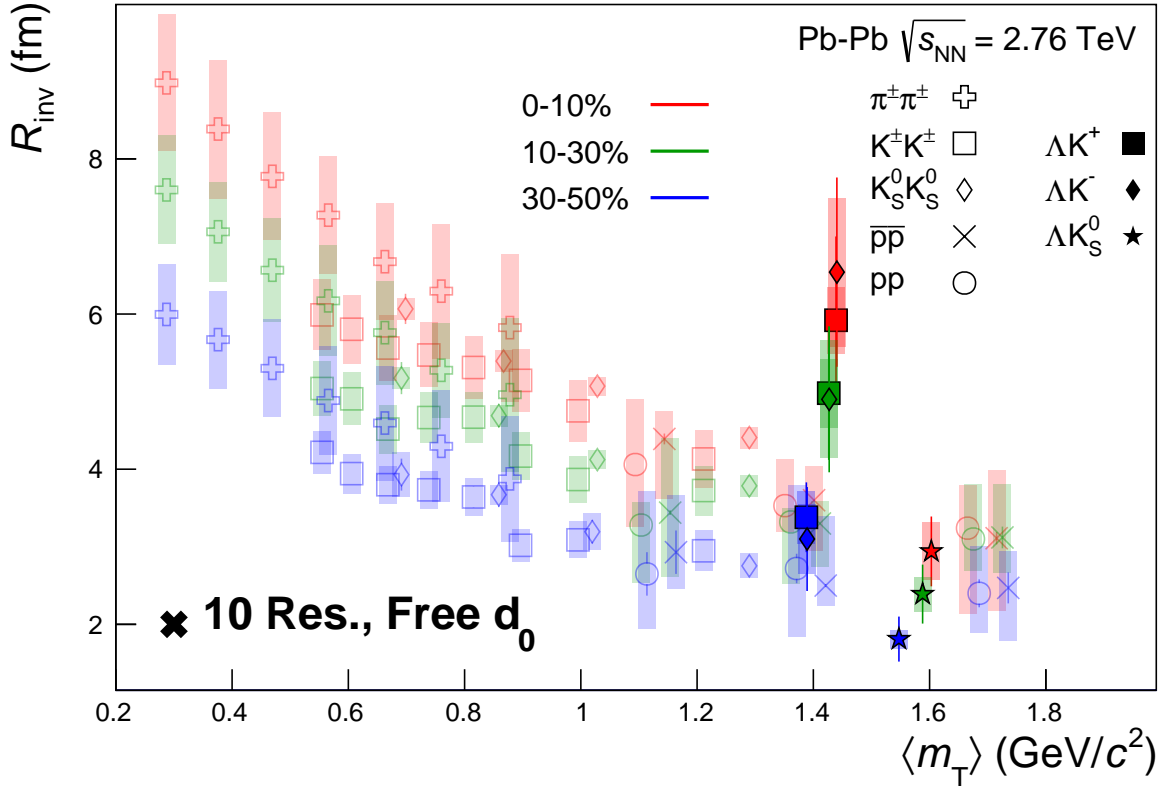
**Fig. 46:** Same as Fig. 45, but with a wider range of view. Fits, with 10 residual correlations included, to the  $\Lambda K^+$  (left) and  $\bar{\Lambda} K^-$  (right) data for the centralities 0-10% (top), 10-30% (middle), and 30-50% (bottom). The lines represent the statistical errors, while the boxes represent the systematic errors. Each has unique  $\lambda$  and normalization parameters. The radii are shared amongst like centralities; the scattering parameters ( $\mathbb{R}f_0$ ,  $\mathbb{I}f_0$ ,  $d_0$ ) are shared amongst all. The black solid line represents the “raw” fit, i.e. not corrected for momentum resolution effects nor non-flat background. The green line shows the fit to the non-flat background. The purple points show the fit after momentum resolution and non-flat background corrections have been applied. The initial values of the parameters is listed, as well as the final fit values with uncertainties.



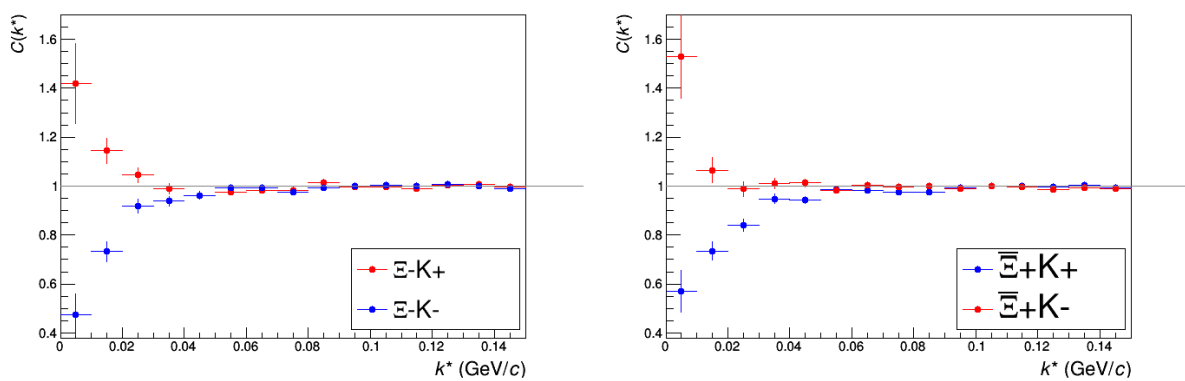
**Fig. 47:** Fits, with 10 residual correlations included, to the  $\Lambda K^-$  (left) with  $\bar{\Lambda} K^+$  (right) data for the centralities 0-10% (top), 10-30% (middle), and 30-50% (bottom). The lines represent the statistical errors, while the boxes represent the systematic errors. Each has unique  $\lambda$  and normalization parameters. The radii are shared amongst like centralities; the scattering parameters ( $\mathbb{R}f_0$ ,  $\mathbb{I}f_0$ ,  $d_0$ ) are shared amongst all. The black solid line represents the “raw” fit, i.e. not corrected for momentum resolution effects nor non-flat background. The green line shows the fit to the non-flat background. The purple points show the fit after momentum resolution and non-flat background corrections have been applied. The initial values of the parameters is listed, as well as the final fit values with uncertainties.



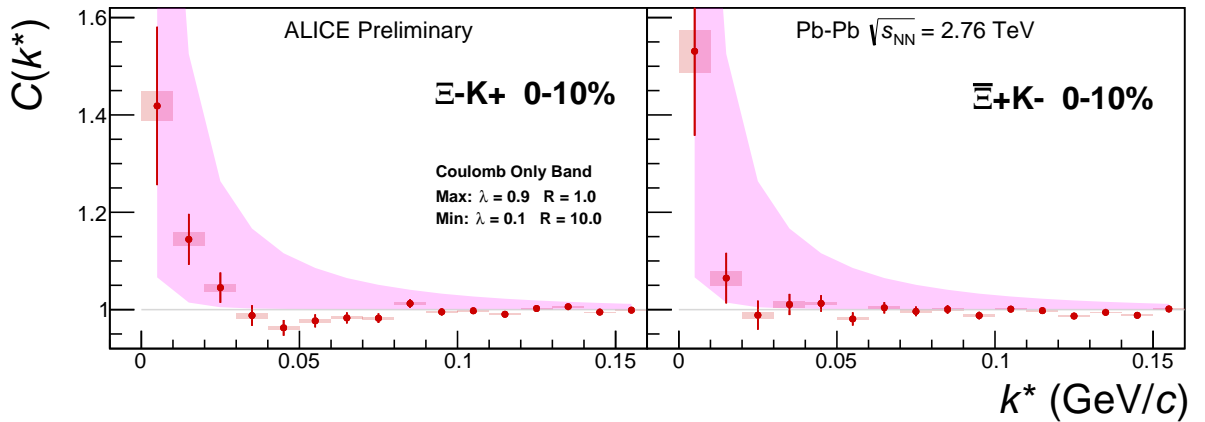
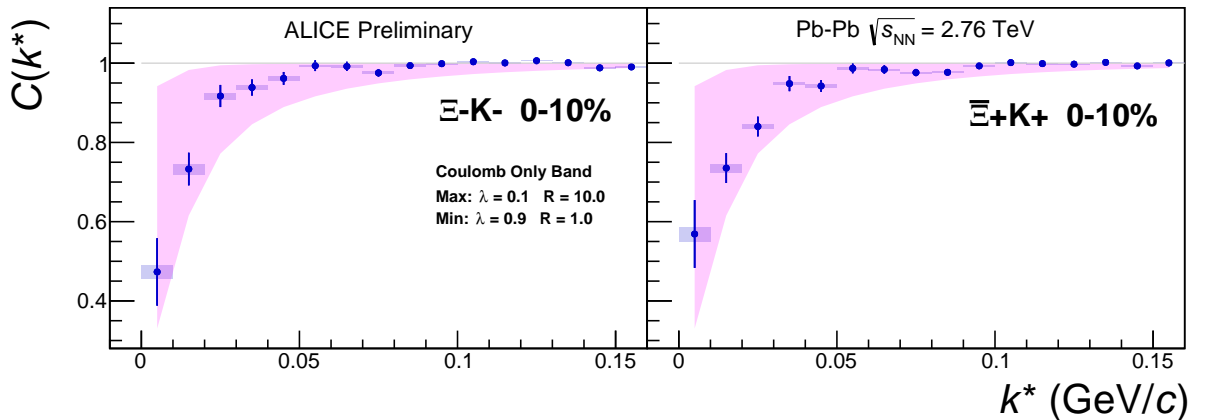
**Fig. 48:** Same as Fig. 47, but with a wider range of view. Fits, with 10 residual correlations included, to the  $\Lambda K^-$  (left) with  $\bar{\Lambda} K^+$  (right) data for the centralities 0-10% (top), 10-30% (middle), and 30-50% (bottom). The lines represent the statistical errors, while the boxes represent the systematic errors. Each has unique  $\lambda$  and normalization parameters. The radii are shared amongst like centralities; the scattering parameters ( $\mathbb{R}f_0$ ,  $\mathbb{I}f_0$ ,  $d_0$ ) are shared amongst all. The black solid line represents the “raw” fit, i.e. not corrected for momentum resolution effects nor non-flat background. The green line shows the fit to the non-flat background. The purple points show the fit after momentum resolution and non-flat background corrections have been applied. The initial values of the parameters is listed, as well as the final fit values with uncertainties.



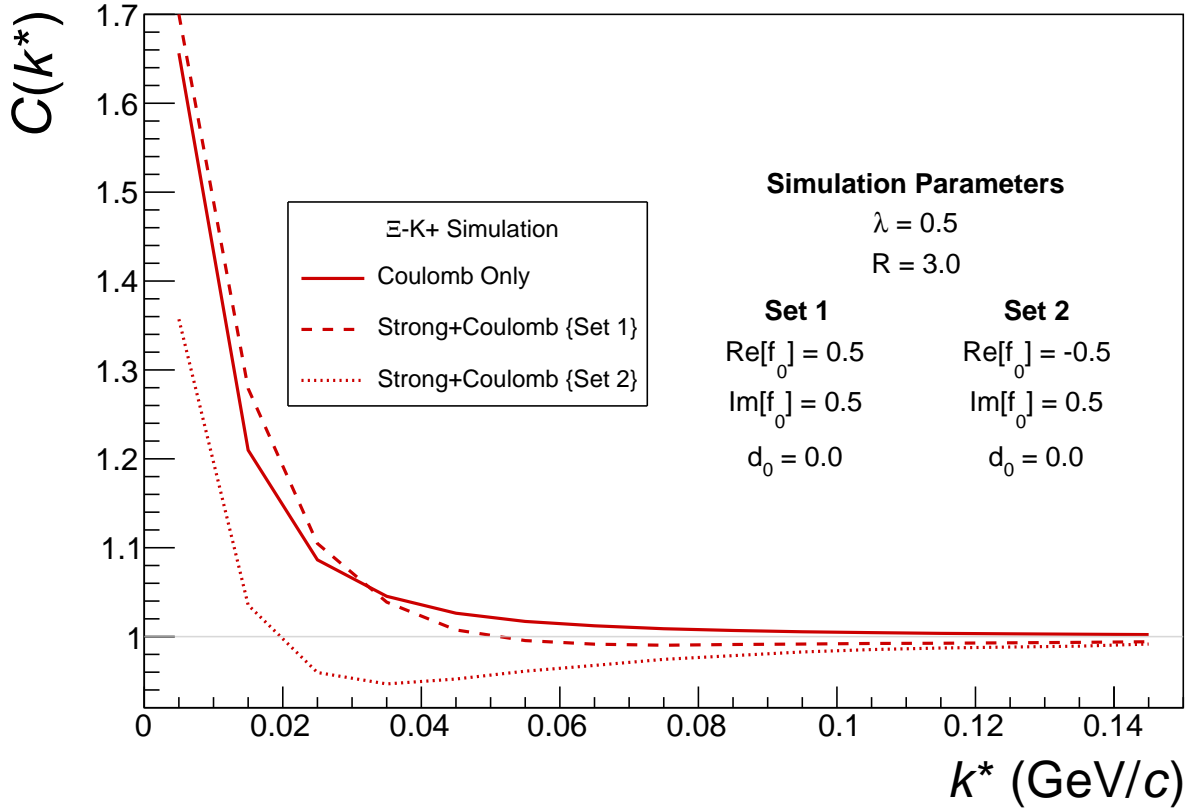
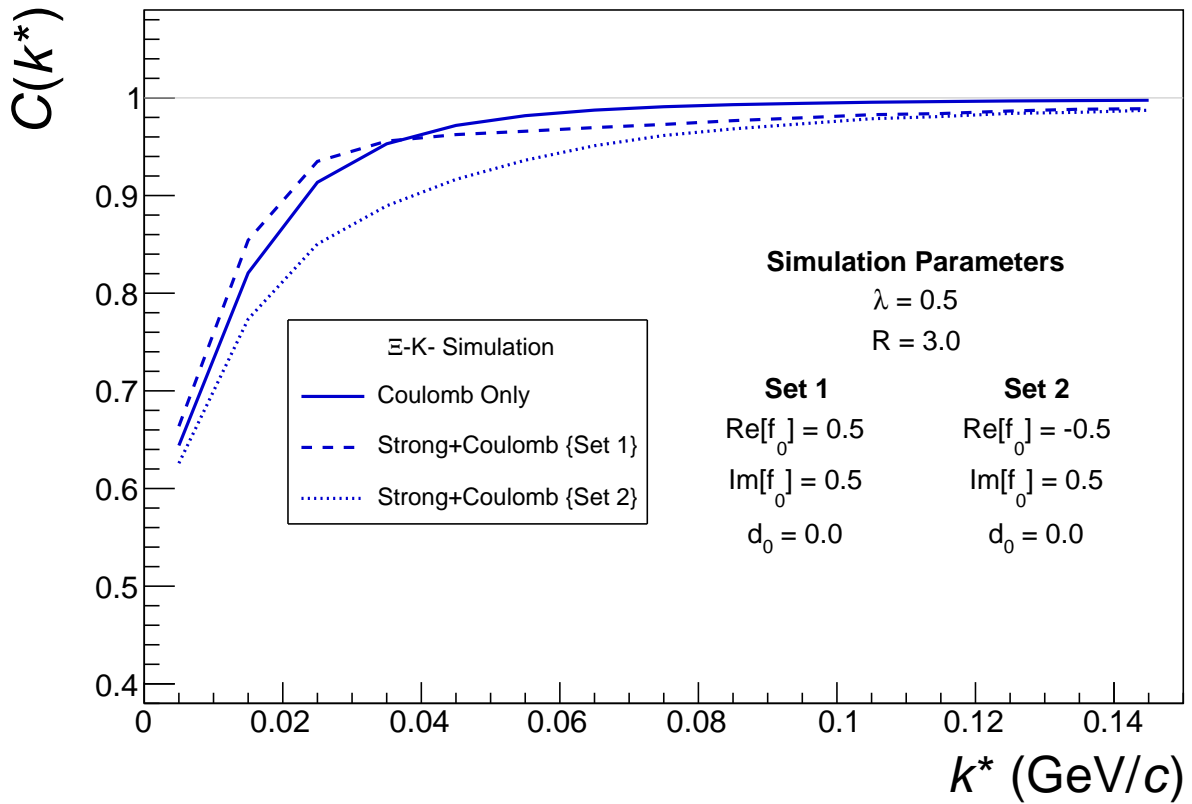
**Fig. 49:** 10 residual correlations in  $\Lambda K$  fits. Extracted fit  $R_{\text{inv}}$  parameters as a function of pair transverse mass ( $m_T$ ) for various pair systems over several centralities. The ALICE published data [10] is shown with transparent, open symbols. The new  $\Lambda K$  results are shown with opaque, filled symbols. In the left, the  $\Lambda K^+$  (with its conjugate pair) results are shown separately from the  $\Lambda K^-$  (with its conjugate pair) results. In the right, all  $\Lambda K^\pm$  results are averaged.



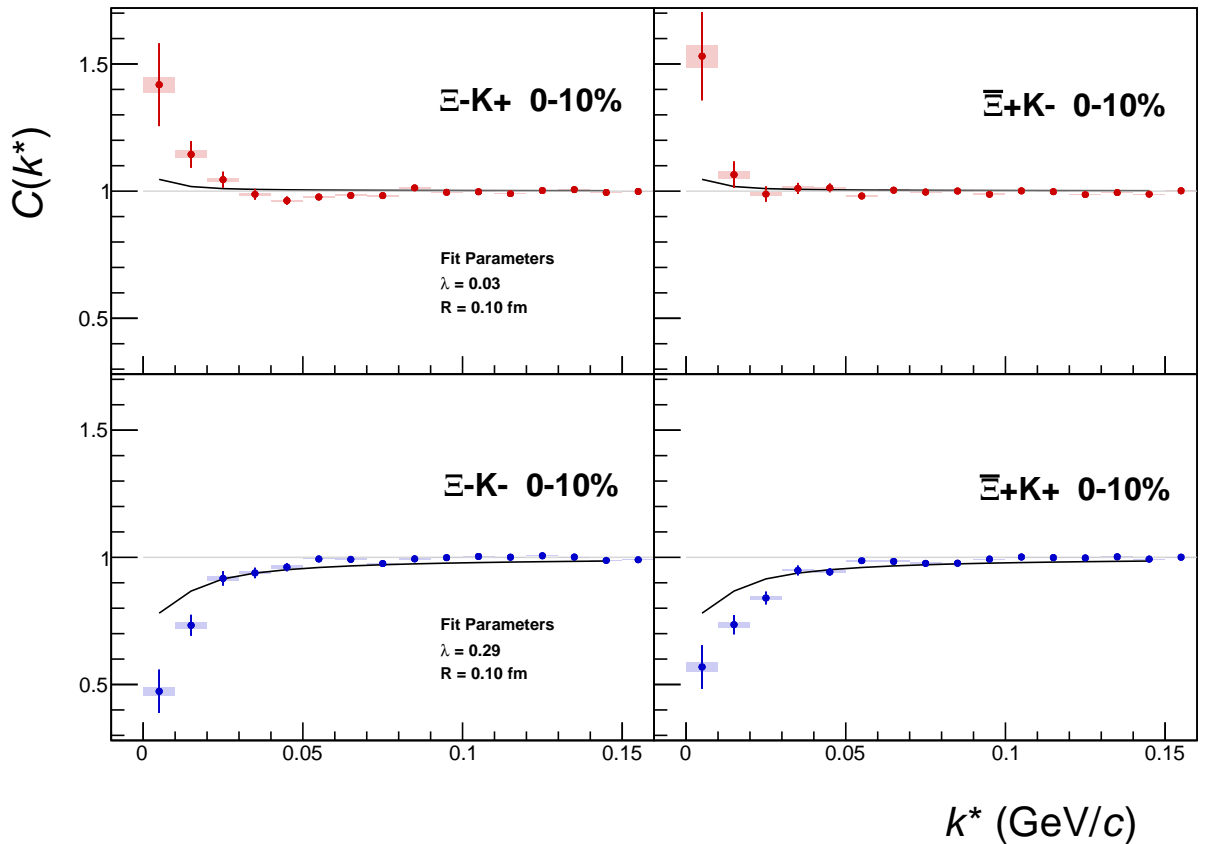
**Fig. 50:**  $\Sigma K^\pm$  Results for 0-10% Centrality. (Left)  $\Sigma^- K^+$  and  $\Sigma^- K^-$  (Right)  $\Sigma^+ K^+$  and  $\Sigma^+ K^-$


 (a) (Left)  $\Xi\text{K}^+$  and (Right)  $\bar{\Xi}\text{K}^-$ 

 (b) (Left)  $\Xi\text{K}^-$  and (Right)  $\bar{\Xi}\text{K}^+$ 

**Fig. 51:**  $\Xi\text{K}^\pm$  data with Coulomb-only bands for the 0-10% centrality bin. The Coulomb-only bands span two sets of Coulomb-only curves: (1)  $\lambda = 0.9$ , R = 1.0 fm and (2)  $\lambda = 0.1$ , R = 10.0 fm. The Coulomb-only curves are simulated correlation functions for the respective pair system assuming only a Coulomb interaction, i.e. ignoring the strong interaction. The Coulomb-only curves change monotonically with varying  $\lambda$  and varying R, therefore, any intermediate parameter set will fall within this Coulomb-only band.

(a)  $\Xi K^+$  and  $\bar{\Xi} K^-$  simulation(b)  $\Xi K^-$  and  $\bar{\Xi} K^+$  simulation

**Fig. 52:** Effect on the Coulomb-only curve of including the strong interaction for  $\Xi K^\pm$  systems. The solid line represents a Coulomb-only curve, i.e. a simulated correlation function with the strong interaction turned off. The dashed lines represent a full simulation, including both the strong and Coulomb interactions. The two dashed lines differ only in the real part of the assumed scattering length: positive in Set 1, and negative in Set 2.



**Fig. 53:**  $\Xi K^\pm$  Global Coulomb-only fit (Set 1) for 0-10% centrality. In this fit, there was a lower limit of 0.1 fm placed on the radius parameter, and the radius parameter was initialized to 3 fm (as seems reasonable, when considering the transverse mass of the system and looking at Fig. 49). As is shown in the results, the radius parameter reached this unrealistic lower bound of 0.1 fm. Also, the extracted  $\lambda$  parameters are too low.

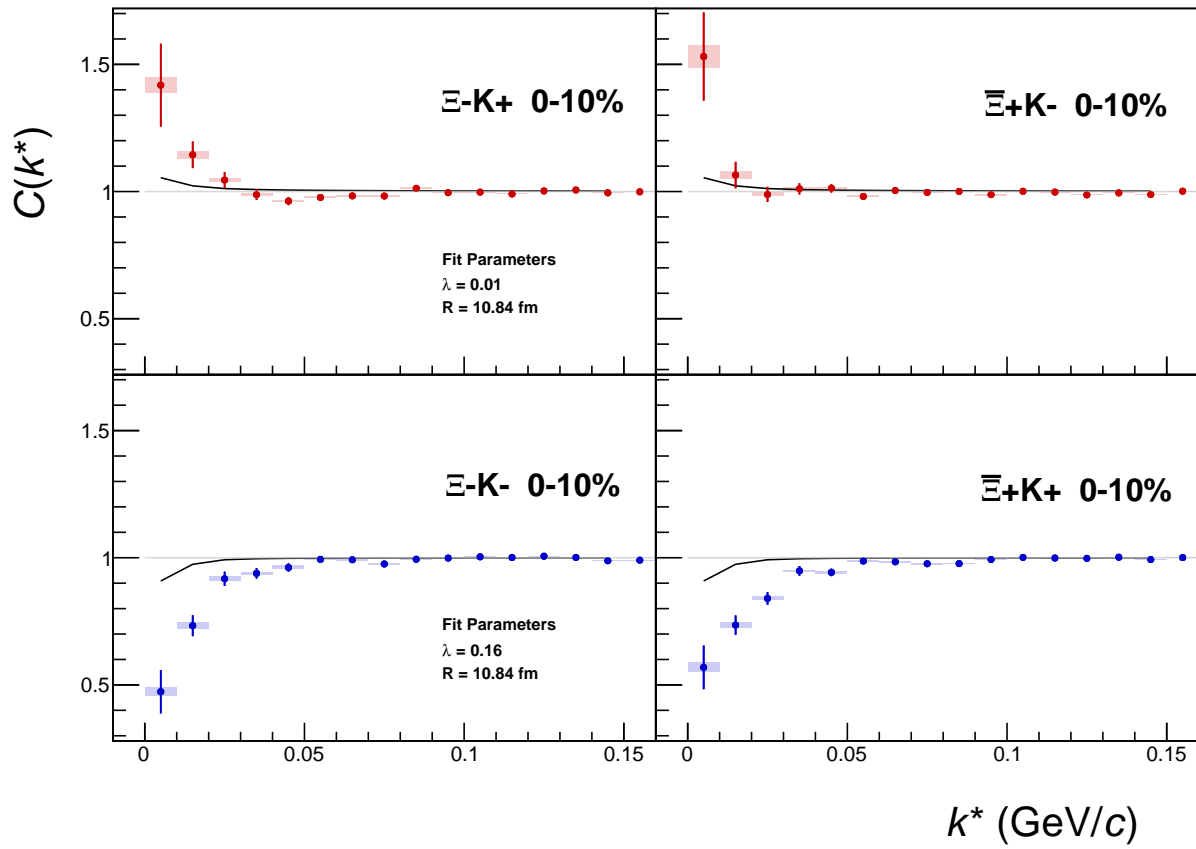


**Fig. 54:**  $\Xi K^\pm$  Global Coulomb-only fit (Set 2) for 0-10% centrality. In this fit, the parameters were all unbounded, and the radius parameter was initialized to 10 fm. In this case, the radius parameters remain high, and ends at an unrealistic value of 10.84 fm. Also, the extracted  $\lambda$  parameters are too low.

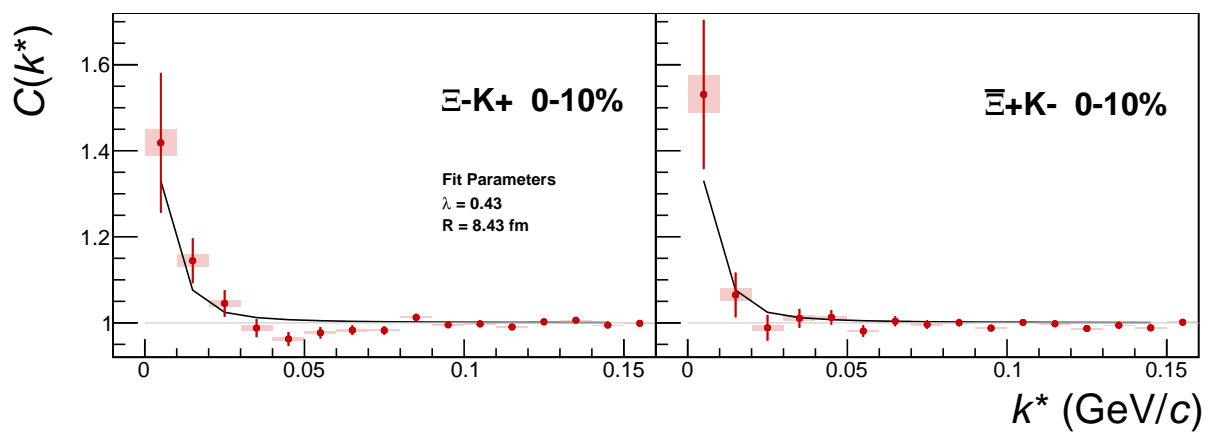


**Fig. 55:**  $\Xi\text{-}K^+$  Coulomb-only fit for 0-10% centrality

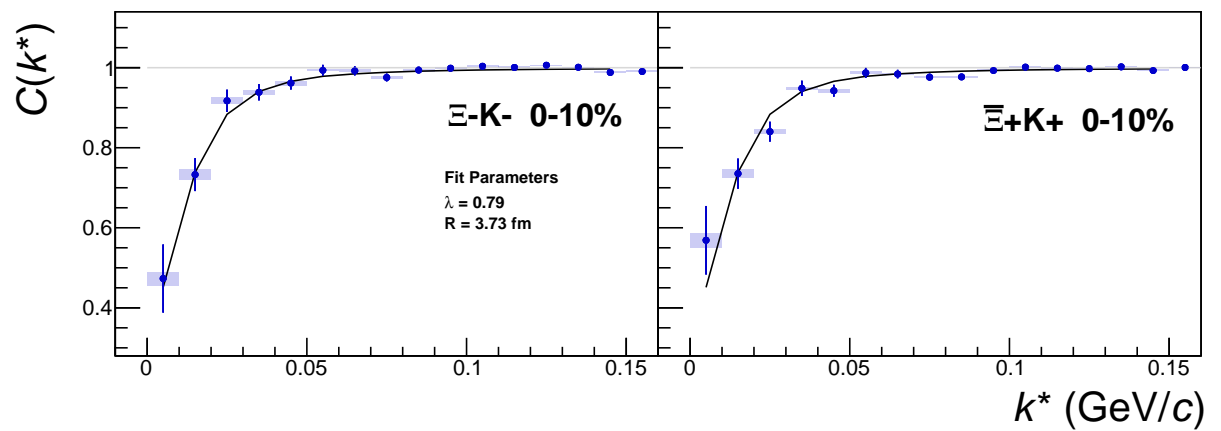
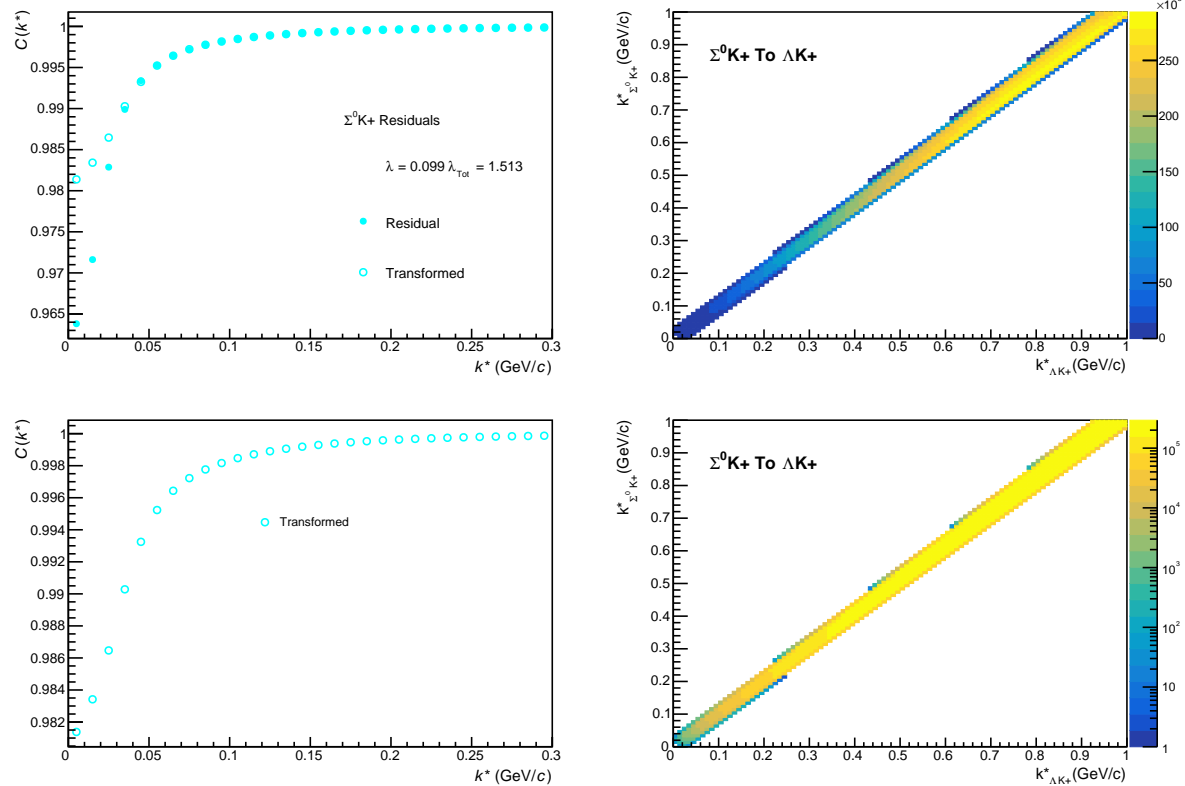


**Fig. 56:**  $\Xi^-$ K $^-$  Coulomb-only fit for 0-10% centrality

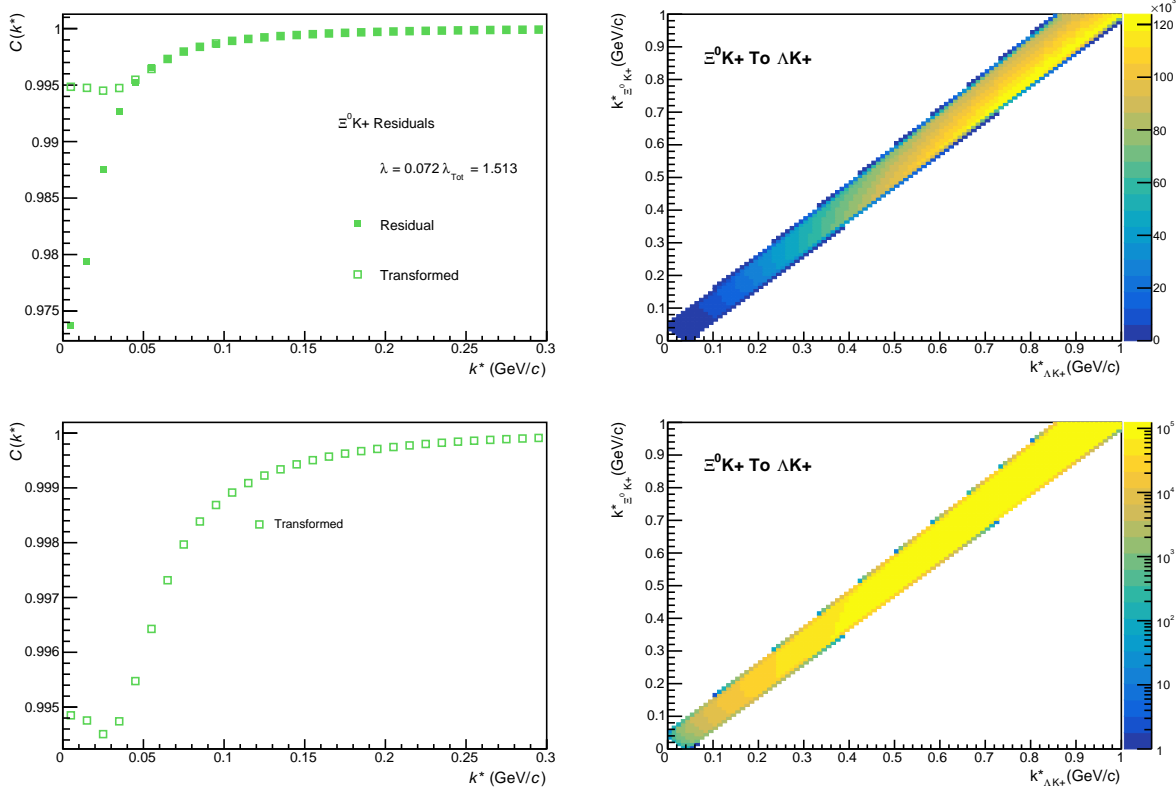
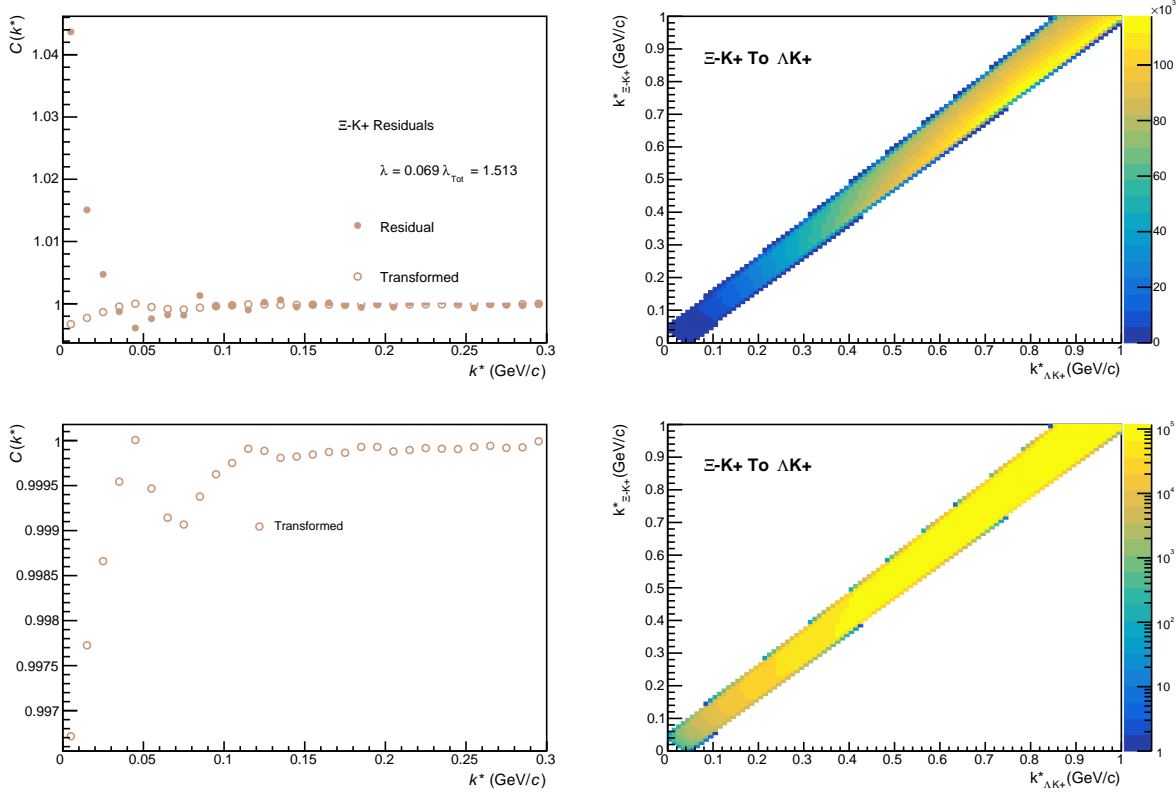
679 **9 Additional Figures**

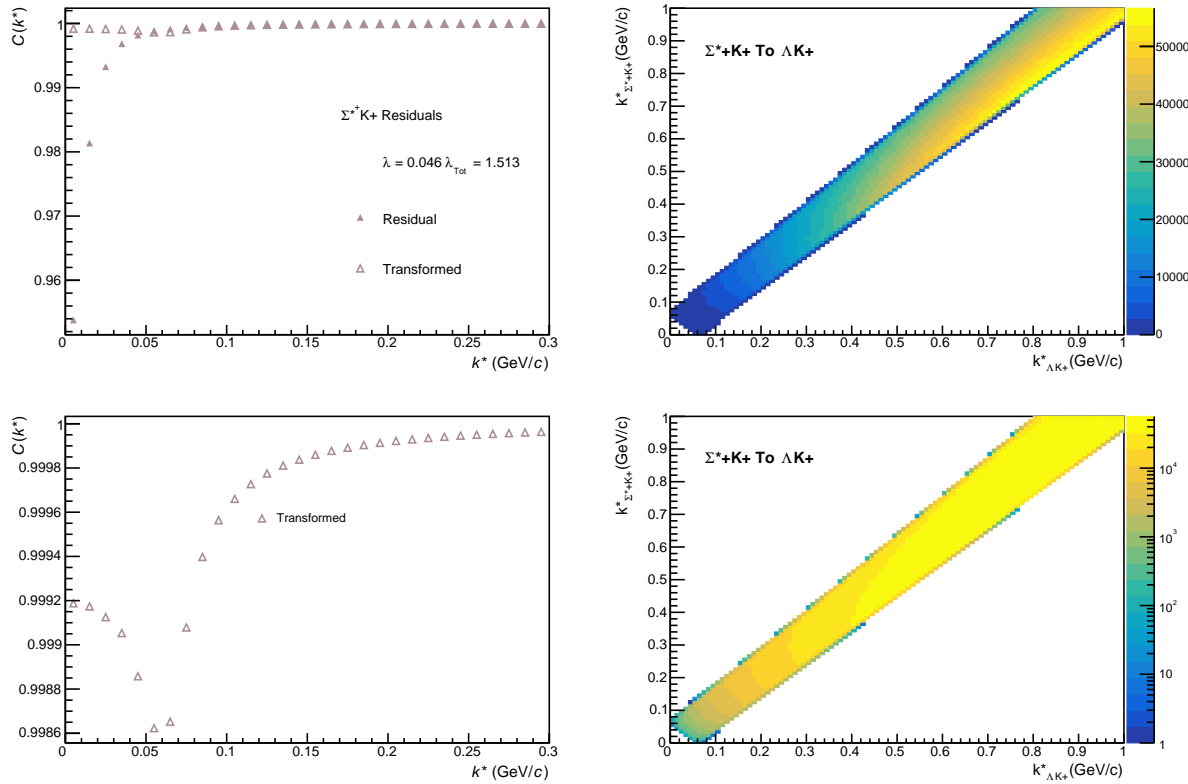
680 **9.1 Residuals**

681 **9.1.1  $\Lambda K^+$  Residuals**

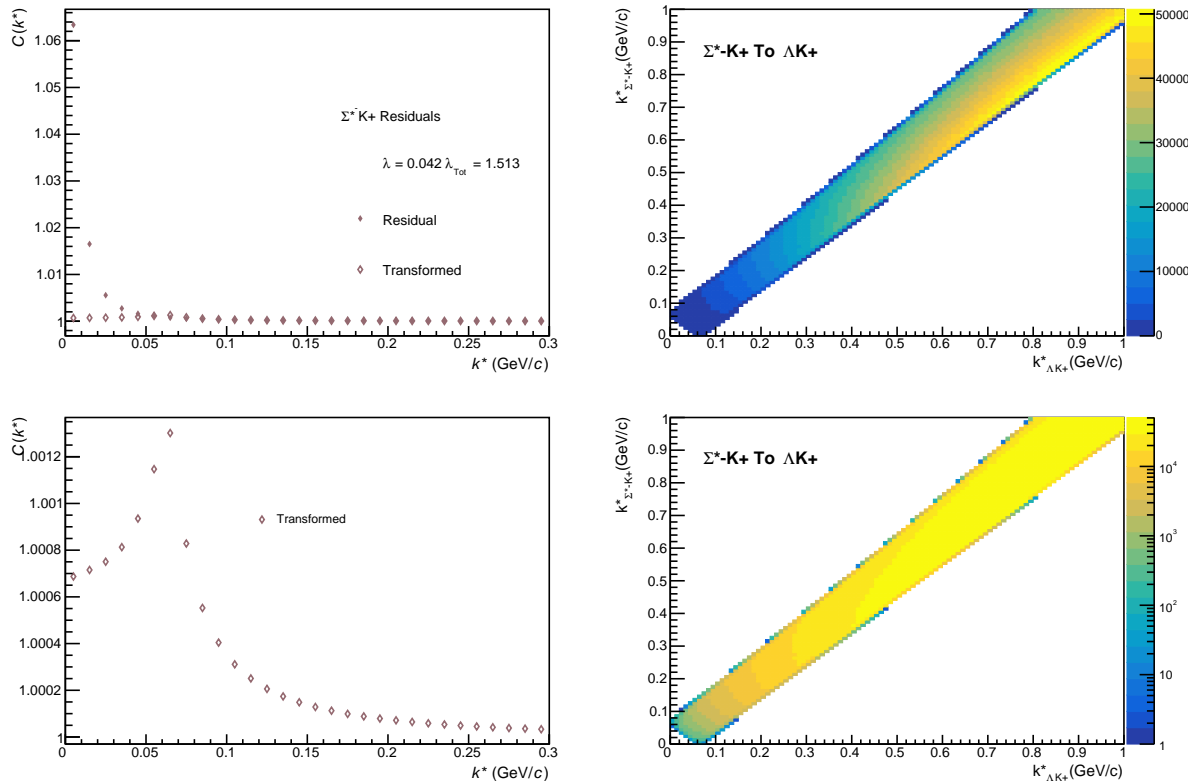


**Fig. 57:** Residuals:  $\Sigma^0 K^+$  to  $\Lambda K^+$  (0-10% Centrality)

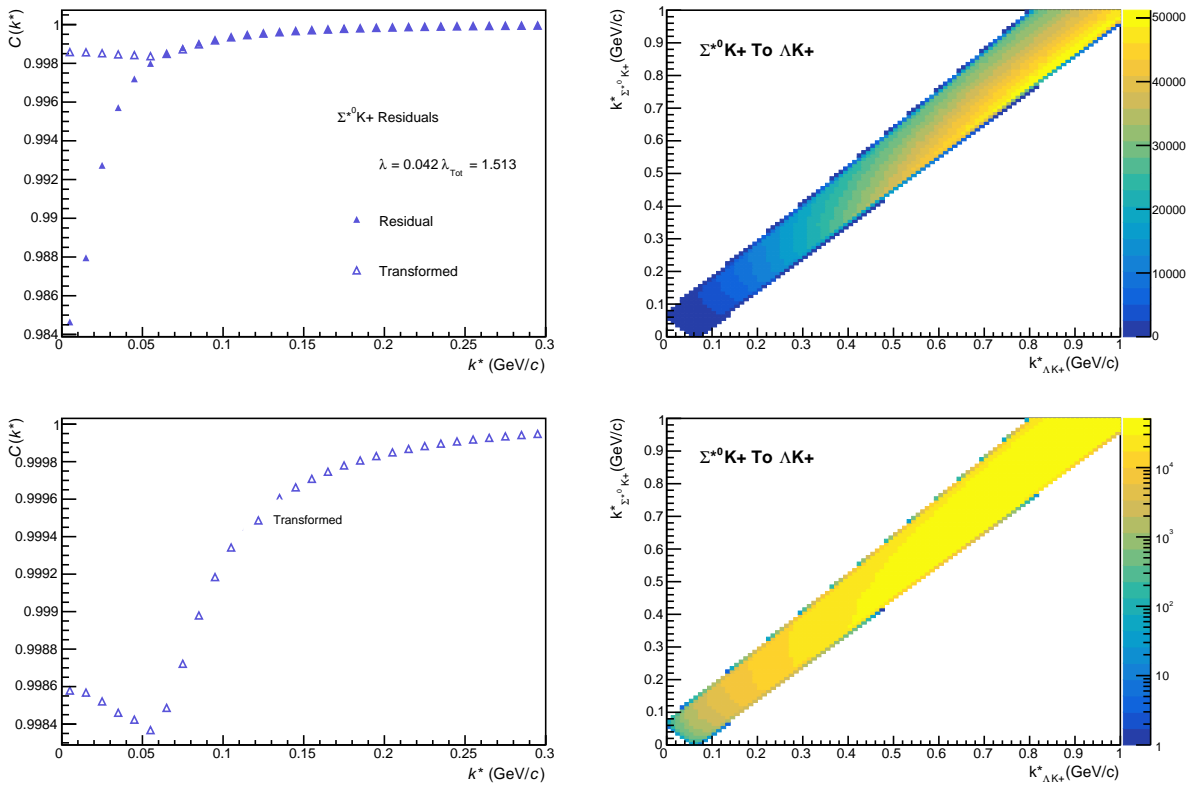
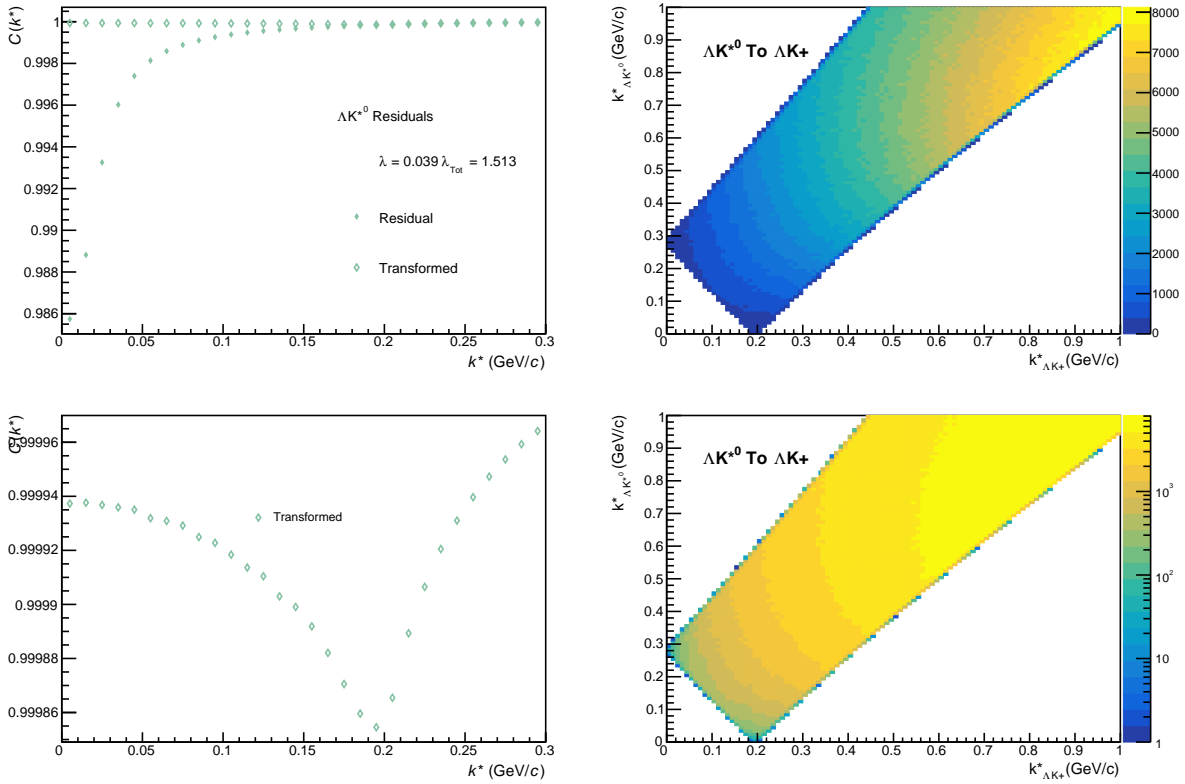

**Fig. 58:** Residuals:  $\Xi^0 \text{K}^+$  to  $\Lambda \text{K}^+$  (0-10% Centrality)

**Fig. 59:** Residuals:  $\Xi^- \text{K}^+$  to  $\Lambda \text{K}^+$  (0-10% Centrality)

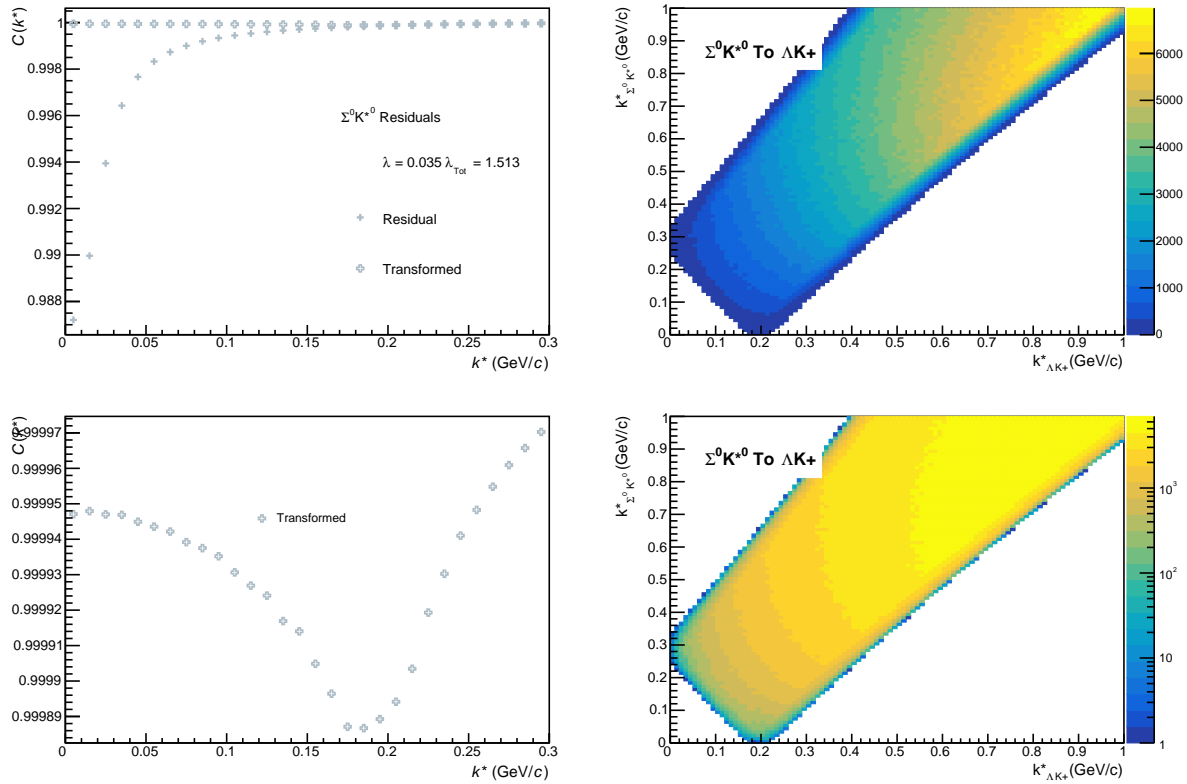


**Fig. 60:** Residuals:  $\Sigma^+ K^+$  to  $\Lambda K^+$  (0-10% Centrality)

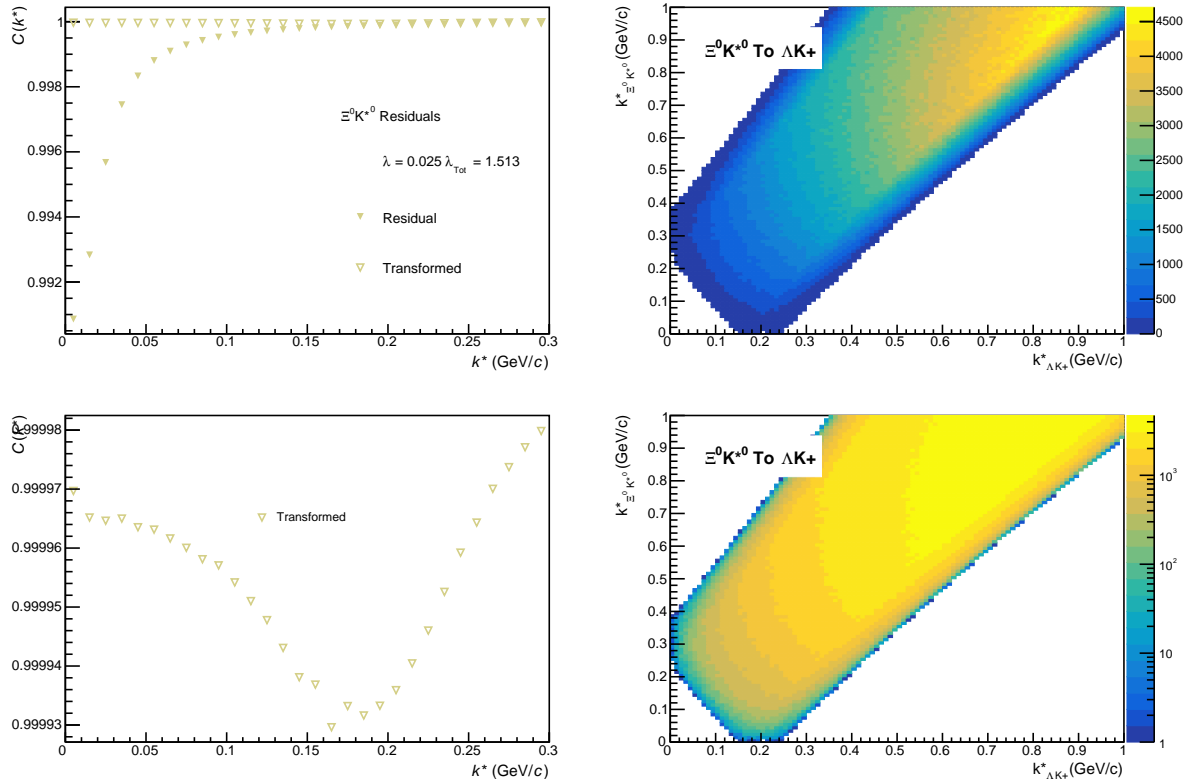


**Fig. 61:** Residuals:  $\Sigma^- K^+$  to  $\Lambda K^+$  (0-10% Centrality)

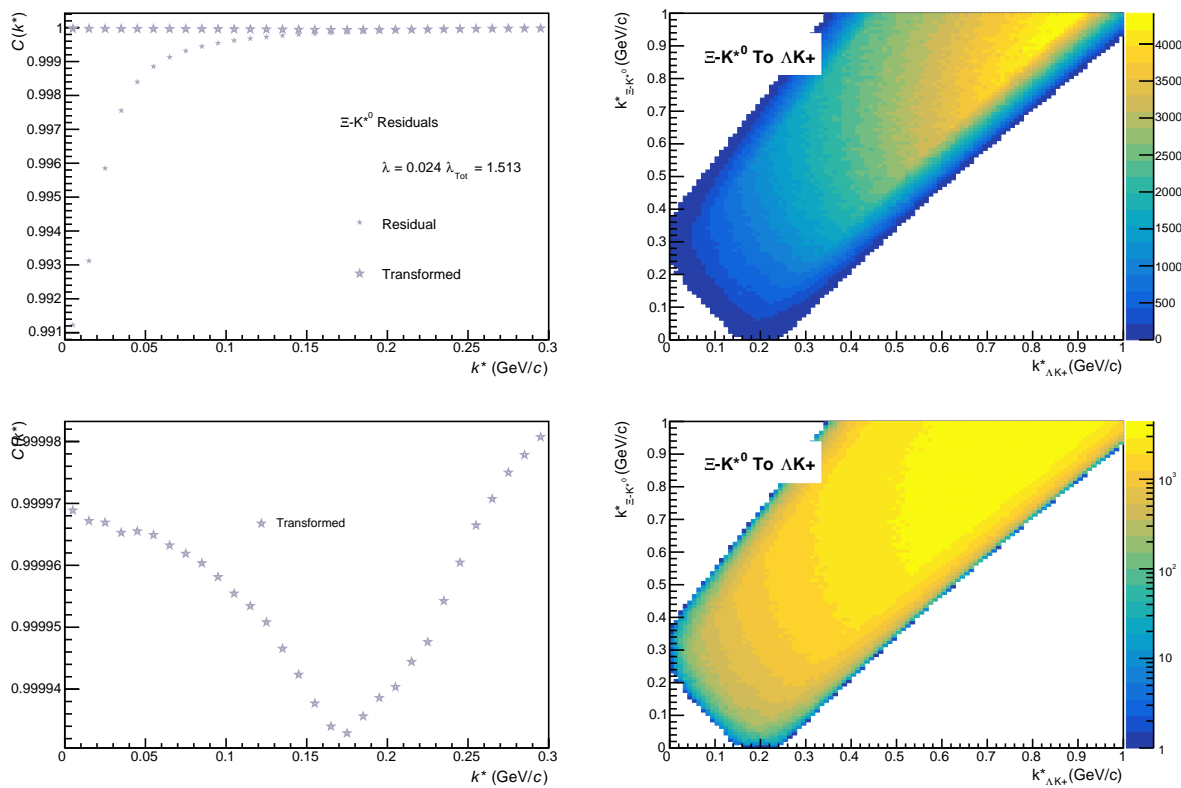

**Fig. 62:** Residuals:  $\Sigma^{*0} \text{K}^+$  to  $\Lambda \text{K}^+$  (0-10% Centrality)

**Fig. 63:** Residuals:  $\Lambda \text{K}^{*0}$  to  $\Lambda \text{K}^+$  (0-10% Centrality)



**Fig. 64:** Residuals:  $\Sigma^0 K^{*0}$  to  $\Lambda K^+$  (0-10% Centrality)

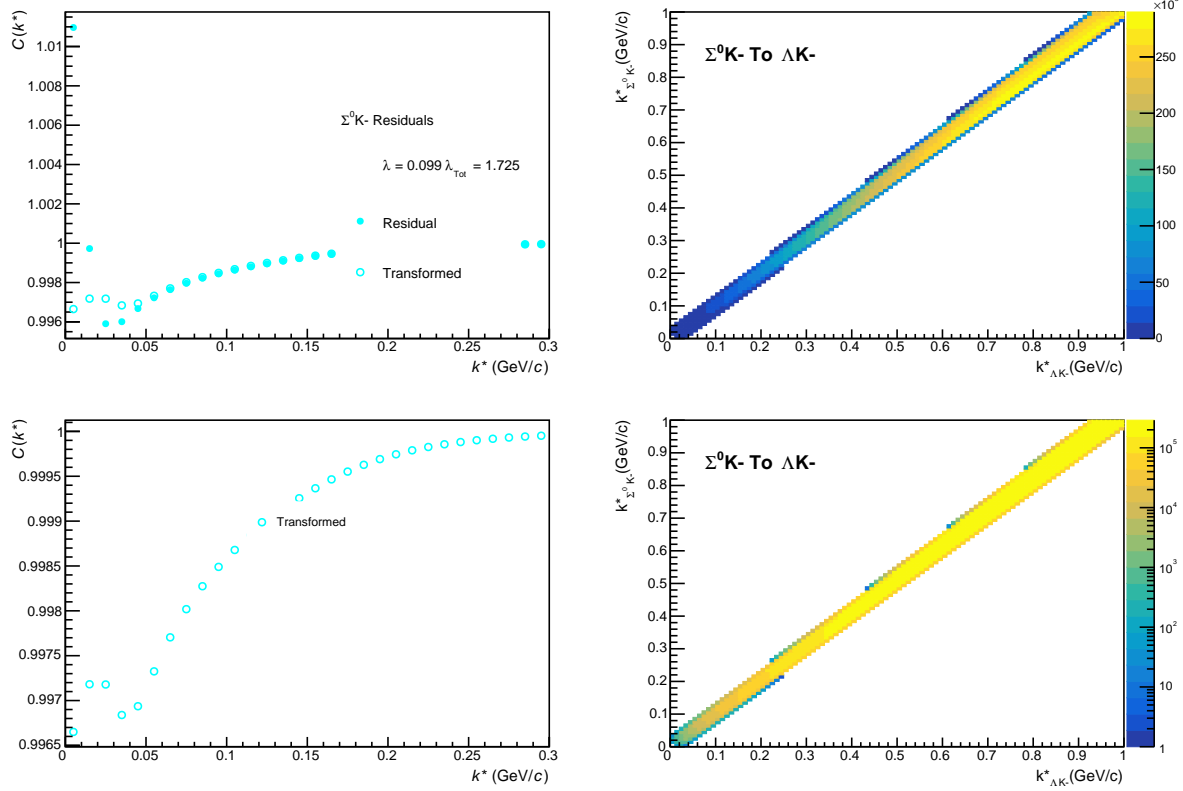


**Fig. 65:** Residuals:  $\Xi^0 K^{*0}$  to  $\Lambda K^+$  (0-10% Centrality)

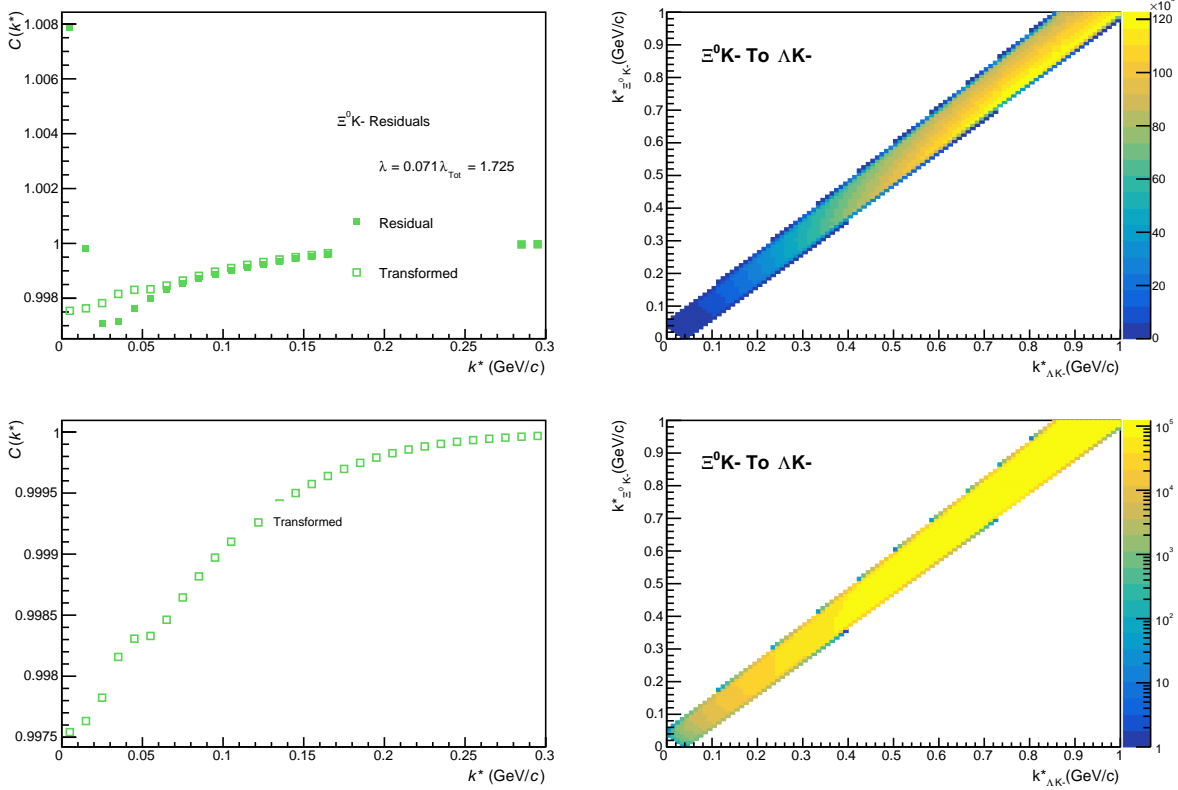
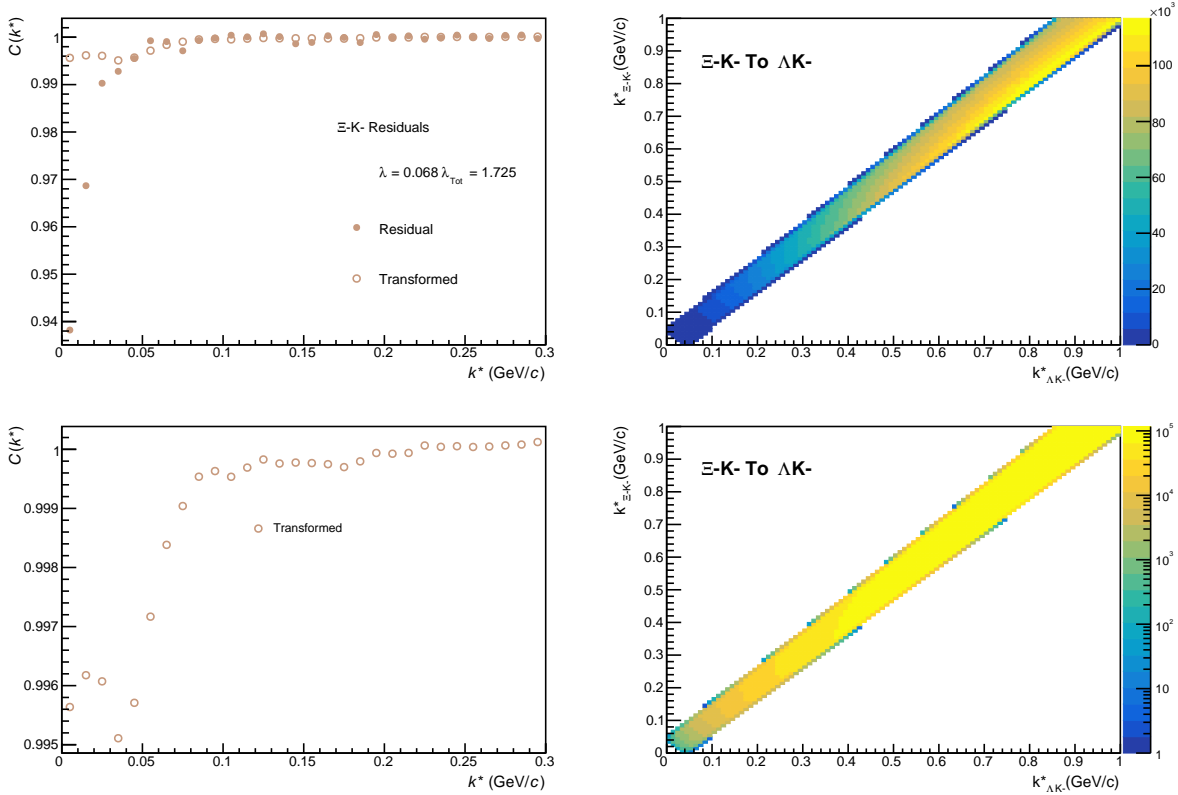


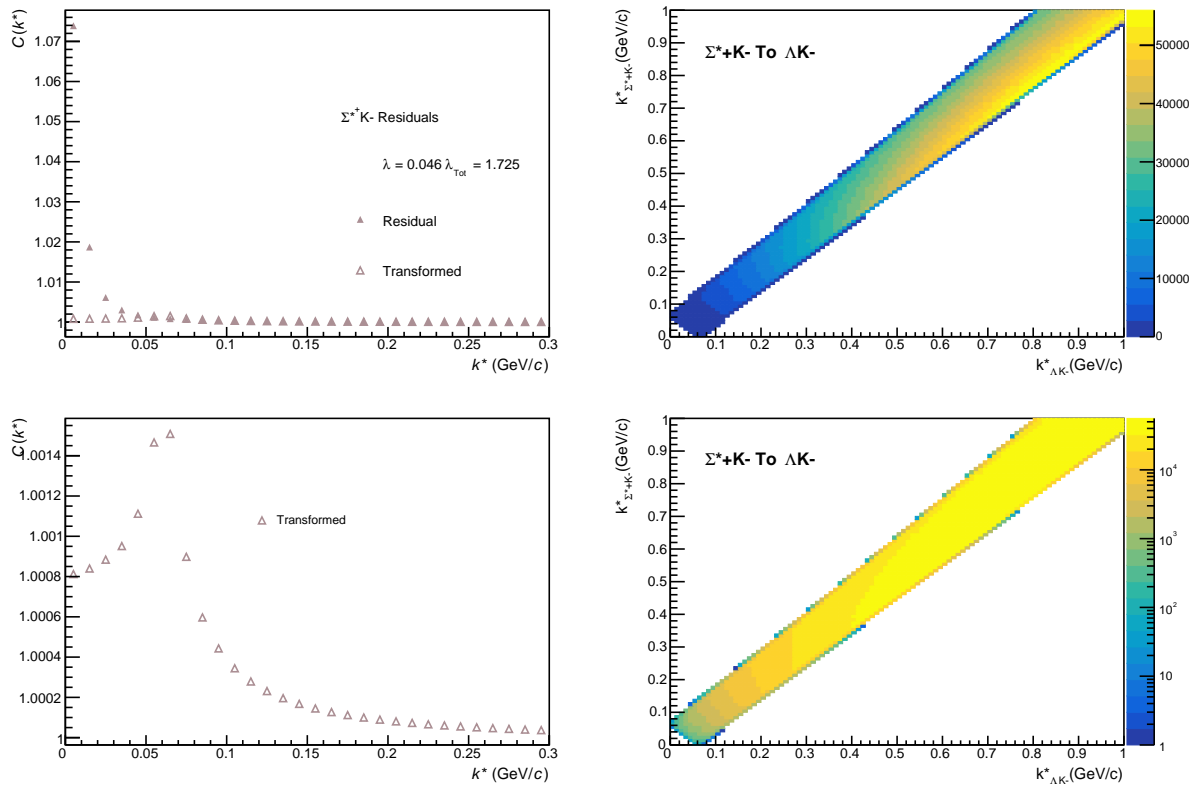
**Fig. 66:** Residuals:  $\Xi\text{-}K^{*0}$  to  $\Lambda\text{K}^+$  (0-10% Centrality)

682 **9.1.2  $\Lambda K^-$  Residuals**

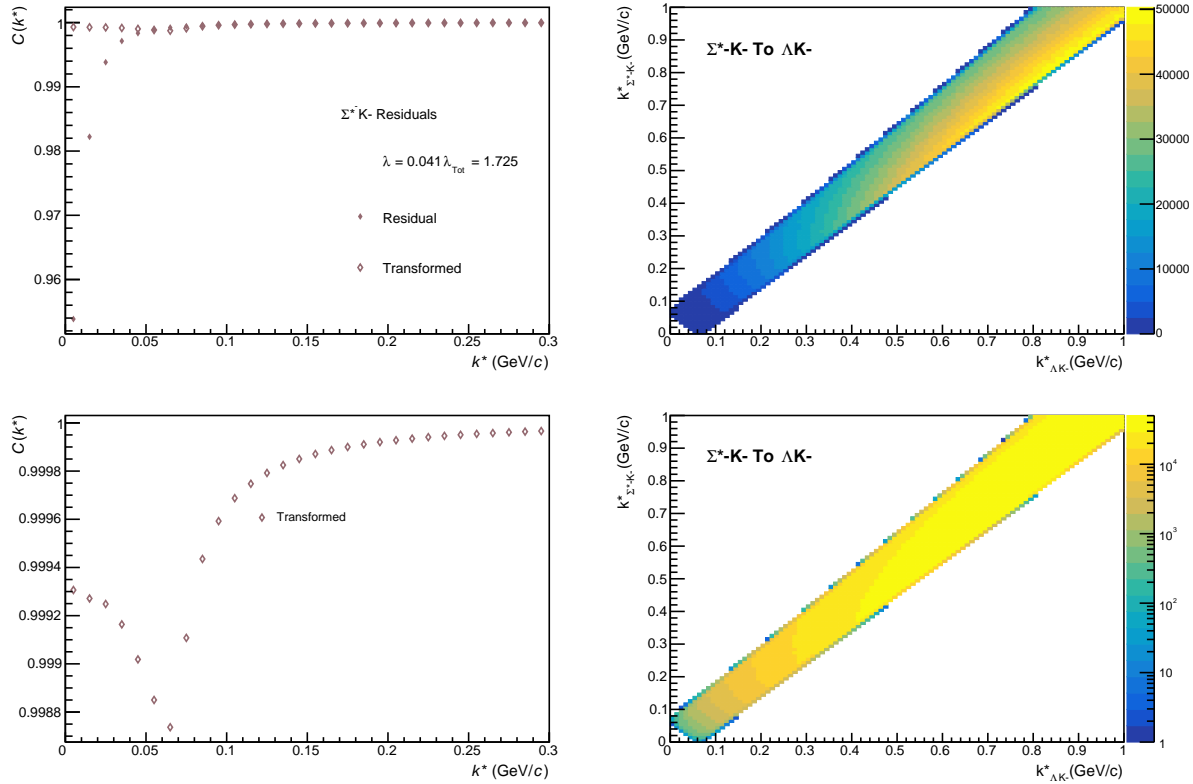


**Fig. 67:** Residuals:  $\Sigma^0 K^-$  to  $\Lambda K^-$  (0-10% Centrality)

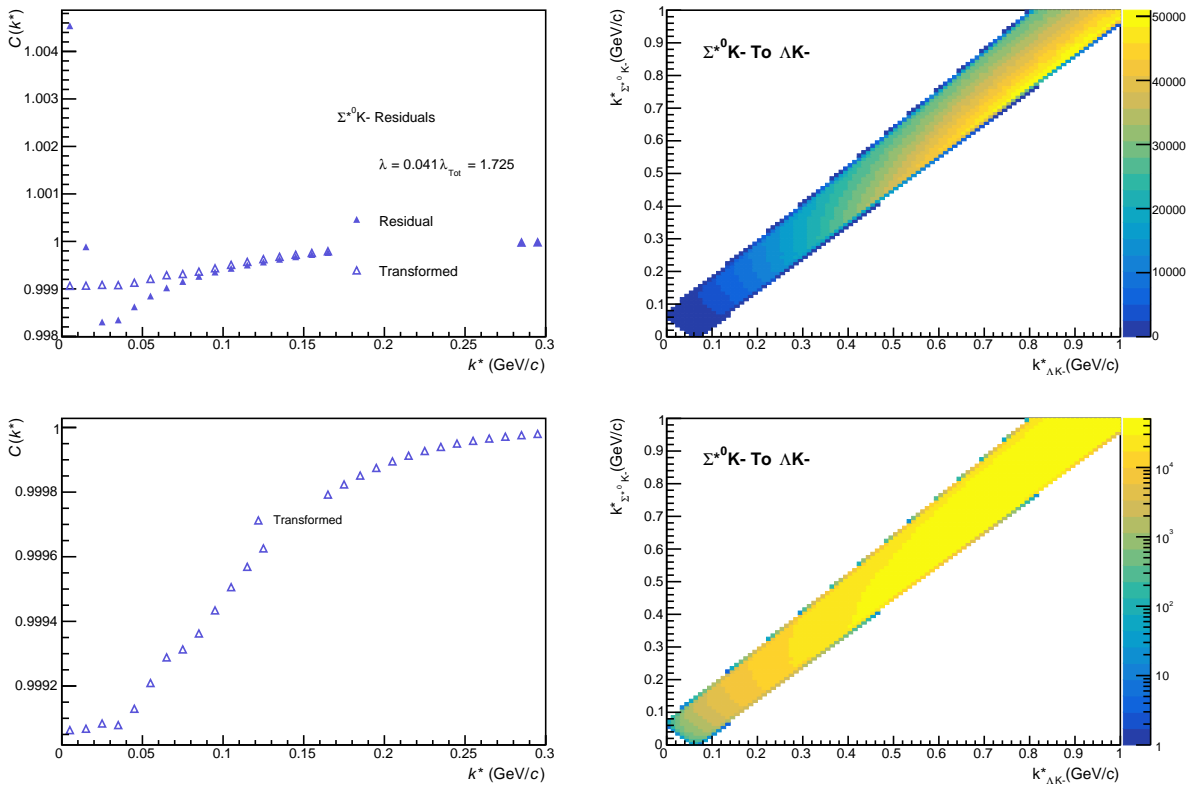
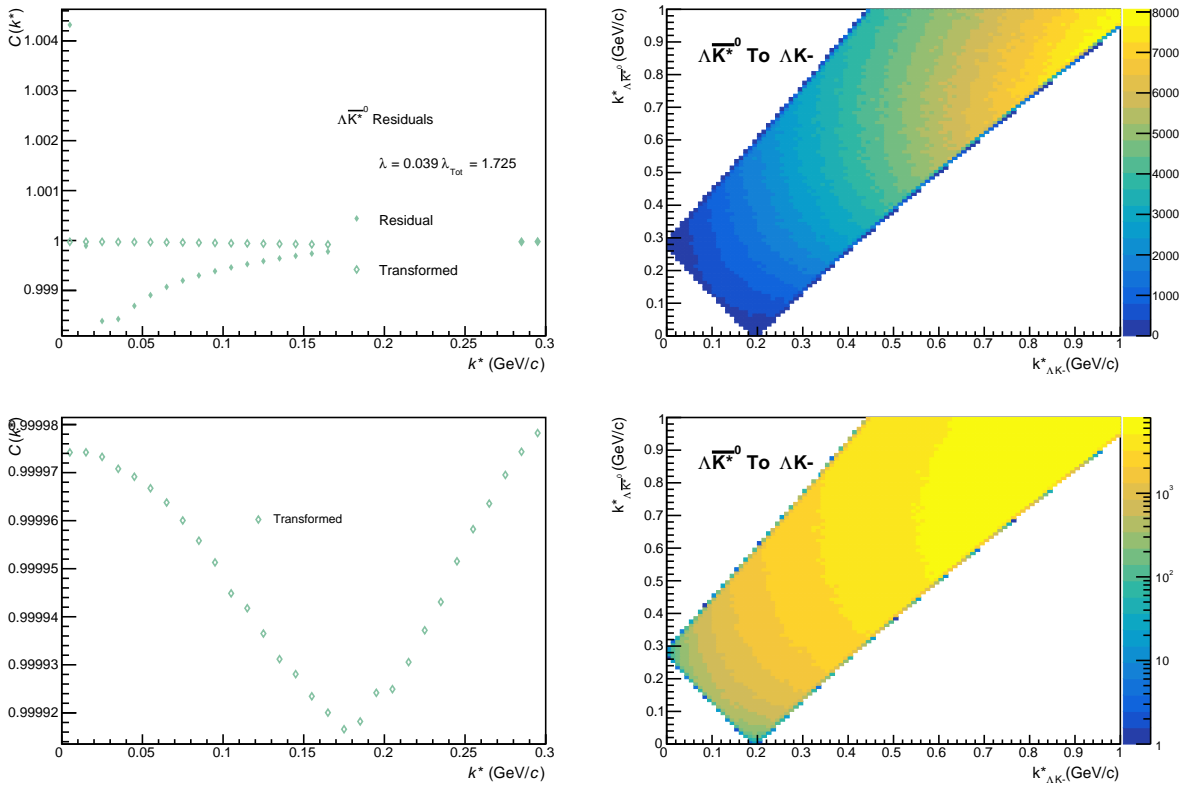

**Fig. 68:** Residuals:  $\Xi^0 \text{K}^-$  to  $\Lambda \text{K}^-$  (0-10% Centrality)

**Fig. 69:** Residuals:  $\Xi^- \text{K}^-$  to  $\Lambda \text{K}^-$  (0-10% Centrality)

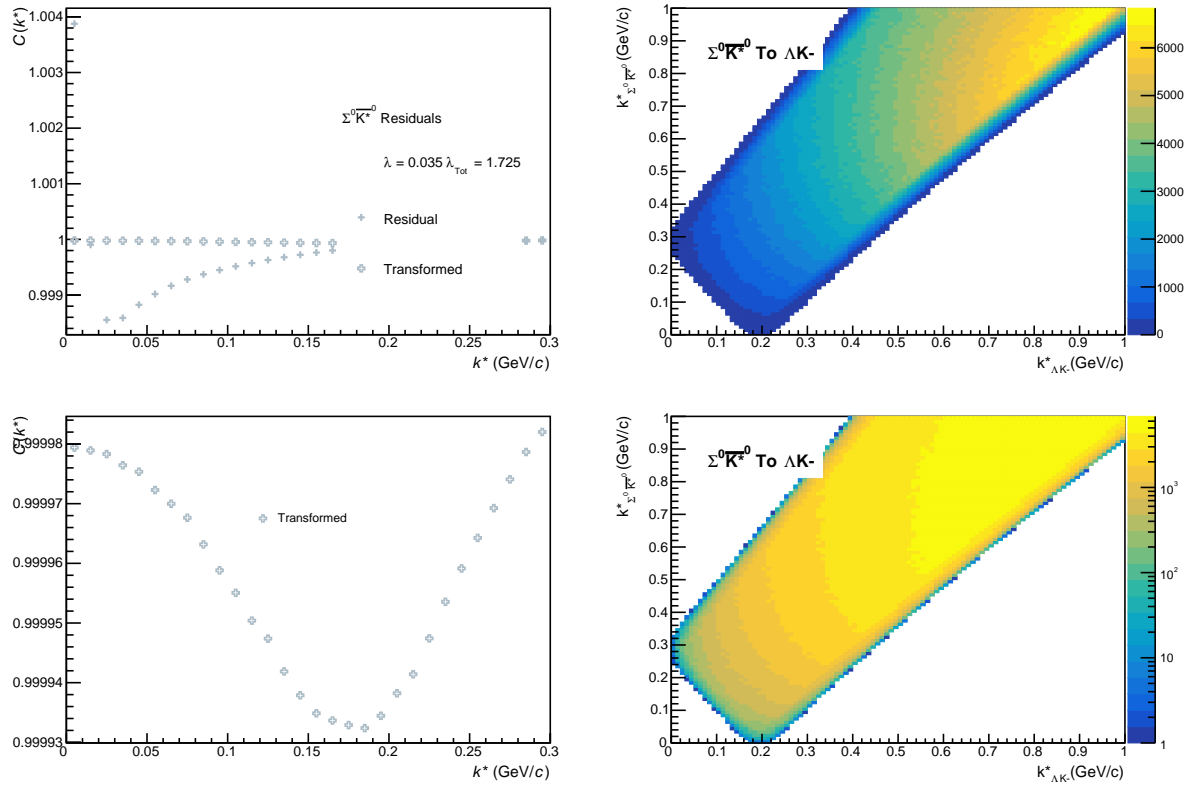


**Fig. 70:** Residuals:  $\Sigma^+ K^-$  to  $\Lambda K^-$  (0-10% Centrality)

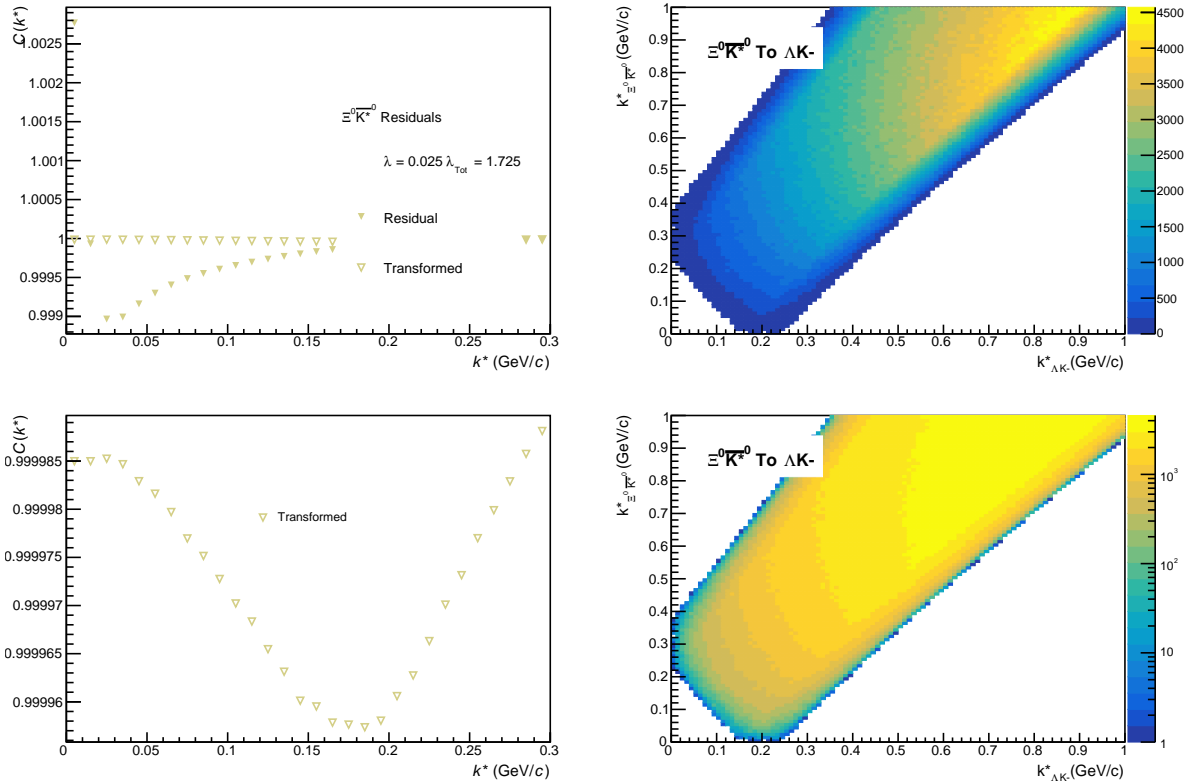


**Fig. 71:** Residuals:  $\Sigma^- K^-$  to  $\Lambda K^-$  (0-10% Centrality)

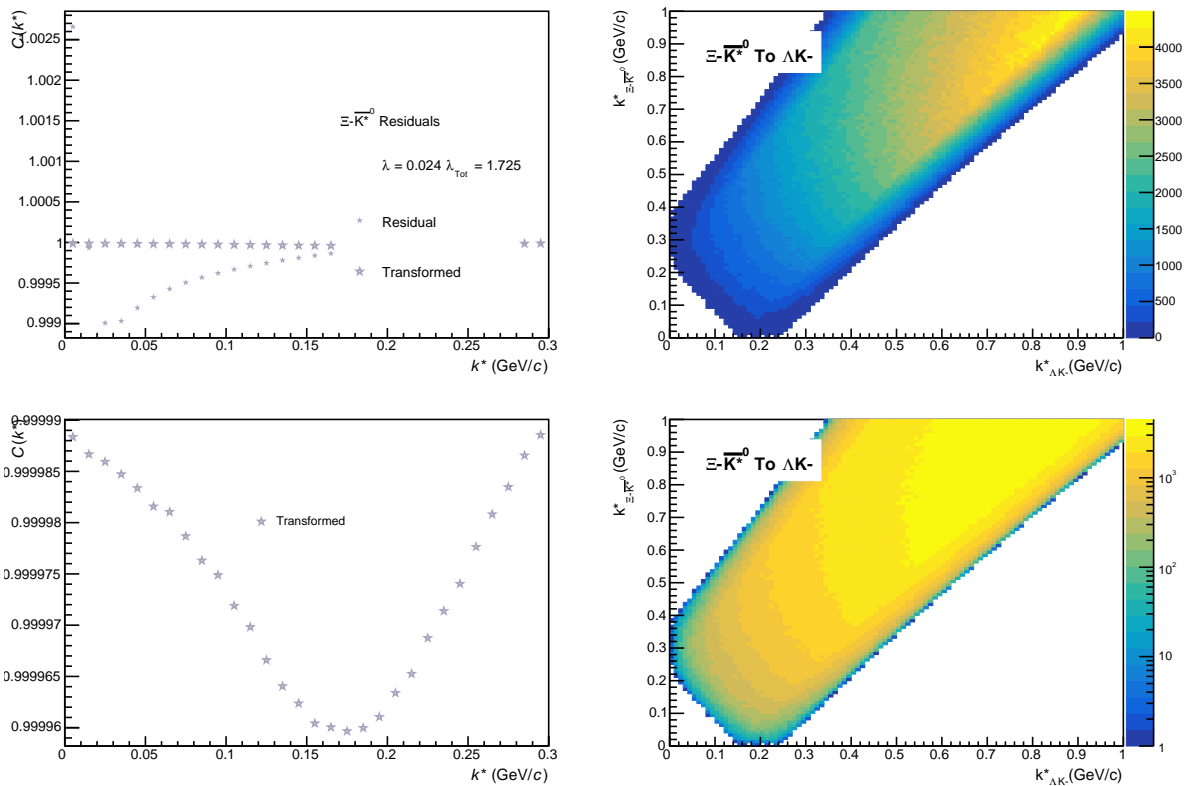

 Fig. 72: Residuals:  $\Sigma^{*0} \text{K-}$  to  $\Lambda \text{K-}$  (0-10% Centrality)

 Fig. 73: Residuals:  $\Lambda \bar{K}^{*0}$  to  $\Lambda \text{K-}$  (0-10% Centrality)



**Fig. 74:** Residuals:  $\Sigma^0 \bar{K}^{*0}$  to  $\Lambda K^-$  (0-10% Centrality)

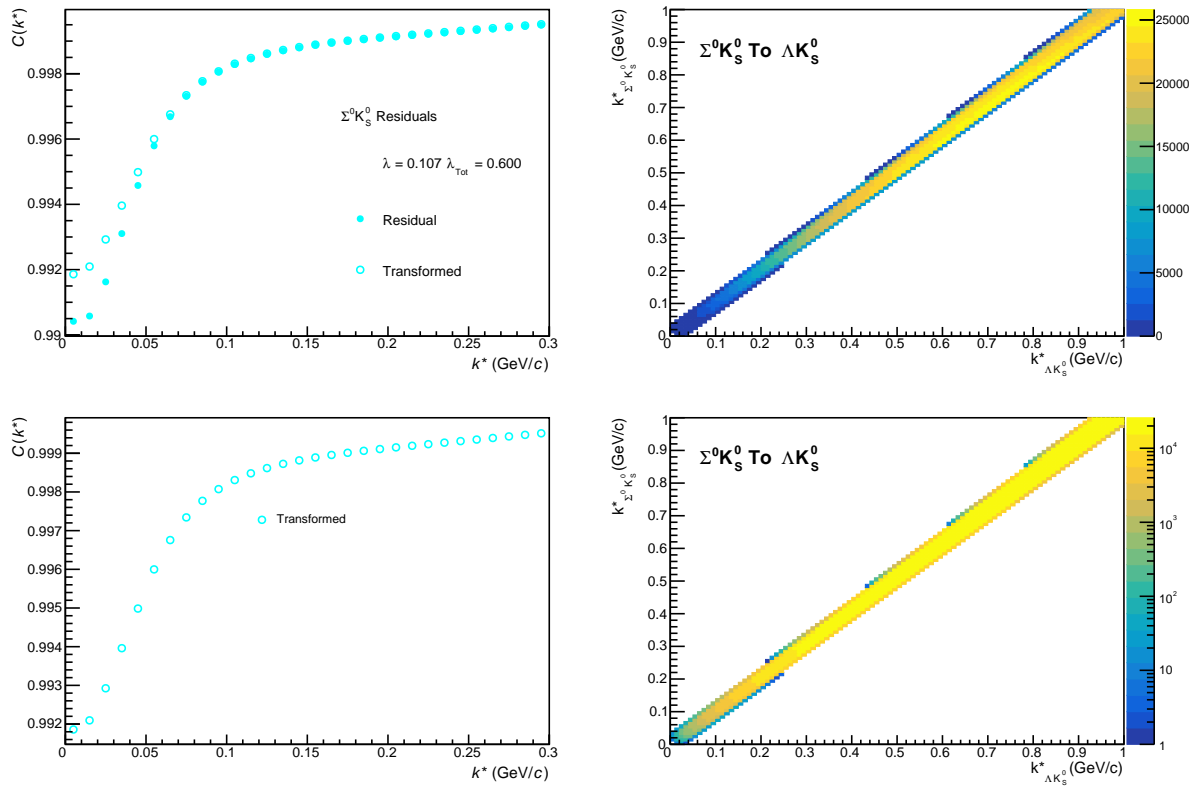


**Fig. 75:** Residuals:  $\Xi^0 \bar{K}^{*0}$  to  $\Lambda K^-$  (0-10% Centrality)

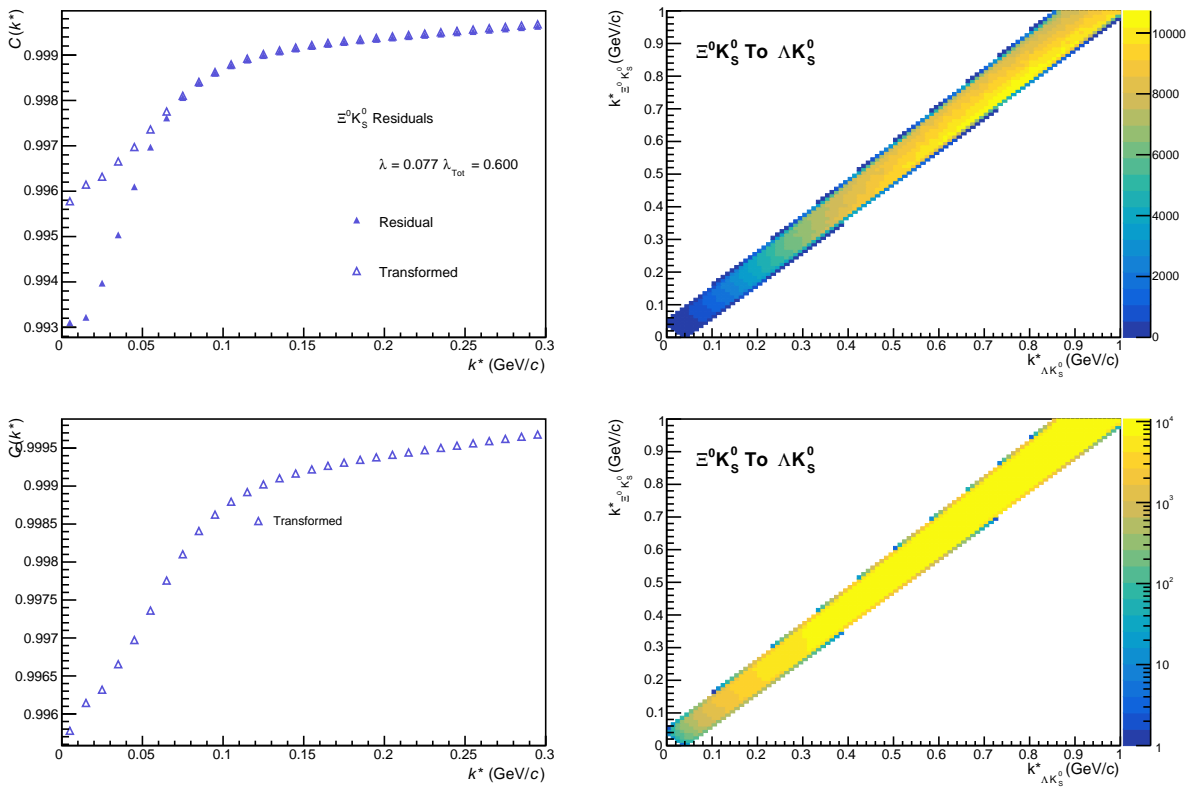
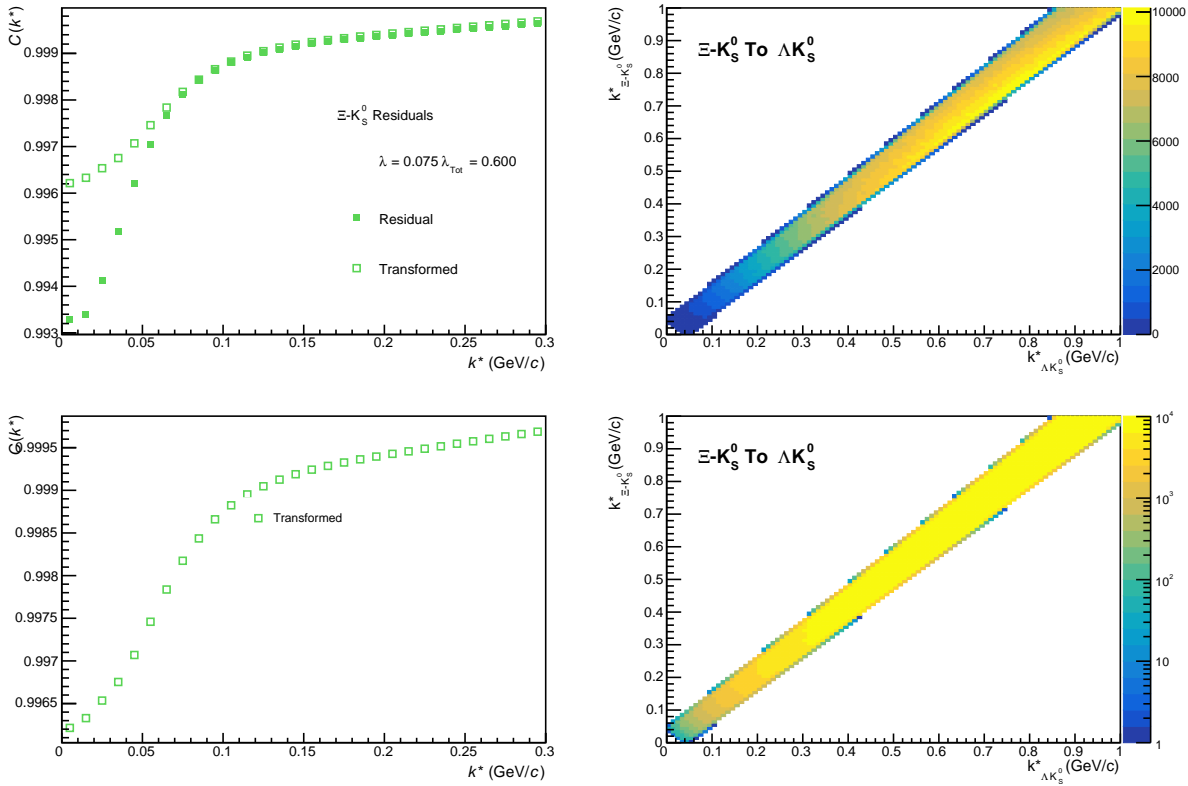


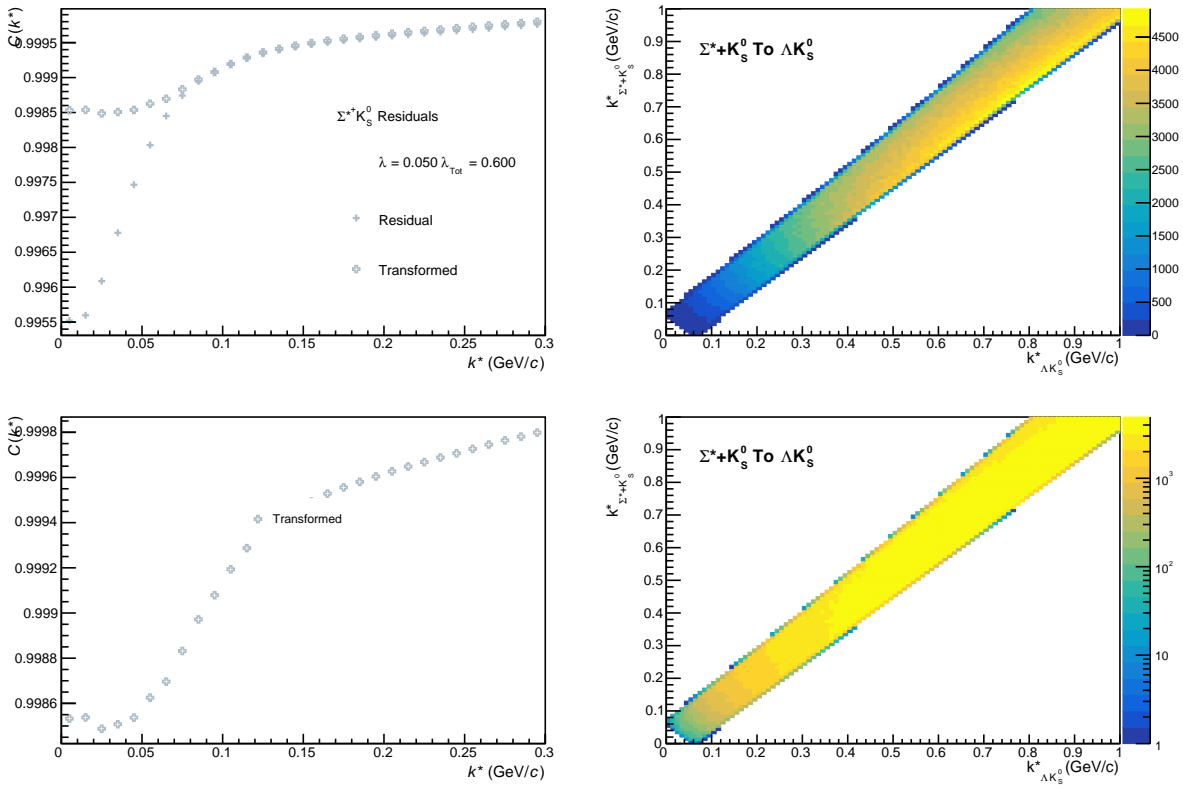
**Fig. 76:** Residuals:  $\Xi-\bar{K}^{*0}$  to  $\Lambda K^-$  (0-10% Centrality)

683 **9.1.3  $\Lambda K_S^0$  Residuals**

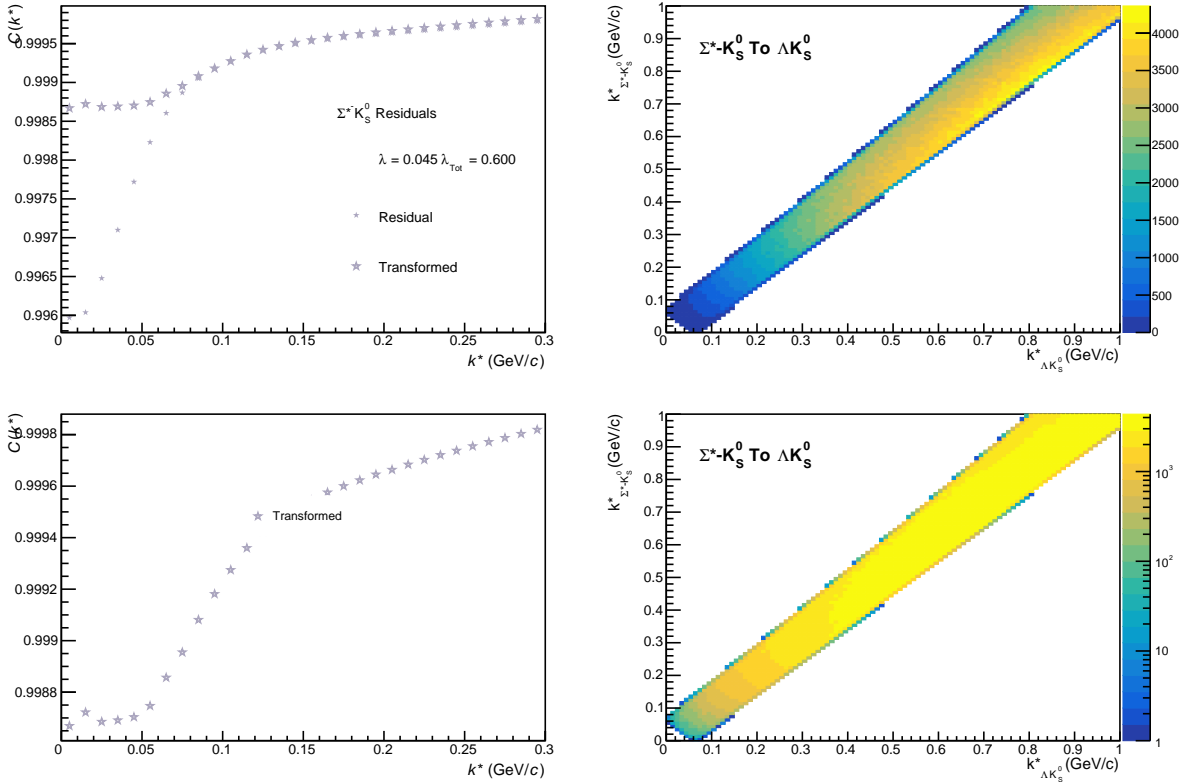


**Fig. 77:** Residuals:  $\Sigma^0 K_S^0$  to  $\Lambda K_S^0$  (0-10% Centrality)

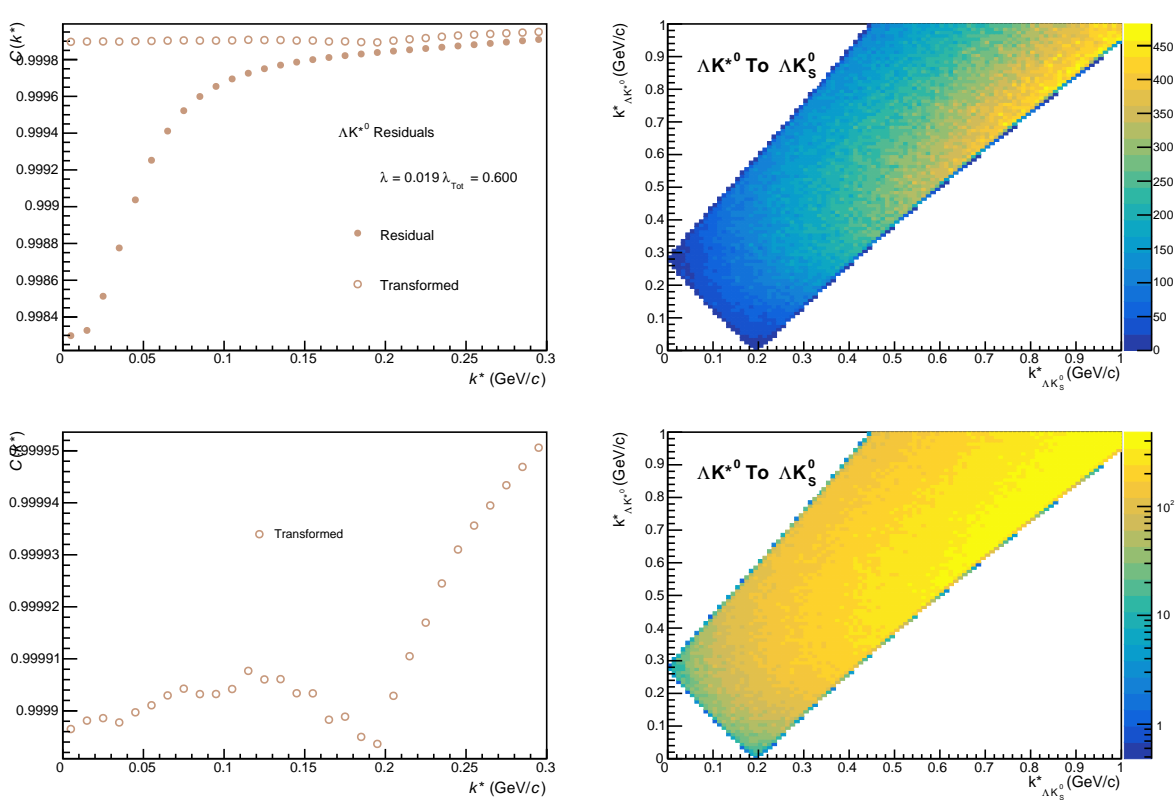
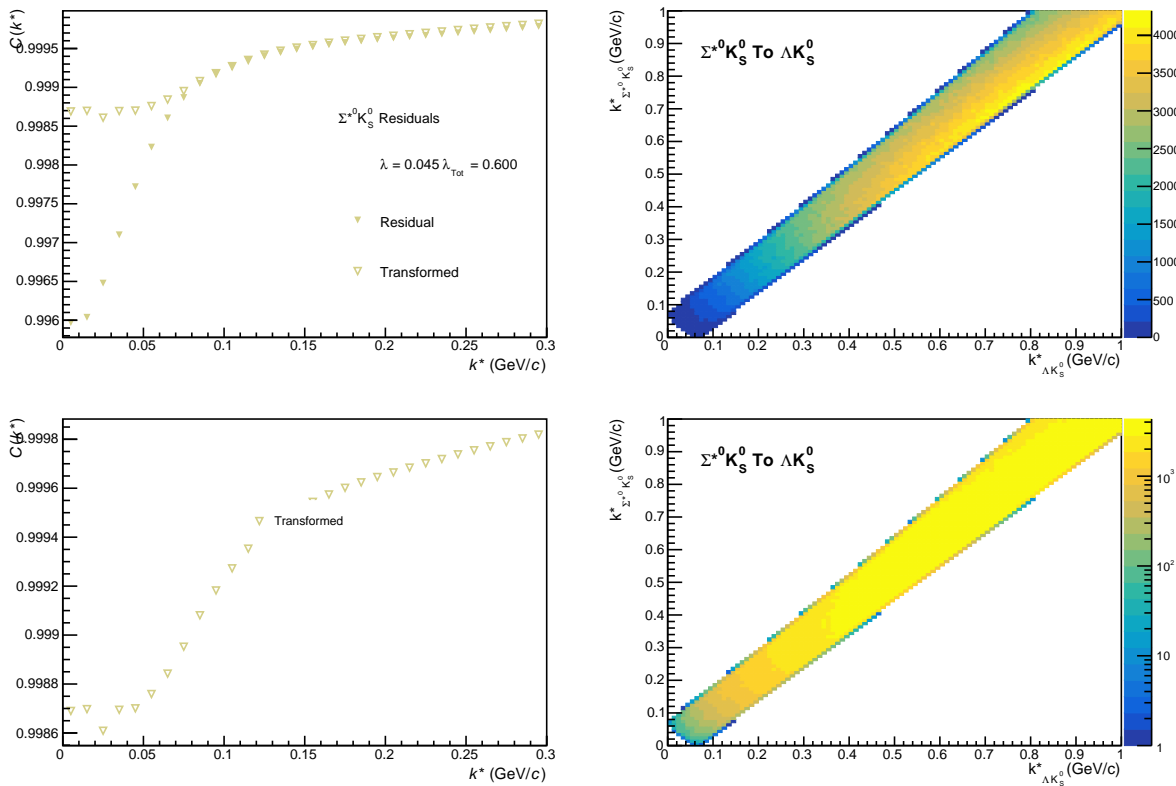

**Fig. 78:** Residuals:  $\Xi^0 K_S^0$  to  $\Lambda K_S^0$  (0-10% Centrality)

**Fig. 79:** Residuals:  $\Xi^- K_S^0$  to  $\Lambda K_S^0$  (0-10% Centrality)



**Fig. 80:** Residuals:  $\Sigma^*+K_S^0$  to  $\Lambda K_S^0$  (0-10% Centrality)



**Fig. 81:** Residuals:  $\Sigma^*-K_S^0$  to  $\Lambda K_S^0$  (0-10% Centrality)



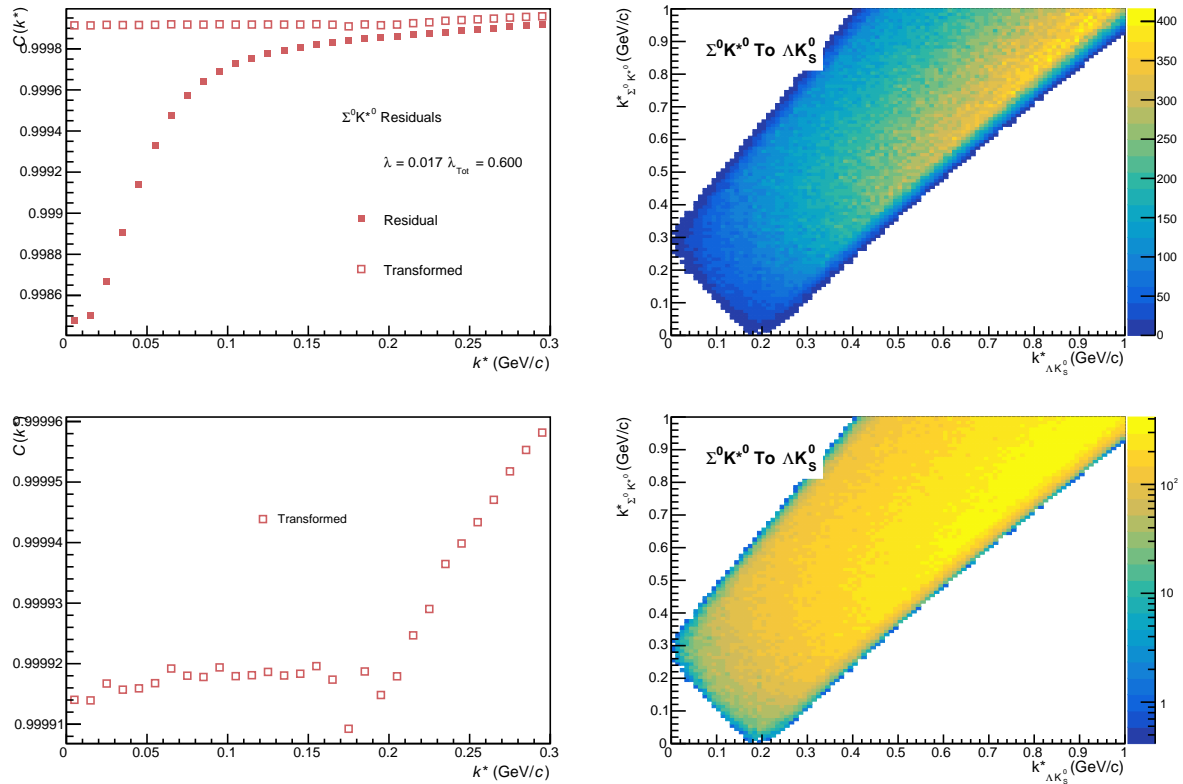


**Fig. 84:** Residuals:  $\Sigma^0 K^{*0}$  to  $\Lambda K_S^0$  (0-10% Centrality)

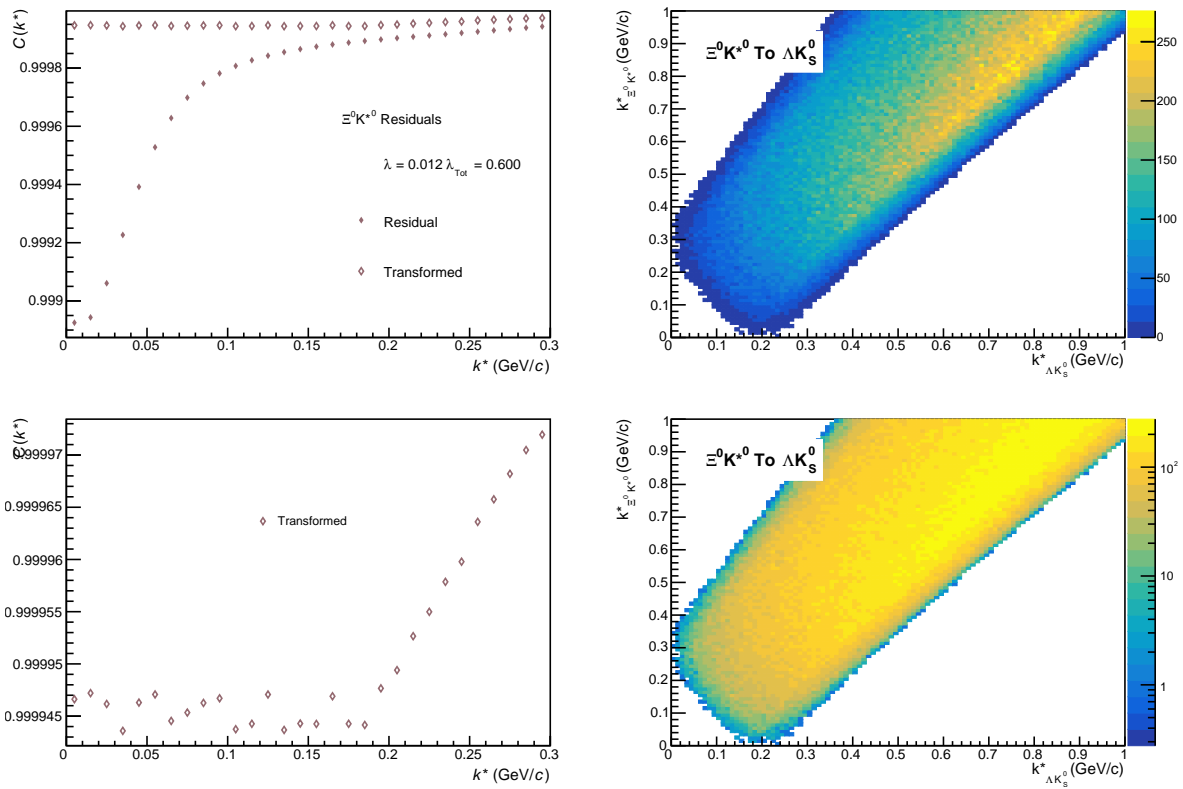


**Fig. 85:** Residuals:  $\Xi^0 K^{*0}$  to  $\Lambda K_S^0$  (0-10% Centrality)

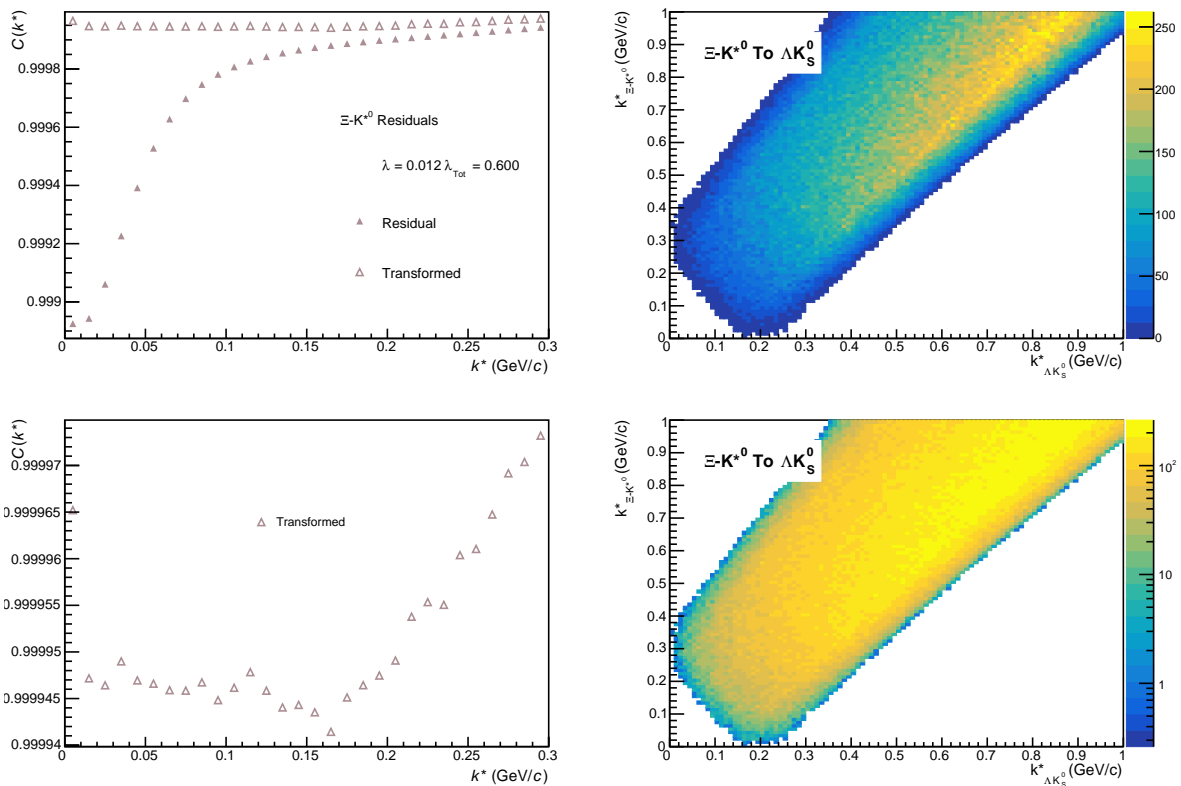


**Fig. 86:** Residuals:  $\Xi\text{-}K^{*0}$  to  $\Lambda K_S^0$  (0-10% Centrality)

## References

- [1] R. Lednicky and V. L. Lyuboshitz. *Sov. J. Nucl. Phys.*, 35:770, 1982.
- [2] Michael Annan Lisa, Scott Pratt, Ron Soltz, and Urs Wiedemann. Femtoscopy in relativistic heavy ion collisions. *Ann. Rev. Nucl. Part. Sci.*, 55:357–402, 2005.
- [3] S. E. Koonin. Proton Pictures of High-Energy Nuclear Collisions. *Phys. Lett.*, B70:43–47, 1977.
- [4] S. Pratt, T. Csorgo, and J. Zimanyi. Detailed predictions for two pion correlations in ultrarelativistic heavy ion collisions. *Phys. Rev.*, C42:2646–2652, 1990.
- [5] Richard Lednicky. Finite-size effects on two-particle production in continuous and discrete spectrum. *Phys. Part. Nucl.*, 40:307–352, 2009.
- [6] Adam Kisiel, Hanna Zbroszczyk, and Maciej Szymaski. Extracting baryon-antibaryon strong interaction potentials from  $p\bar{\Lambda}$  femtoscopic correlation functions. *Phys. Rev.*, C89(5):054916, 2014.
- [7] Jai Salzwedel and Thomas Humanic. Lambda femtoscopy in  $\sqrt{s_{NN}} = 2.76$  TeV Pb-Pb collisions at ALICE, Jan 2017. Presented 15 Dec 2016.
- [8] Yan-Rui Liu and Shi-Lin Zhu. Meson-baryon scattering lengths in HB chi PT. *Phys. Rev.*, D75:034003, 2007.
- [9] Maxim Mai, Peter C. Bruns, Bastian Kubis, and Ulf-G. Meissner. Aspects of meson-baryon scattering in three and two-flavor chiral perturbation theory. *Phys. Rev.*, D80:094006, 2009.
- [10] Jaroslav Adam et al. One-dimensional pion, kaon, and proton femtoscopy in Pb-Pb collisions at  $\sqrt{s_{NN}} = 2.76$  TeV. *Phys. Rev.*, C92(5):054908, 2015.